Breakout from the hot-CNO cycle via the ^{18}Ne(α,p)^{21}Na reaction

Darren Groombridge B.Sc M.Sc

A thesis submitted to the University of Edinburgh for the degree of Doctor of Philosophy in the Faculty of Science & Engineering

Department of Physics & Astronomy

2001

Abstract

The ^{18}Ne(α,p)^{21}Na reaction is of great importance to Nuclear Astrophysics as it provides a route to breakout from the hot-CNO cycle, possibly leading to the formation of the elements up to $A\sim100$.

This particular reaction has been studied using a ^{18}Ne beam, available at Louvain-la-Neuve, together with a helium gas target system previously developed for the investigation of (α,p) reactions with a radioactive beam.

This study covered an energy region from $\sim1.7-2.9$ MeV in the centre of mass frame of the ^{18}Ne+α system. A change in the detector geometry resulted in an increase in the detection efficiency and significantly reduced the proton background that hindered the previous measurement.

A direct measurement of the energy loss of the ^{18}Ne beam, as it passed through He gas, was undertaken to reduce a major source of uncertainty in the determination of the stellar reaction rate. This showed a linear relationship, between beam energy and distance traversed within the gas, over an energy scan of $\sim8-16$ MeV and gave an energy loss of (1.55 $\pm$ 0.01) MeV/cm and (15.96 $\pm$ 0.02) MeV for the energy of the ^{18}Ne beam upon entry into the gas.

This information was used, together with kinematic information from the protons, to provide information on the level structure in the compound nucleus, ^{22}Mg. Ten states have been identified within an energy region of $\sim10-11$ MeV and are in good agreement with information that is currently known. These resonances were used to calculate an enhanced stellar reaction rate which shows reasonable agreement with theoretical predictions [44] at and above a temperature of 1.5 GK.

Acknowledgements

Firstly I would like to thank my supervisor, Alan Shotter for his support and patience throughout this project. My thanks go to my second supervisor, Phil Woods for his support. Special thanks go to Tom Davinson whose guidance and encouragement was greatly appreciated. I would also like to thank Will Bradfield-Smith for our useful discussions and Gordon Turnbull for his technical help with the experimental preparation.

My thanks also go to our collaborators in Belgium, especially Pierre Leleux, for their invaluable contribution to this work.

Special thanks go to my closest friend, Mandeep for her continuous support and encouragement throughout my time in Edinburgh. Thanks go to my other friends, especially Alessia, Alison, Chris, Fred, Karsten and Steve for creating a good working atmosphere and to my former flatmate, David for making life outside work entertaining. Thanks also go to my family (Mum, Dad and Daniel) for all their support.

I wish to thank Gene Roddenberry for creating Star Trek which inspired me to study physics.

Finally I wish to acknowledge the Engineering and Physical Sciences Research Council (EPSRC) for funding this project.

Contents

List of Figures

List of Tables

Chapter 1

Introduction

1.1 The Role of Nuclear Physics in Astrophysics

Nuclear Physics is crucial to the understanding of our universe. Indeed, nuclear reactions are responsible for the existence of all chemical elements, which are formed in a process called nucleosynthesis. The knowledge of nucleosynthesis comes from astronomical observations and from studies of isotope abundance on Earth and in meteorites. These cosmic abundances (see figure 1.1) are interpreted in terms of their nuclear properties and the temperature and density conditions in which they can be synthesised.

^{1}H, ^{2}H, ^{3}He, ^{4}He, ^{7}Li and ^{9}Be were synthesised in the Big Bang. Heavier elements, on the other hand, are synthesised in stars. Thus it is quite plausible to think of the universe as a cosmic nuclear physics experiment. The work presented in this thesis involves the investigation of one particular nuclear reaction. Out of the many that occur, this reaction is an important part of

the jigsaw.

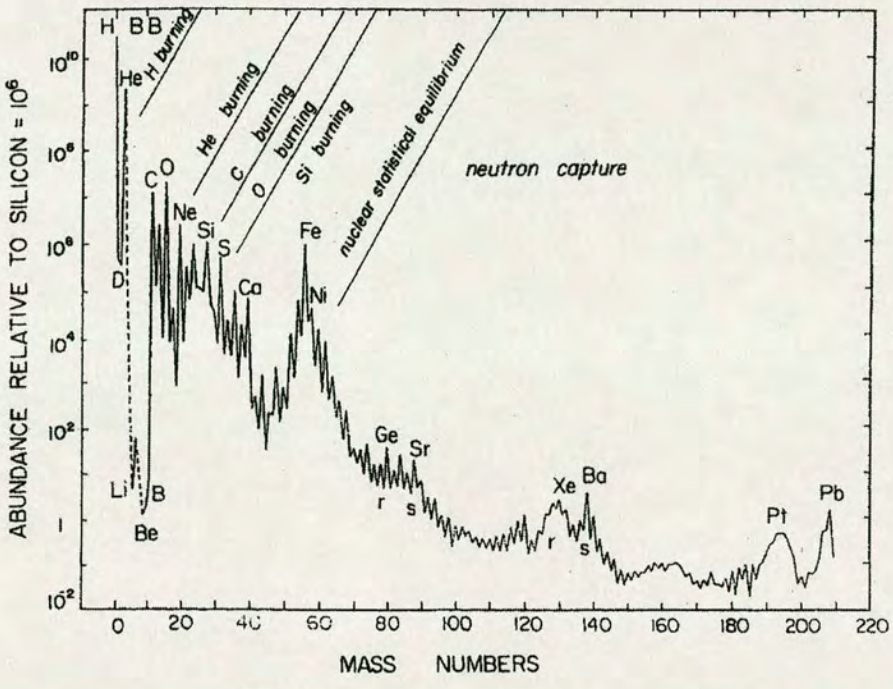

Figure 1.1: *Observed cosmic abundances relative to silicon [1].*

1.1.1 The History of the Universe

It is widely accepted that our universe began in a "Big Bang", in which all matter and radiation originated in an explosion some 10-20 billion years ago. This theory is supported by strong observational evidence. For instance, the discovery of the expansion of the universe, cosmic background radiation and the observed cosmic abundance of helium.

Since its formation, the universe has been expanding, cooling as it does so, from initial conditions of both extreme temperature and density. The Planck time of 10^{-43}s specifies the earliest time in which the current laws of physics hold. The Uncertainty Principle determines this lower limit. At the Planck

time, the temperature was around 10^{32} K. A quantum theory of gravity is required to describe the universe at this time. At 10^{-37}s after the Big Bang, the universe can be described by gravity and the unification of the strong, electromagnetic and weak forces. These forces were no longer unified when the temperature of the universe cooled to $<10^{29}$ K. When the universe was 10^{-35}s old, it is believed that the amounts of matter and antimatter (existing as quarks, leptons and their associated antiparticles) were comparable. The asymmetric decay of the X boson led to matter being left over. Between 10^{-35} and $<10^{-30}$s, the universe is thought to have undergone very rapid expansion - this is known as the *inflationary era.*

The dominant particle reactions were determined by a fall in temperature as the universe expanded with age. First of all, quarks annihilated with anti-quarks and those left over formed protons and neutrons. Lepton annihilation followed hadron annihilation and continued until the universe was 100s old. This is known as the radiation era because annihilation photons dominated the universe. The universe was then at a temperature of 10^9K and was cool enough for deuterium to form before neutrons decayed. The deuterium fused together forming helium, almost in the abundance seen today. Some lithium was also formed. At this point the elemental mass fractions were $\sim$0.76, 0.24 and 0.00 for hydrogen, helium and metals (elements heavier than helium) respectively. The reader is referred to reference [2] for further details.

The universe between the times 10^2 and 10^{12}s, almost entirely consisted of ionised hydrogen and helium. When the temperature dropped to $\sim$10,000 K (i.e when the universe was between 10^{12} and 10^{16}s old), this was the beginning of the matter era. Neutral hydrogen and helium atoms formed as electrons could recombine with nuclei. The electromagnetic background

cooled to 2.7 K, the temperature observed today. The decoupling of matter from radiation enabled stars and stellar systems to form. Galaxies began to form 10^{16}s after the Big Bang, eventually leading to the universe we see today.

1.1.2 Stellar Evolution

The Birth of Stars

Stars are enormous gaseous bodies which generate energy through nuclear fusion reactions within their core. They are formed in the densest regions of the interstellar medium (ISM) in collapsing Giant Molecular Clouds (GMC). Here temperatures are between 100-1000 K. These clouds resist collapse due to the heating effects of nearby stars, their rotation and magnetic field pressure. However, the collapse can be initiated through shocks from supernova explosions or through turbulence from passing through the spiral density wave in spiral galaxies. The conditions for initial collapse can be described by the Virial Theorem. The general form of which is [3]:

$$\frac{1}{2}\frac{d^2I}{dt^2} = 2 < T > + U_{\text{Mag}} + \Omega + 3\int P\,dV \tag{1.1}$$

where the term on the left hand side is the energy of the generalised moment of inertia (I), $2<T>$ is the kinetic energy of mass motion (i.e from turbulence and rotation), U_{Mag} is the magnetic energy, Ω is the gravitational potential energy, $3\int P\,dV$ is the internal thermal energy, P is the pressure and V is the volume.

Collapse occurs when the Virial Theorem is negative and when the mass

of the cloud is greater than the critical or Jeans mass, M_J. Gravitational instability leads to the development of smaller, denser regions which develop to the point of self-gravitational collapse. During collapse half of the gravitational energy is released (leading to an increase in temperature) and half is radiated away. This must take place in order to satisfy the Virial Theorem which assumes conditions of hydrostatic equilibrium. Gravity now wins and the collapse can not be stopped at this stage.

The final fragments are protostars and are isolated from the rest of the cloud. These stable hydrostatic bodies subsequently draw in gas from the cloud through gravitational attraction. A build up in pressure allows infalling matter to settle onto the surface of the protostar. Thermal and magnetic pressure increases towards the centre, thus supporting the outer layers. Density also increases towards the centre. In the core, the material becomes optically thick to molecular emissions and hence the temperature inside the core increases. This results in an increase in the internal pressure and the collapse begins to slow down. Further temperature increases cause hydrogen and helium to ionise. If the core temperature reaches $\sim 10^6$ K hydrogen burning commences because the kinetic energy of nuclei is now sufficient to penetrate the Coulomb barrier. The object is now a star on the main sequence (see figure 1.2) and maintains its stability against gravitational collapse through thermonuclear reactions.

The Main Sequence

This is the phase where the only energy source is that from hydrogen fusion in the core. A star spends most of its life on the main sequence. The following relations hold for stars on the main sequence:

$$L = 4\pi R^2 \sigma T^4 \tag{1.2}$$

$$M \propto L^{1/3.8} \tag{1.3}$$

$$t \propto \frac{M}{L} \tag{1.4}$$

where L is the luminosity, R is the radius, T is the temperature, M is the mass and t is the lifetime of the star. Thus less massive stars stay on the main sequence for longer because the rate at which hydrogen is consumed is slower than for massive stars.

An upper mass limit occurs when radiation pressure acting on the envelope of the star exceeds the weight of the envelope, expelling matter from its surface. Thomson scattering is dominant, exerting an outward force on matter. This limit, known as the Eddington limit, occurs when the outward force is balanced by gravity and is $\sim$60-120$M_\odot$[3].

A lower mass limit occurs at $\sim$0.08 $M_\odot$ when the protostar becomes dense enough to become dominated by the electron degeneracy pressure, but before it can contract enough to raise the core temperature above 10^6 K.

The most fundamental property of a star is indeed its mass. As well as giving information on other stellar properties (such as luminosity, radius and lifetime) the mass of a star also determines its fate.

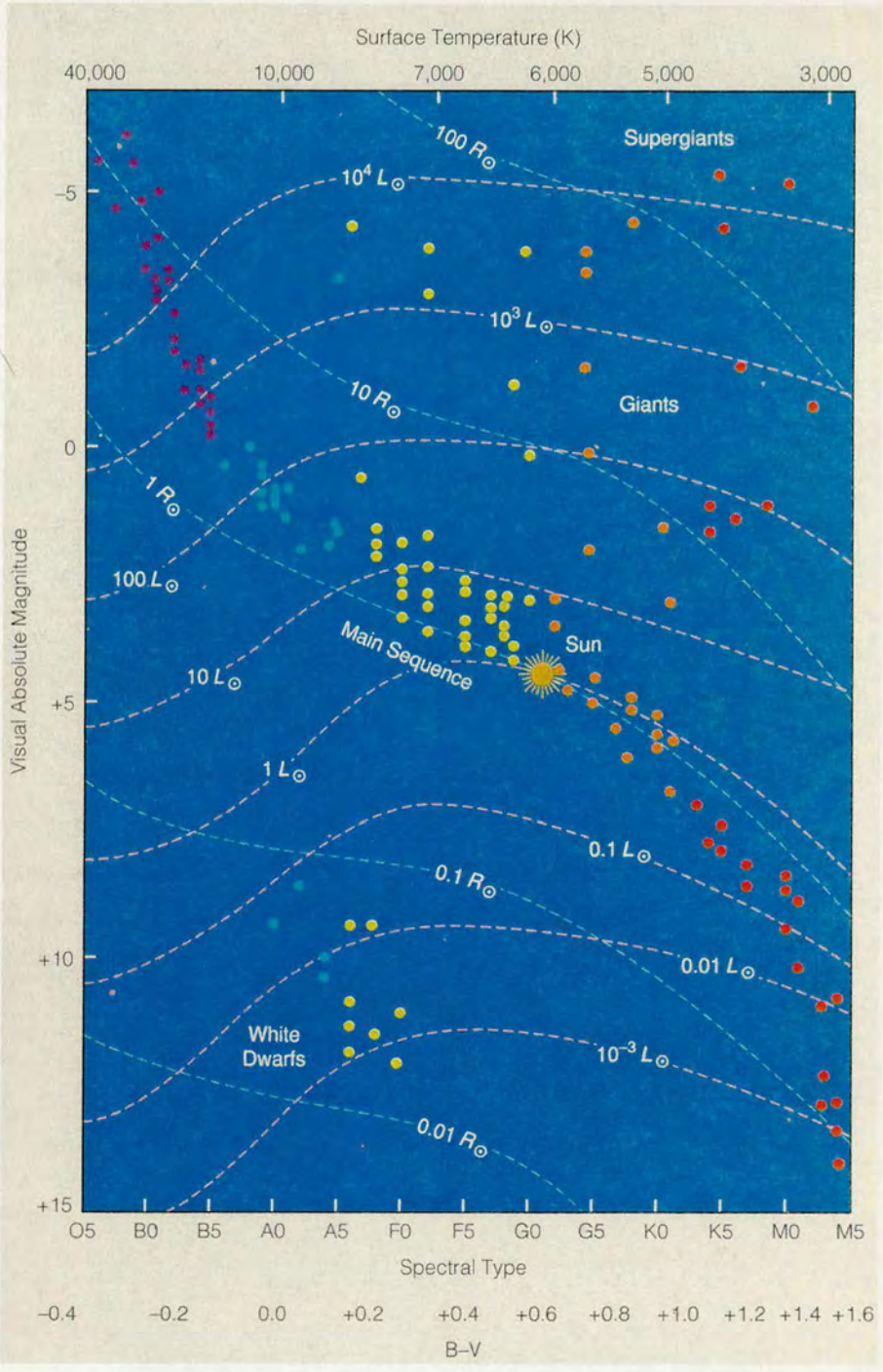

Figure 1.2: *The Hertzsprung-Russell diagram for stars showing a plot of absolute magnitude (luminosity) vs. spectral class [4].*

Post-main sequence evolution ($M_\star$<2.2$M_\odot$)

When a star exhausts its supply of hydrogen the stability against gravity is lost. Thus it begins to collapse causing the core temperature to increase. H-burning can occur in a shell around the core if the temperature reaches $\sim 10^6$ K. However, not all the energy generated in shell burning reaches the surface of the star. Some of the energy heats the intermediate layers giving rise to expansion of the outer layers. The surface luminosity stays constant and thus the effective temperature decreases. The star now becomes a *red subgiant.*

The core continues to contract and reaches a point where the electron degeneracy pressure becomes dominant. Expansion of the outer layers stops and the luminosity increases. The star is now a *red giant.* The core eventually reaches the temperature necessary for the triple alpha reaction to start. The degeneracy of the core means that the pressure does not increase with temperature. This causes an increase in the energy generation rate, leading to a rapid increase in temperature producing a *helium flash.* The luminosity produced in this flash can, for a few seconds, be as much as the luminosity of an entire galaxy! The very high temperature in the core eventually increases the energy of the electrons thus lifting the degeneracy. The star is now on the *horizontal branch* with a He-fusing core surrounded by a H-fusing shell. Once the fuel in the core is exhausted, it begins to contract under gravity once more. The temperature increases further as a result forming a He-burning shell within the H shell. If the core temperature rises further then C-burning starts. The star climbs the *Asymptotic Giant Branch (AGB)* and becomes a *Red Supergiant.*

At the top of the AGB, stellar winds cause mass loss. Thus the star evolves

to become a *Planetary Nebula* very quickly. The core continues to burn material. Once exhausted the star becomes a *White Dwarf.*

In main sequence stars with a mass $\leqslant 0.7 M_{\odot}$ the core temperature does not reach the temperature required for He-burning. Without mass loss, these stars evolve to become white dwarfs. In stars with a mass between $0.7 M_{\odot}$ and $1.4 M_{\odot}$, the core temperature does not reach the temperature required for C-burning. With some mass loss, the star evolves to the planetary nebula stage and then becomes a white dwarf.

Post-main sequence evolution (massive stars)

The evolution of massive stars is the same as lower mass stars. However, the main sequence to subgiant stage is much faster giving rise to the observed absence of stars on the Hertzsprung-Russell diagram (figure 1.2) - known as the *Hertzsprung gap.* Before the core becomes degenerate, the core temperature becomes high enough for He-burning (via the triple alpha process) to start. As the temperature increases further, C and O burning begins forming Si. At this point the core loses energy via neutrino emission.

For stars with $M > 8 M_{\odot}$, an onion layer structure is reached up to Fe with thick inert shells and thin fusion shells as seen in figure 1.3. Fe marks the endpoint of fusion reactions (see later). Above the Fe group the reactions are endothermic (since A=56 gives the maximum binding energy per nucleon) and the inner core can finally become exhausted. When the outer layers come into contact with the core, there is a *core bounce.* The shock wave produced causes the outer layers to explode outwards. This is a *Type II Supernova* explosion.

If the mass of the remaining core exceeds $1.4 M_{\odot}$ (the Chandrasekhar limit),

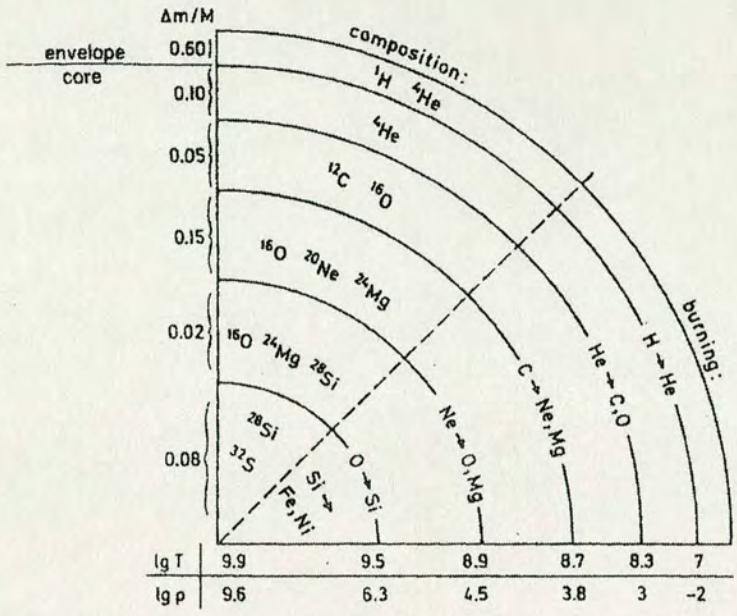

Figure 1.3: *The onion layer structure of a massive star. Typical mass fractions are indicated on the vertical axis, while typical temperatures and densities are indicated on the horizontal axis [5].*

the star is not stable as a white dwarf because the force of gravity is greater than the electron degeneracy pressure. Thus the core continues to collapse until protons and electrons coalesce into neutrons. It is now a *Neutron star* and maintains its stability through the neutron degeneracy pressure. Having a diameter of ~10km, a sugar cube would weigh ~1 tonne on the surface. A core that collapses further becomes a *Black Hole* when its radius is that of the Schwartzschild radius. At this radius, the escape velocity exceeds the speed of light, and thus all information is trapped in the "event horizon". A core with mass $>3M_{\odot}$ can become a black hole.

1.1.3 Stellar Energy Sources

The reader is referred to [6, 7] for further details on the synthesis of elements in stars, however an overview will be given here.

The types of reactions that occur depend on the mass of the star. For stars with mass $<1.5M_{\odot}$, the pp-chain is the dominant process whereas for stars with mass $>1.5M_{\odot}$ the CNO (or Bethe-Weiszaecker) cycle is the dominant process.

The pp-chain

The pp-chain consists of the following steps (see figure 1.4):

$$^{1}\mathrm{H} + {}^{1}\mathrm{H} \rightarrow {}^{2}\mathrm{D} + \mathrm{e}^{+} + \nu$$

This weak interaction is very slow (10^{10} yrs) and its probability has not been determined in the laboratory. In fact our Sun is still shining because this reaction is very slow! The positron immediately undergoes electron-positron pair annihilation (producing two gamma rays). The neutrino escapes freely, carrying away some of the energy that is produced. The deuterium produced is destroyed by the following reaction:

$$^{2}\mathrm{D} + {}^{1}\mathrm{H} \rightarrow {}^{3}\mathrm{He} + \gamma$$

This reaction occurs very quickly (1.6s) making the abundance of deuterium very small. Three different reaction pathways are now open. The most probable of these is:

$$^{3}\mathrm{He} + {}^{3}\mathrm{He} \rightarrow {}^{4}\mathrm{He} + 2\,{}^{1}\mathrm{H}$$

This is the pp-1 chain. There are two other competing pp chains:

$$^3\mathrm{He} + {}^4\mathrm{He} \rightarrow {}^7\mathrm{Be} + \gamma$$

$$^7\mathrm{Be} + \mathrm{e}^- \rightarrow {}^7\mathrm{Li} + \nu$$

$$^7\mathrm{Li} + {}^1\mathrm{H} \rightarrow {}^4\mathrm{He} + {}^4\mathrm{He}$$

This is the pp-2 chain. The pp-3 chain is given by the following sequence of reactions:

$$^3\mathrm{He} + {}^4\mathrm{He} \rightarrow {}^7\mathrm{Be} + \gamma$$

$$^7\mathrm{Be} + {}^1\mathrm{H} \rightarrow {}^8\mathrm{B} + \gamma$$

$$^8\mathrm{B} \rightarrow {}^8\mathrm{Be} + \mathrm{e}^+ + \nu$$

$$^8\mathrm{Be} \rightarrow {}^4\mathrm{He} + {}^4\mathrm{He}$$

The net result of each of these branches of the pp-chain is the conversion of four protons into one helium nucleus, two positrons, two electron neutrinos and gamma rays, giving out a total energy of 26.7 MeV.

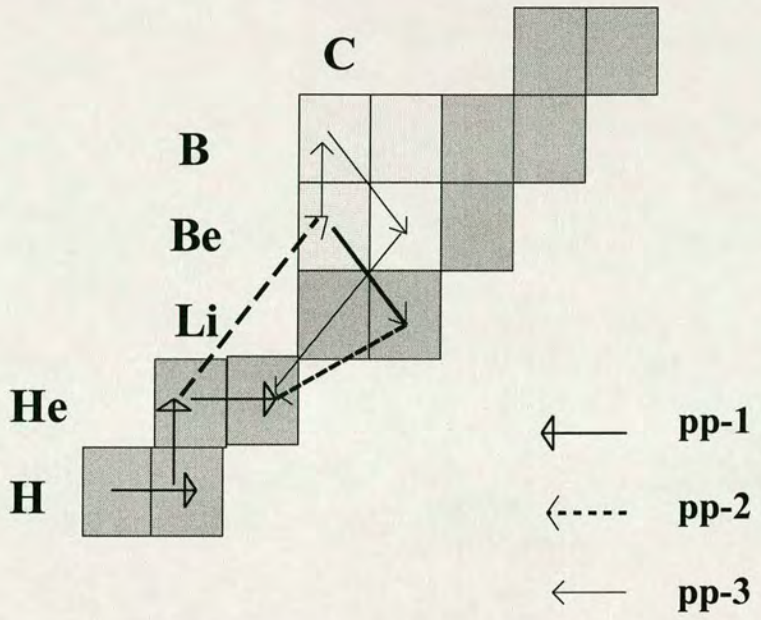

Figure 1.4: *The pp-chain reactions [8].*

The CNO cycles

This is very sensitive to temperature and is the more dominant process at higher temperatures because of the faster reaction rates. It consists of the following sequence:

$$^{12}\mathrm{C(p,\gamma)^{13}N(e^{+}\nu)^{13}C(p,\gamma)^{14}N(p,\gamma)^{15}O(e^{+}\nu)^{15}N(p,\alpha)^{12}C}$$

where carbon, nitrogen and oxygen act as catalysts converting four protons into one helium nucleus, two positrons, two electron neutrinos and gamma rays (as in the pp-chain). The CNO cycle is more efficient than the pp-chain because the reaction rate is greater at higher temperatures. However, the CNO cycle produces slightly less energy as more energy is carried away by the freely escaping neutrinos. The slowest reaction is that of the $^{14}\mathrm{N(p,\gamma)^{15}O}$ reaction. This then determines the energy generation in the H-burning stage

of a star.

1.1.4 Other Burning Processes

The Triple Alpha Reaction

At temperatures >0.1 GK, helium can be fused to form carbon in the following reactions:

$$\alpha + \alpha \rightarrow {}^{8}\mathrm{Be} + \gamma$$

$${}^{8}\mathrm{Be} + \alpha \rightarrow {}^{12}\mathrm{C}^{\star} + \gamma$$

^{8}Be is particle unstable and rapidly decays back to two alpha particles. Thus the production of ^{12}C is produced by three alpha particles colliding almost simultaneously. For significant production of ^{12}C, the reaction must proceed through the 7.654 MeV 0^{+} excited state. Most of the carbon formed in this way decays back into three alpha particles, however, the ground state of ^{12}C can be reached through gamma-decay (although with a small probability). The triple alpha reaction can thus be summarised as:

$$\alpha + \alpha + \alpha \rightarrow {}^{12}\mathrm{C} + \gamma$$

Alpha Reactions

At ~0.1 GK, the following alpha capture reactions can occur:

$${}^{12}\mathrm{C} + \alpha \rightarrow {}^{16}\mathrm{O} + \gamma$$

$${}^{16}\mathrm{O} + \alpha \rightarrow {}^{20}\mathrm{Ne} + \gamma$$

$${}^{20}\mathrm{Ne} + \alpha \rightarrow {}^{24}\mathrm{Mg} + \gamma$$

These reactions are, however, rare in occurrence but explain the O:C ratios needed for further burning towards heavier mass.

Carbon Burning

At temperatures ~0.4-0.8 GK, carbon is ignited through the following reactions:

$$^{12}\mathrm{C} + {}^{12}\mathrm{C} \rightarrow {}^{20}\mathrm{Ne} + \alpha$$

$$^{12}\mathrm{C} + {}^{12}\mathrm{C} \rightarrow {}^{23}\mathrm{Na} + \mathrm{p}$$

$$^{12}\mathrm{C} + {}^{12}\mathrm{C} \rightarrow {}^{23}\mathrm{Mg} + \mathrm{n}$$

The ^{20}Ne formed in the first reaction can either react or decay via:

$$^{20}\mathrm{Ne} + \alpha \rightarrow {}^{24}\mathrm{Mg} + \gamma$$

or:

$$^{20}\mathrm{Ne} + \gamma \rightarrow {}^{16}\mathrm{O} + \alpha$$

Oxygen Burning

At temperatures ~1-2 GK, the following reactions can occur:

$$^{16}\mathrm{O} + {}^{16}\mathrm{O} \rightarrow {}^{32}\mathrm{S} + \gamma$$

$$^{16}\mathrm{O} + {}^{16}\mathrm{O} \rightarrow {}^{31}\mathrm{P} + \mathrm{p}$$

$$^{16}\mathrm{O} + {}^{16}\mathrm{O} \rightarrow {}^{28}\mathrm{Si} + \alpha$$

$$^{16}\mathrm{O} + {}^{16}\mathrm{O} \rightarrow {}^{31}\mathrm{S} + \mathrm{n}$$

$$^{16}\mathrm{O} + {}^{16}\mathrm{O} \rightarrow {}^{24}\mathrm{Mg} + 2\alpha$$

Significant abundances of nuclei up to the Fe-group are synthesised.

Silicon Burning

At temperatures ~3-5 GK, the energy of photons is large enough for photo-disintegration of ^{28}Si to occur as follows:

$$^{28}\mathrm{Si} + \gamma \rightarrow {}^{24}\mathrm{Mg} + \alpha$$

This reaction is followed by capture reactions such as:

$$^{28}\mathrm{Si} + {}^{28}\mathrm{Si} \rightarrow {}^{56}\mathrm{Ni} + \gamma$$

which leads to the formation of ^{56}Fe via:

$$^{56}\mathrm{Ni} \rightarrow {}^{56}\mathrm{Fe} + \mathrm{e}^{+} + \mathrm{e}^{+} + 2\nu$$

Heating, caused by the absorption of emitted γ rays, gives rise to the observed light curves for type I supernovae. ^{56}Co was synthesised in Supernova 1987A and therefore iron-group elements are also formed in type II supernovae.

1.1.5 Formation of Nuclei with A>56

Nucleosynthesis of these elements require reactions involving neutron capture on the iron-group isotopes. Having no charge, neutrons can be captured

at low energies. Free neutrons exist in the core of a star. Nuclei up to ^{209}Bi can be synthesised under conditions of slow neutron capture (s-process). Here neutron capture reactions occur on timescales longer than that of the β decay lifetimes. S-process nucleosynthesis occurs, prior to core collapse, in red giant stars as a result of He shell flashes. Resulting temperatures are >0.3 GK and neutrons are formed by the ^{22}Ne(α,n)^{25}Mg and ^{13}C(α,n)^{16}O reactions. S-process isotopes including Zr and ^{99}Tc have been observed in the spectra of red giant stars.

Some stable isotopes of elements lighter than Pb are bypassed by the s-process. Hence these isotopes must be synthesised under conditions of rapid neutron capture (r-process). At higher temperatures, nuclei up to ^{252}Cf, or higher, can be synthesised. Some r-process nucleosynthesis is thought to occur in luminous red giants. Supernovae type II provide high temperature and nonequilibrium conditions. The propagation of a shock wave through the He zone of a massive star is another likely mechanism for the r-process. Given the very different types of stars in which these two processes occur, it is interesting to point out that the s-process and r-process abundance peaks are similar.

The elements produced in stars eventually get redistributed into the ISM through mass loss processes. For example, elements up to Si are redistributed from stellar winds, planetary nebulae and nova explosions. Fe and heavier nuclei on the other hand become redistributed from supernova explosions. Indeed we are all "children of the stars".

1.1.6 The Hot-CNO Cycles and Breakout Reactions

At temperatures ~0.2 GK, the $^{13}N(p,\gamma)^{14}O$ reaction becomes more dominant and the $^{13}N(e^+\ \nu)^{13}C$ reaction is bypassed. This gives rise to the following reaction sequence:

$$^{12}C(p,\gamma)^{13}N(p,\gamma)^{14}O(e^+\nu)^{14}N(p,\gamma)^{15}O(e^+\nu)^{15}N(p,\alpha)^{12}C$$

which is known as the hot-CNO cycle (see figure 1.5). At temperatures ~0.4 GK, the $^{14}O(e^+\nu)^{14}N$ reaction is bypassed, giving rise to another series of reactions:

$$^{12}C(p,\gamma)^{13}N(p,\gamma)^{14}O(\alpha,p)^{17}F(p,\gamma)^{18}Ne(e^+\nu)^{18}F(p,\alpha)^{15}O(e^+\nu)^{15}N(p,\alpha)$$

This is the second hot-CNO cycle (also seen in figure 1.5) which feeds material back into the first cycle via the $^{18}F(p,\alpha)^{15}O$ reaction. The slowest process in the first hot-CNO cycle are the β-decays of ^{14}O and ^{15}O ($t_{1/2}$=70.6s and 122s respectively). The slowest process in the second hot-CNO cycle is that of the β-decay of the ^{18}Ne isotope ($t_{1/2}$=1.67s). These β decaying isotopes are called *waiting point isotopes.*

Further nucleosynthesis requires a *breakout* from the CNO cycles (see figure 1.5). At temperatures >0.4 GK, the ^{15}O and ^{18}Ne waiting points can be bypassed by the $^{15}O(\alpha,\gamma)^{19}Ne$ and $^{18}Ne(\alpha,p)^{21}Na$ reactions respectively. These are the two main possible breakout routes which lead to a predicted r(apid) p(roton)-process via the hot Ne-Na and Mg-Al cycles.

The rp-process (see [10] for further details) is a series of proton and alpha

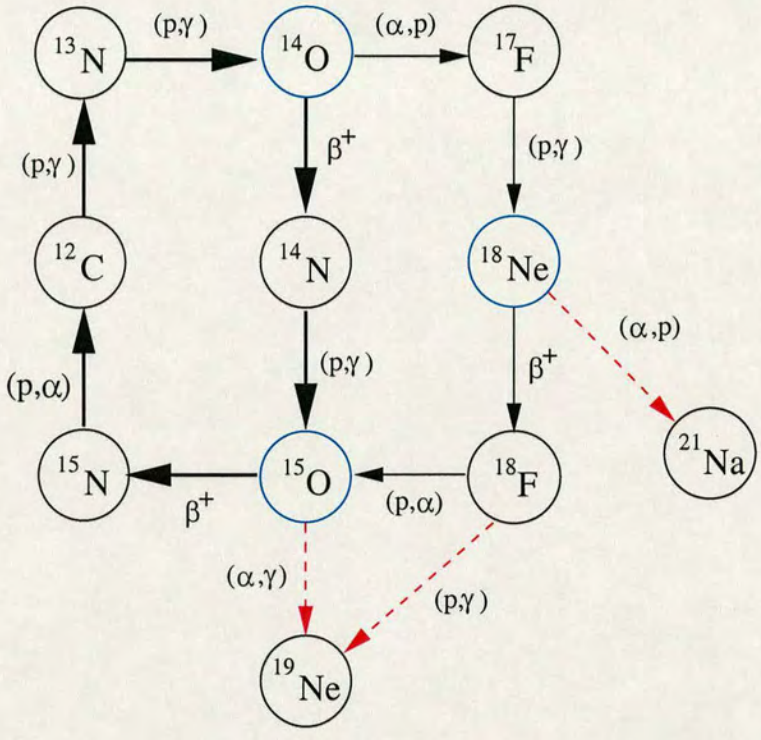

Figure 1.5: *The hot-CNO cycles. The dominant reaction path is denoted by the heavy arrows. At higher temperatures, the second hot-CNO cycle becomes important. The waiting points are shown in blue and the breakout reactions are denoted by the red arrows [9].*

capture reactions on nuclei lying between the line of stability and the proton drip line. Charged particle reactions compete with the β-decays of the waiting point nuclei. These waiting point nuclei govern the rate of flow of material toward heavier mass.

The reaction $^{15}O(\alpha,\gamma)^{19}Ne$ has been studied indirectly by Laird *et al* [11] The study of the $^{18}Ne(\alpha,p)^{21}Na$ reaction is the object of this thesis.

1.1.7 Sites for Explosive Hydrogen Burning

Close Binary Systems

Nearly 60% of all stars are found in binary systems. In a close binary system each star alters the structure of the other. Stellar surfaces are distorted by tidal forces (differences in gravitational force between two positions on a star). This distortion gives rise to the internal dissipation of energy (from fluid friction). The two stars have circularised orbits and are "tidally locked" - the lowest energy configuration. Thus energy is lost from both orbital and rotational energy.

A test particle in this system is affected by gravity and the centrifugal force. The net potential energy is the sum of these two individual potentials. A surface of constant net potential is known as a *Roche Lobe* (see figure 1.6). Lagrangian points are points where the effective force (which acts perpendicularly to such surfaces) is zero. Since the gravitational forces exerted by both stars cancel each other at the Lagrange point, material can be attracted to one star or the other. If one of the stars expands during its evolution and fills its Roche Lobe, matter will flow over to the companion and accrete in a disc.

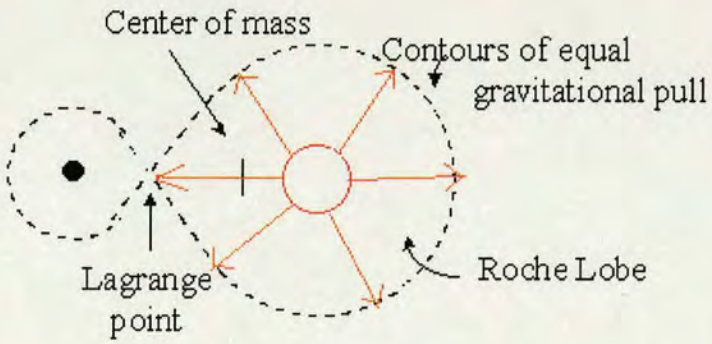

Figure 1.6: *The Roche Lobe of a binary system showing gravitational equipotential surfaces separated by a contact point.*

Evolving Binary Stars

It is assumed that the two stars in a binary system arrive on the main sequence at around the same time. This can occur if cloud fragmentation is late. As the radii of the stars are less than that of their respective Roche Lobes, the stars evolve separately. However, the more massive star evolves more quickly. If the more massive star expands to the red giant stage and its radius is greater than its Roche Lobe, *Roche Lobe overflow* begins and continues. The temperature (and hence luminosity) of the massive star decreases due to mass loss and becomes a subgiant. The smaller star gains mass and so its temperature (and luminosity) increases but still remains near the main sequence. The more massive star loses its envelope and becomes a white dwarf (and is now the less massive star). Thus the companion star is now more massive, still near the main sequence.

Mass transfer from a main sequence star to a white dwarf can cause explosive hydrogen burning. This is the case of *Novae*. The white dwarf is either one with a CO core or one with a O-Ne-Mg core. Hydrogen rich material piles

up on the surface of the white dwarf, under electron degenerate conditions, until a critical mass is reached. After this the temperature increases, but no expansion occurs, ultimately causing a themonuclear ignition. This triggers a thermonuclear runaway until the degeneracy is lifted and thermonuclear burning sets in, at a temperature of ~0.2 GK. The hot-CNO cycles are the main energy source. An abundance of ^{20}Ne and ^{24}Mg means that additional energy comes from the Ne-Na and Mg-Al cycles which leads to the production of the P and S isotopes. Recent advances in the studies of the nova outburst are highlighted in [14].

If the accretion takes place on the surface of a neutron star, this is an *X-Ray Binary* (or X-Ray Burster). Nucleosynthesis takes place in much the same way as novae. However, the accretion of matter onto the neutron star occurs at a slower rate compared with that for novae. Again under degenerate gas conditions, thermonuclear reactions begin resulting in a thermonuclear runaway in the accretion disc. The main energy sources are the hot-CNO cycles and energy production is limited by the ^{14}O, ^{15}O and ^{18}Ne waiting points. Once temperature dependent, the triple alpha process converts helium into carbon which in turn is processed in the CNO and the hot-CNO cycles. Breakout from the hot-CNO cycles leads to the rp-process and converts the initial CNO isotopes into heavier elements. Recent calculations have shown that the rp process ends with the Sn-Sb-Te cycle [15].

In recurrent novae, He, C and O accrete onto a CO white dwarf. The mass of the lighter star becomes greater than the Chandrasekhar limit leading to a *Type Ia Supernova.* The spectra of these show no H lines, however, Si, Ca, Ni and Fe are seen. The reader is referred to references [8, 10, 12, 13], for further details on explosive hydrogen burning. Figure 1.7 gives typical

temperature and density conditions for sites of explosive hydrogen burning.

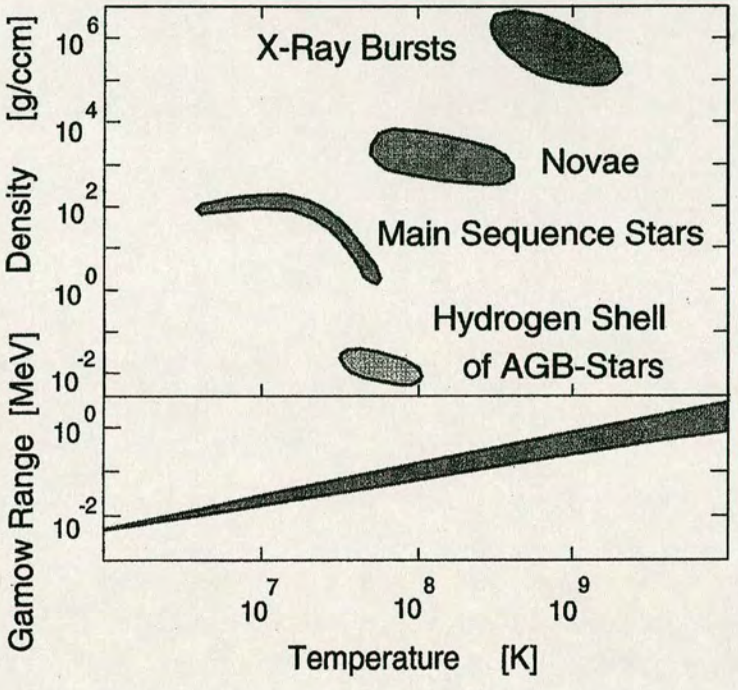

Figure 1.7: *Characteristic temperature and density conditions for stellar and explosive hydrogen burning environments. The lower part shows the Gamow energy range for the CNO reactions, adapted from [13].*

1.2 Thermonuclear Reactions in the Stellar Environment

1.2.1 The Gamow Window

In the stellar environment particles move at non-relativistic velocities in a non-degenerate gas and local thermodynamic equilibrium can be assumed. The Maxwell-Boltzmann distribution function can be applied to describe nuclei under these conditions. In 3-D the particle distribution (P) expressed as a function of velocity (V) is [16]:

$$P(V)\,dV = \left(\frac{m}{2\pi kT}\right)^{\frac{3}{2}} e^{-\frac{m(v_x^2+v_y^2+v_z^2)}{2kT}}\,dv_x\,dv_y\,dv_z \tag{1.5}$$

where $V = \sqrt{v_x^2 + v_y^2 + v_z^2}$, $dv_x\,dv_y\,dv_z$ is a small increment in velocity space, k is Boltzmann's constant, T is the absolute temperature and m is the particle mass. The transformation from $dv_x\,dv_y\,dv_z$ to dV is:

$$P(V)\,dV = \left(\frac{m}{2\pi kT}\right)^{\frac{3}{2}} e^{-\frac{mV^2}{2kT}}\,V^2\,4\pi\,dV \tag{1.6}$$

The number of particles with speed, V is given by $N(V) = N\,P(V)$ where N is the number of particles. Thus:

$$N(V)\,dV = N\,4\pi\,V^2\left(\frac{m}{2\pi kT}\right)^{\frac{3}{2}} e^{-\frac{mV^2}{2kT}}\,dV \tag{1.7}$$

In stellar environments nuclei frequently collide with one another with energies of the order of keV. This is very much less than the Coulomb potential barrier which is typically of the order of MeV. Particles have a probability

of tunnelling through this barrier. The tunnelling probability, or penetration factor, P is given by $P = e^{-G}$ where G is the Gamow factor. At low energies, $G \approx 2\pi\eta$ where η is the Sommerfeld parameter. Convolution of the Maxwell-Boltzmann distribution and the Coulomb barrier penetration factor gives rise to the Gamow peak (see figure 1.8). The Gamow window, ΔE_{G} is the energy range around the Gamow energy, E_{G} (where the reaction is most probable) given by [17]:

$$E_{\mathrm{G}} = 1.22\,(Z_1^2\,Z_2^2\,\mu\,T_6^2)^{\frac{1}{3}} \tag{1.8}$$

$$\Delta E_{\mathrm{G}} = 0.749\,(Z_1^2\,Z_2^2\,\mu\,T_6^5)^{\frac{1}{6}} \tag{1.9}$$

where Z_1 and Z_2 are the atomic numbers of the interacting particles, μ is the reduced mass and T_6 is the temperature in units of 10^6 K.

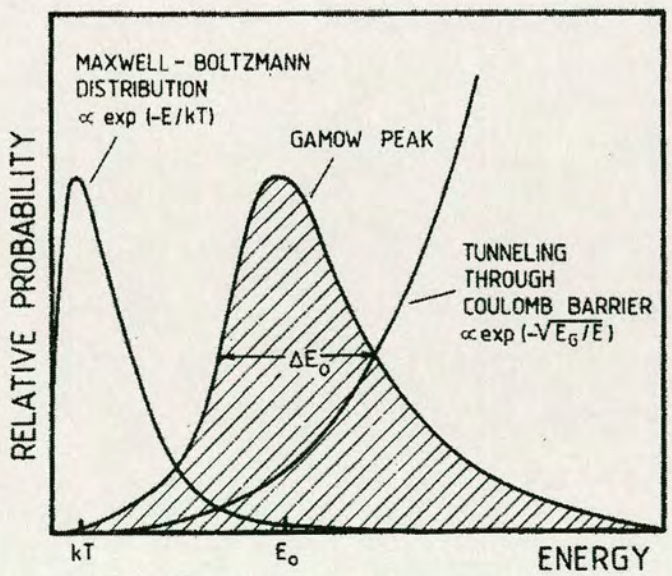

Figure 1.8: *The Gamow peak [18].*

1.2.2 Resonant Reactions

A reaction that leads to the formation of a compound nucleus which subsequently decays can be represented as a two-step process as follows:

$$a + X \rightarrow C^{\star} \rightarrow b + Y + Q \tag{1.10}$$

where C* is the compound nucleus state, b and Y are the exit channels (or decay mode) and Q is the Q-value of the reaction. The total width of a state, Γ is the sum of the partial widths for the possible decay channels i.e

$$\Gamma = \sum_{n} \Gamma_n \tag{1.11}$$

where Γ_n is the partial width for decay through some channel n.
The Breit-Wigner formula describes the cross section for the formation of a compound nucleus through channel α and subsequent decay through channel β. This is given by [16]:

$$\sigma_{\alpha\beta} = \frac{\omega\pi}{k^2} \frac{\Gamma_\alpha \Gamma_\beta}{(E - E_r)^2 + (\frac{1}{2}\Gamma)^2} \tag{1.12}$$

where $k^2 = \frac{2\mu E}{\hbar^2}$, E_{r} is the resonant energy and E is the interaction energy. In terms of the resonance strength, $\omega\gamma$, the above equation can be re-written as:

$$\sigma(E) = \frac{\pi}{k^2}\, \omega\gamma\, \frac{\Gamma}{(E - E_{\mathrm{r}})^2 + (\frac{1}{2}\Gamma)^2} \tag{1.13}$$

where the spin-statistical factor $\omega = \frac{2I+1}{(2I_{\mathrm{proj}}+1)(2I_{\mathrm{targ}}+1)}$ and $\gamma = \frac{\Gamma_\alpha \Gamma_\beta}{\Gamma}$

1.2.3 Stellar Reaction Rates

For non-identical particles 1 and 2, the reaction rate per unit volume is given by:

$$R_{12} = n_1\, n_2\, <\sigma v> \tag{1.14}$$

where n_1 and n_2 are the number densities of particles 1 and 2 respectively and $<\sigma v>$ is the product (velocity averaged) of cross section and relative velocity between the nuclei and is given by:

$$<\sigma v>_{12} = \int_0^\infty \int_0^\infty \phi(v_1)\, \phi(v_2)\, \sigma(v)\, v\, dv_1\, dv_2 \tag{1.15}$$

where v is the relative velocity, v_1 and v_2 are the absolute velocities of nuclei 1 and 2 respectively. Averaging over the Maxwell-Boltzmann distribution in terms of energy and substituting for $\sigma(E)$ yields:

$$<\sigma v> = \left(\frac{2}{\mu\pi}\right)^{\frac{1}{2}} \left(\frac{1}{kT}\right)^{\frac{3}{2}} \left(\frac{\hbar^2\pi}{\mu}\right) (\omega\gamma)\, \Gamma \int_0^\infty \frac{e^{-\frac{E}{kT}}}{(E - E_r)^2 + (\frac{\Gamma}{2})^2}\, dE \tag{1.16}$$

where μ is the reduced mass of the two nuclei, T is the temperature and E is the CM energy.

For a narrow resonance (i.e. $\Gamma \ll E_r$) this equation can be integrated to yield [9]:

$$<\sigma v> = \left(\frac{2\pi}{\mu kT}\right)^{-\frac{3}{2}} \hbar^2\, (\omega\gamma)\, e^{-\frac{E_r}{kT}} \tag{1.17}$$

On the other hand, if a resonance is broad then a Lorentzian shape can no longer be assumed. In this case the equation has to be solved numerically to obtain the reaction rate.

1.2.4 Network Calculations

A network calculation is a series of time dependent reactions that can be used to describe nucleosynthesis. The evolution of isotopic abundance, in time, is determined from the reaction rates for production and depletion of the isotope. Thus in general:

$$\frac{dN_i}{dt} = \sum_i N_{i-1} < \sigma v >_{i-1,i} - N_i < \sigma v >_{i,i+1} \tag{1.18}$$

where N_i is the abundance of a particular isotope. This can be applied to all isotopes in a reaction sequence resulting in a set of coupled linear first order differential equations.

As already mentioned, the stellar reaction rate is temperature dependent. In addition, the isotopic abundance is dependent on the density. Hence this also needs to be taken into account in network calculations, by giving initial conditions for isotopic abundances. The initial abundances of isotopes are set at the solar abundance. Further details of network calculations can be found in [19, 20].

1.3 The Need for Radioactive Ion Beams

Some of the reactions important to the CNO cycles and most of the rp-process involve those with unstable nuclei. These nuclei can have lifetimes longer than the time for burning in certain stellar events. At a temperature of ~1 GK, reaction cross sections are in the range of millibarns to microbarns.

For an understanding of such reactions, it is crucial to measure stellar reaction rates, $< \sigma v >$. These rates are strongly sensitive to temperature, therefore it is necessary to know the energy dependent cross section, $\sigma(E)$ of the reactions as accurately as possible.

There are two possible methods to measure such cross sections: the use of radioactive beams or radioactive targets. The target approach is favourable for nuclei that have half-lives of the order of days. The disadvantages of the target method, however, is that the target gives considerable background radiation and could also be contaminated.

^{18}Ne is a β-decaying isotope which does not exist naturally (as for many of the isotopes involved in stellar nucleosynthesis). Its very short half-life of 1.67s means that the target method is not feasible. Thus the use of a radioactive beam of ^{18}Ne is required.

At present there are two methods used for the production of radioactive ion beams. One of these, the Isotope Separation OnLine (ISOL) technique is used at Louvain-la-Neuve. See Chapter 2 for further details of the ISOL technique and its use in this work.

1.4 Experimental Approaches

Until recently the ^{18}Ne(α,p)^{21}Na reaction rate was based on the level structure of the compound nucleus, ^{22}Mg and its respective mirror, ^{22}Ne via charge exchange or transfer reactions. This approach gives a large uncertainty in the reaction rate which can only be removed by making direct measurements with radioactive beam induced reactions.

In order to measure the ^{18}Ne(α,p)^{21}Na reaction rate, the resonance parameters (E_r and Γ) and the resonance strength ($\omega\gamma$) for each level in ^{22}Mg must be evaluated with sufficient accuracy. A direct measurement of the cross section can thus be used to determine the reaction rate. ^{18}Ne has a 1.67s half-life and thus a direct measurement must be done using a ^{18}Ne beam on a helium target. This is not without its problems, however, as radioactive beams have low intensities and are generally poor in quality.

1.4.1 Previous Work

A direct measurement of the ^{18}Ne(α,p)^{21}Na reaction, in inverse kinematics, has been previously undertaken by Bradfield-Smith *et al* [21, 22]. This study utilised a post-accelerated radioactive beam available at Louvain-la-Neuve and a gaseous helium target. A ΔE-E technique using double sided silicon strip detectors (DSSSD) at 0° with respect to the beam line was employed, covering an energy region from 2.04 to 3.01 MeV in the centre of mass (CM) frame of the ^{18}Ne+α system. Protons were detected with energies between 3-10 MeV. This setup had a proton detection efficiency of ~2%, assuming an isotropic distribution of protons in the CM. Three levels in ^{22}Mg were identified with certainty at 10.91, 10.99 and 11.13 MeV (see figure 1.9).

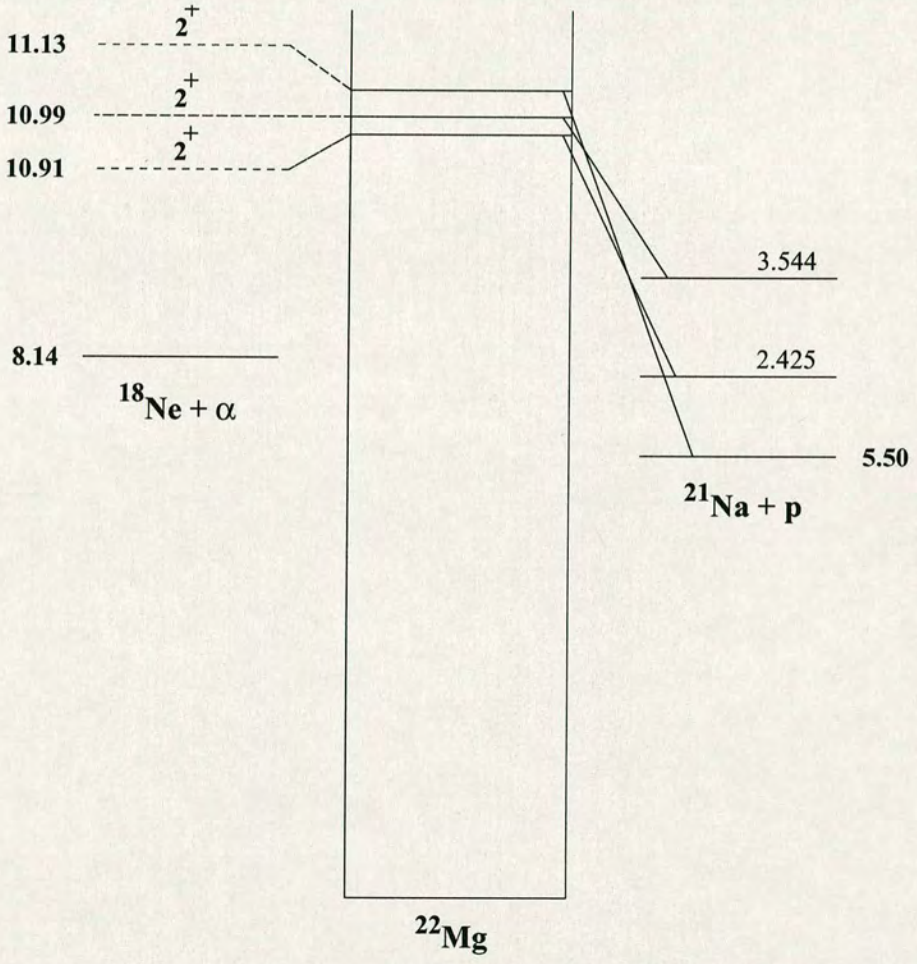

Figure 1.9: *Level diagram showing the states accessed in* ^{22}Mg from the previous direct measurement.

Other states could not be identified with any certainty due to an ambiguity in the assignment of the final state. Resonance strengths were extracted with an uncertainty of ~30%. The main source of this error was due to the uncertainty in the mean beam energy as the beam passed through the window and as it traversed through the gas. Furthermore, a large proton background (due to elastic scattering of protons from water vapour on the surfaces of all foils) was observed. The experimental stellar reaction rate showed reasonable agreement with theoretical predictions at and above a temperature of 2.5 GK. This reaction rate was applied to a one zone X-ray burst model, which showed that breakout via the ^{18}Ne(α,p)^{21}Na reaction was sufficient to trigger the burst and allow material to flow to higher mass.

1.4.2 The Present Work

The present work aims to extend the previous experiment [21, 22] by eliminating the proton background from the window, making a measurement at lower energy and attempting to observe other states in the level structure of ^{22}Mg below 10.58 MeV. To achieve this aim, a detector system of improved efficiency was constructed to measure the reaction over a lower energy range of ~1.70 to 2.90 MeV in the CM, appropriate for a nova outburst. A separate direct measurement of the energy profile of the ^{18}Ne beam as it passed through He gas, was undertaken to reduce a major source of uncertainty in the previous determination of the reaction rate.

A related experiment by Chen *et al* [23] looked at the ^{16}O(^{12}C,^{6}He)^{22}Mg reaction to populate states in ^{22}Mg above and below the α threshold. Eighteen new energy levels were discovered and this information provides a basis

which can be used for comparison.

Chapter 2

Experimental Procedure

2.1 Experimental Design

The main aim of the experiment was to improve the previous measurement of the ^{18}Ne(α,p)^{21}Na reaction. One major source of error, in the determination of the resonance strengths, is associated with the rate of energy loss of ^{18}Ne through the He gas. The first consideration was to reduce this source of error. To do this, a surface barrier detector (at 0° with respect to the beam line) was used to directly measure the energy of the ^{18}Ne beam as it entered the gas and as a function of distance within the gas.

The second consideration was to address the problem of proton background and the ambiguity in the assignment of the final state. An alternative geometry to that used previously was needed. Two possibilities were considered using the ΔE-E setup - one telescope at 45° and one at 90° with respect to the beam axis. Elastic proton events from the window could not be detected, due to the collimation provided by both geometries. A look at the

reaction kinematics of ^{18}Ne+^{4}He shows that elastically scattered ^{18}Ne ions could not be detected in either geometry, whereas elastic recoil alphas could be stopped in the ΔE detector (see appendix D.1).

A Monte Carlo simulation (written by W. Bradfield-Smith and D. Groombridge) allowed the two geometries to be compared. Proton events were created at various positions within the gas target, allowing the detection efficiency to be determined as a function of distance. Both geometries showed a similar efficiency over a possible region of interest. From the variation in proton energy as a function of angle, the 45° geometry was favoured as the excited states of ^{21}Na could be more easily resolved at forward angles. The proton tracking provided by this geometry allows the beam energy to be determined for any resonance, so reducing the ambiguity in the final state accessed in ^{21}Na.

In additon, a two-telescope system at either side of the beam line was used, giving symmetry and doubling the statistics.

The position of the telescope system was crucial to the success of the experiment. A local code "dedx" [24] was used to determine where the detectors would need to be placed so that proton yields may be observed from states in ^{22}Mg with E_{x}>10.00 MeV.

2.2 ^{18}Ne Beam Production

The Radioactive Ion Beam (RIB) facility at the Université Catholique de Louvain in Louvain-la-Neuve, Belgium was used to carry out the experimental work. This facility makes use of the Isotope Separation OnLine (ISOL) technique using a "coupled" cyclotron setup. A 30 MeV primary

H^- beam from CYCLONE30 bombards a lithium fluoride target held in a graphite matrix. ^{18}Ne is produced via a (p,2n) reaction on the target. The ^{18}Ne is extracted and sent to an electron cyclotron resonance (ECR) source which is optimised for producing ^{18}Ne in the 3^+ charge state. The ^{18}Ne ions are then sent to the CYCLONE110 accelerator where they are accelerated to the required energy (in this case 30 MeV, FWHM 1%) with an average intensity $\leq 10^6$ particles per second. A schematic of the accelerator setup is shown in figure 2.1.

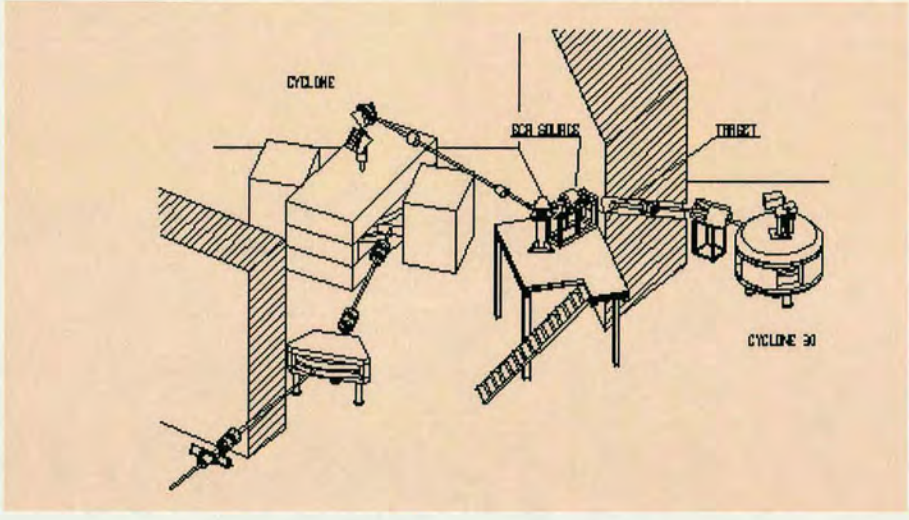

Figure 2.1: *^{18}Ne beam production at Louvain-la-Neuve.*

2.3 Charged Particle Detection and Identification

This work made use of specialised semiconductor detectors and therefore an overview of semiconductor theory and a description of the detectors used

will be given here.

2.3.1 Semiconductor Detectors

A semiconductor is a crystalline material which has a small band gap ($\sim$ 1.1 eV in silicon [25]). At room temperature, therefore, some electrons are promoted into the conduction band leaving behind holes in the valence band. Hence conduction occurs at room temperature. The amount of energy required to form an electron-hole pair is $\sim$eV which means that a semiconductor will have a better energy resolution than other types of detectors (see later).

However, there is a problem in detecting additional electron-hole pairs, produced by incident radiation, in the presence of thermally excited ones. This is overcome by using junctions between differently "doped" materials.

Silicon is a group IV element meaning that it has four valence electrons which try to form four covalent bonds with other atoms. Silicon can be doped with a group III element (e.g Boron) which has three valence electrons. In order to bond to four Si atoms in the lattice, this electron acceptor has to grab an extra electron forming a fixed negative ion and producing a mobile hole in the valence band. This forms p-type Si and has more positive charge carriers than negative ones. Alternatively Si can be doped with a group V element (e.g Phosphorus) which has five valence electrons. Four of these will bond to the surrounding four Si atoms leaving a spare electron. This extra electron is mobile and moves through the conduction band of the crystal leaving behind a fixed positive charge on the electron donor. n-type Si is formed and has more negative charge carriers than positive ones.

Both types of doping must be introduced into a single crystal so that the band structure runs right through. Doping thus significantly increases the concentration of "majority carriers", making the concentration of "minority carriers" very small.

Devices usually consist of a "junction" between n-type and p-type material. At these junctions electrons diffuse from n-type into p-type and holes diffuse from p-type into n-type, leaving behind their fixed charges. Diffusion stops when the electric field due to the fixed charges left behind is strong enough to prevent further motion. This gives a contact potential between two sides and a region around the junction with no majority charge carriers. This is the *depletion region* and normally only contains few minority carriers. When incident radiation produces electron-hole pairs by ionisation, they separate in the electric field due to the fixed charges. This is detected as a pulse as the separation of charges causes a drop in the potential across the region which can be amplified. A schematic of the depletion region is shown in figure 2.2.

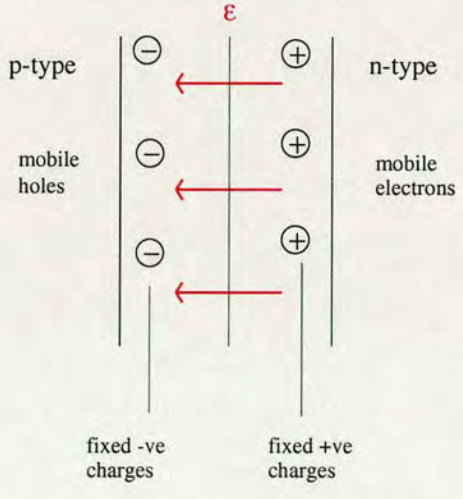

Figure 2.2: *A schematic of the depletion region in a semiconductor.*

A reverse bias is applied across the junction, pushing electrons further back into the n-type and holes further back into the p-type making the depletion region wider (giving a larger electric field across the region). This electric field has to be large enough to separate the electrons from the holes rapidly to prevent recombination. The thickness of the depletion region (d) is given by:

$$d \simeq \sqrt{\frac{2\varepsilon V}{e\,N}} \tag{2.1}$$

where V is the reverse bias voltage, N is the dopant concentration, e is the electronic charge and ε is the dielectric constant. Thus to get a large d, a large reverse bias is required. Fully depleted detectors are useful as ΔE detectors for particle identification. A 'telescope' of one thin ΔE detector and one (or more) thick E detector(s) can be used. Charged particles will lose part of their energy in the ΔE detector and lose the remainder in the E detector(s).

The energy lost is a measure of the stopping power $\frac{dE}{dx}$. Thus it is easy to distinguish between different elements because of the Z^2 dependence (see later).

The energy resolution (R) of a detector is given by:

$$R = \sqrt{\frac{F\,w}{E}} \tag{2.2}$$

where F is the Fano factor, ~0.1 for Si and w is the energy deposited per electron-hole pair, ~3.6 eV in Si [25]. In practice, however, this is limited by:

(i) incomplete charge collection (recombination) due to trapping sites in the crystal and the resulting fluctuations;

(ii) fluctuations in the leakage current (current which flows through the junction due to minority carriers);

(iii) noise in series resistance (Johnson noise);

(iv) noise in the external electronics;

(v) "straggling" in the energy loss in the dead layer at the surface of the detector (the metal contacts and an inactive layer of Si);

(vi) the effects of nuclear stopping.

2.3.2 Double Sided Silicon Strip Detectors

These are p-n junction devices with orthogonal strips on two faces of a silicon wafer. The detectors used in this work were manufactured by Micron Semiconductors Ltd. [30]. Figure 2.3 shows a schematic (not to scale) of the two sides of the detectors used.

The n-type substrate on the front of the detector is doped to form strips of p^+ regions. Metal contacts are applied on each strip. Silicon dioxide (SiO_2) separates the contacts ensuring these regions are non-conducting. The reverse biased p^+-n junction behaves as a diode. The two opposing diodes, with a 100 MΩ effective resistance [26], minimise conduction between p^+ regions.

The n^+ regions on the back of the detector give an ohmic contact with the metal contacts. To isolate adjacent strips, the n^+ regions are separated by p^+ regions. This gives an effective resistance of 10 MΩ [26].

As the bias is applied on the front side of the detector, a negative polarity voltage is required to reverse bias the junction.

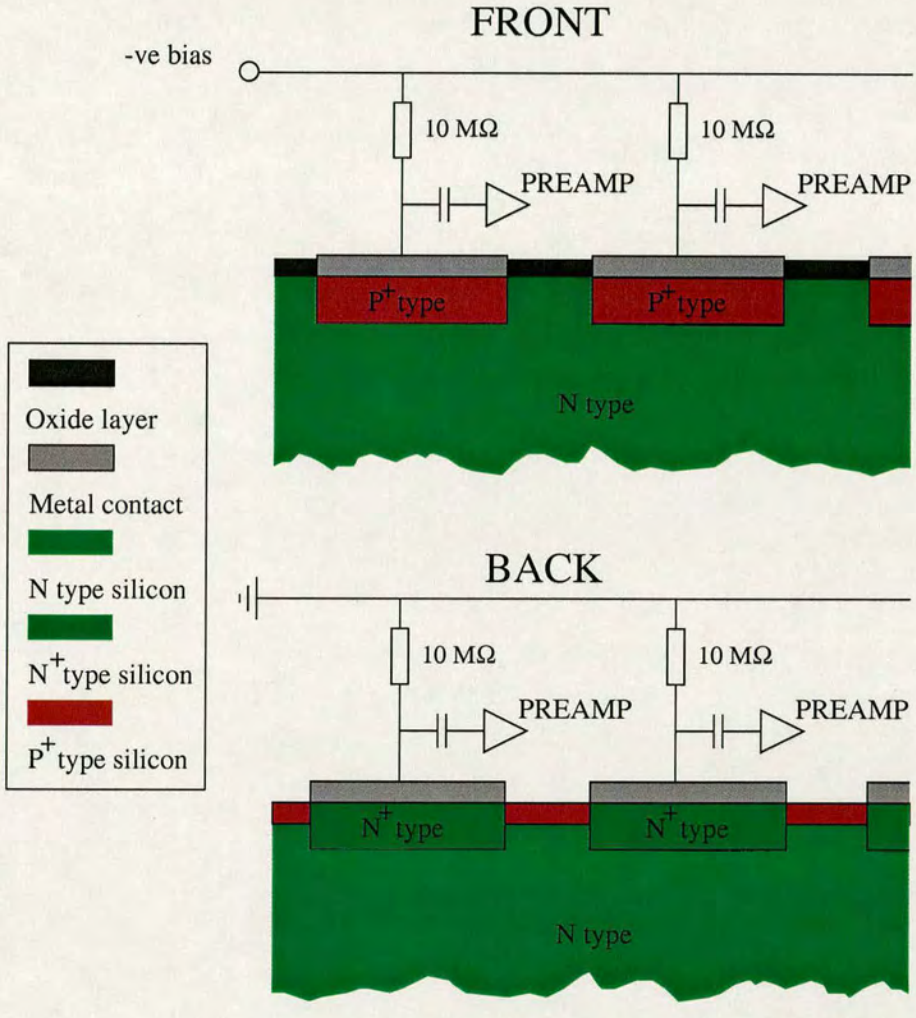

Figure 2.3: *A schematic of a double sided silicon strip detector, adapted from [21].*

2.3.3 Surface Barrier Detectors

These are detectors that are produced by starting with a n-type crystal of Si with the surface oxidised through exposure to air. This produces a large density of electron trapping sites so forming a thin p-type layer which acts as a junction. SBDs can also be produced by starting with a p-type crystal of Si and an n-type contact resulting from evaporating aluminium. These detectors are characterised by their very thin dead layers, typically 100nm or less [25]. Figure 2.4 shows a cross-section of a surface barrier detector.

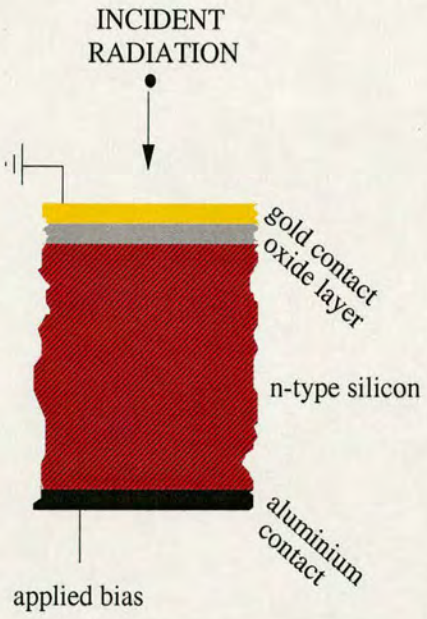

Figure 2.4: *Formation of a surface barrier detector, adapted from [31].*

The detectors used in this work were manufactured by EG & G ORTEC [32]. These require a positive polarity voltage to reverse bias the junction.

2.4 The Detector System

The experiment utilised a scattering chamber and a helium gas target previously developed for the investigation of (α,p) reactions with a radioactive beam.

The scattering chamber (see figure 2.5) consisted of two sections - a vacuum side for connection to the beam line and a larger gas target side filled with 500 mbar of He gas. In the vacuum side, two 200mm^2 surface barrier detectors located in the backward hemisphere were used for beam normalisation. Located in the forward hemisphere were two ΔE-E detector telescopes, positioned at 45° with respect to the beam line, used to detect charged particles. Each telescope consisted of a ΔE detector (DSSSD with 48×48 strips and pitch 335μm) and two E detectors (DSSSD with 16×16 strips and pitch 3mm). The telescope on the left hand side of the beam line (looking downstream) consisted of a 67μm ΔE detector with a 470μm E detector (*E1*) 5cm behind the ΔE and a 464μm E detector (*E2*) 1cm behind the *E1* detector. Similarly for the telescope on the right hand side of the beam line, but with detector thicknesses of 67μm, 478μm and 464μm for the ΔE, *E1* and *E2* detectors respectively.

The use of a movable platform allowed the detectors to be placed at the region of interest. The platform was positioned at a fixed distance from the window to give an energy scan of ~1.70 to 2.90 MeV in the centre of mass. Various foils were used in the chamber for different purposes. The first foil in the vacuum side was a 200μg/cm^2 Au foil. This allowed the Rutherford scattered beam particles to be used for beam normalisation (see later.)

A metallic window was used to separate the two sections of the chamber.

A 1.98mg/cm^2 Ni foil was used (with a 100μg/cm^2 Au flash in the vacuum side), allowing the gas to be at a pressure of 500 mbar and ensuring that the ^{18}Ne beam had the required energy upon entry into the target.

A 2mg/cm^2 Ni foil was used to stop the beam to ensure that the gas did not become contaminated with ^{18}F. This foil was attached to a wedge-shaped piece of aluminium which was placed between the two telescopes. This wedge also shielded the *E1* detectors from β^+ particles resulting from beam decay beyond the ΔE detectors.

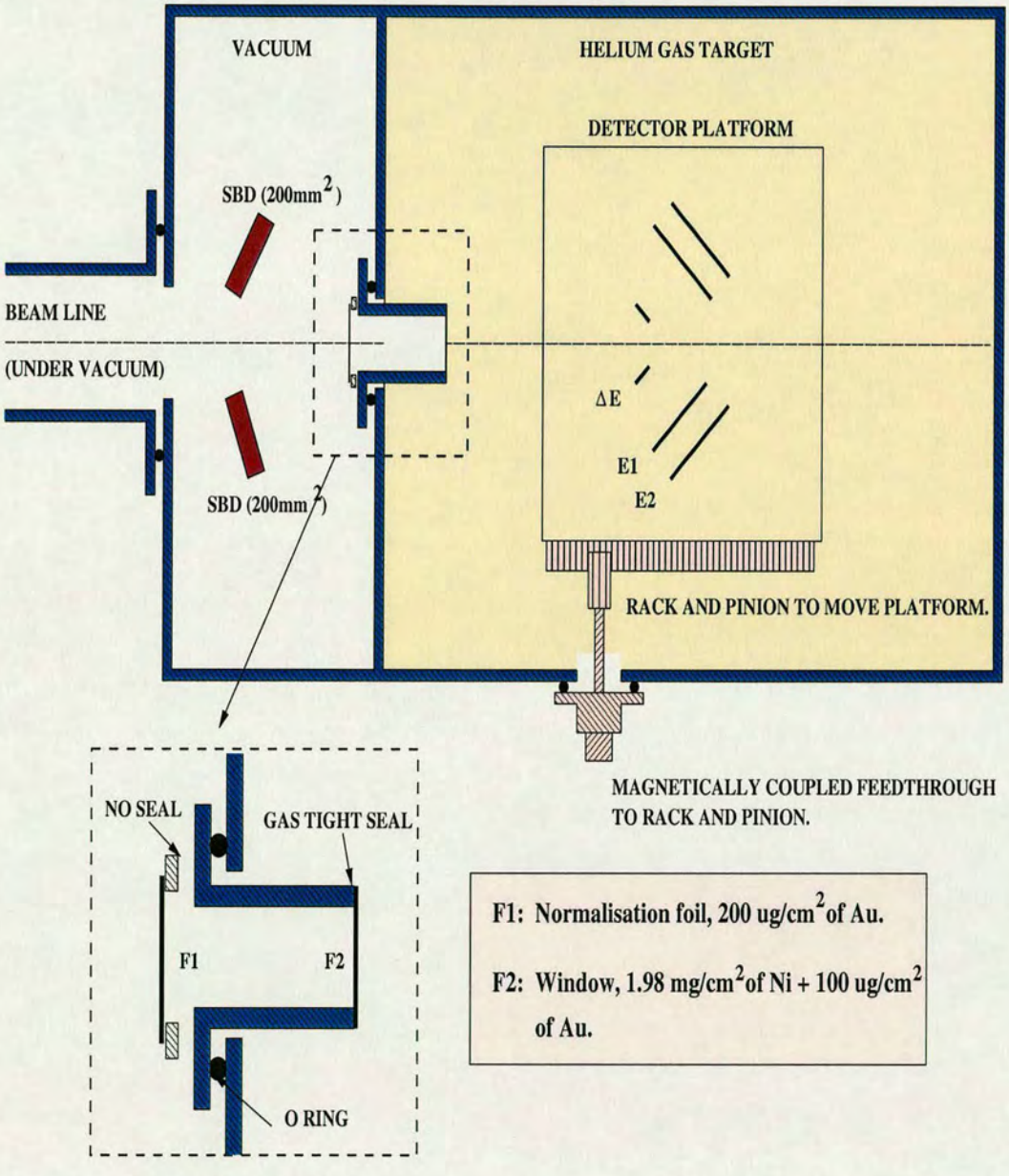

Figure 2.5: *A schematic of the scattering chamber. Note that the wedge shield is not shown on this figure.*

2.5 Electronics and Acquisition

2.5.1 Data Acquisition

As events are detected, they are amplified by charge sensitive preamplifiers (of type RAL108 designed by the Edinburgh Nuclear Physics Group and manufactured by the Rutherford Appleton Laboratory). The output from each preamplifier is connected to an 8 channel shaping amplifier (of type RAL109). These produce both analogue and logic signals which are sent to an Analogue to Digital Convertor (ADC) and a Time to Digital Convertor (TDC) respectively. The events are buffered in CAMAC crate controllers and the VME CPU builds these events, produces on-line spectra and writes the event data to tape.

The ADCs (8 channel Silena 4418/ V CAMAC ADCs) were used to record the energy signals for each strip detector channel (320 channels). TDCs (32 channel LeCroy 3377 CAMAC TDCs) were used to measure the time-of-flight of the reaction products. The two surface barrier detectors used for beam normalisation each had one ADC channel.

The logic signals are also used for the trigger to generate an ADC gate and the TDC common stop and to determine whether the digital signals need to be written to tape.

The reader is referred to [27] for further details on the instrumentation.

2.5.2 Trigger Logic

Before an event is read out, a gate is generated by taking a total OR of all the detectors in coincidence with the high frequency (HF) signal from the

cyclotron. This gives a relative time for the event.

If an event is read out to the VME, a clear signal to the ADC output register closes the gate. Subsequent events trigger the acquisition in the same way. The ECL signal from the shaping amplifiers starts the TDCs and the next HF pulse to arrive after a detected event stops the TDCs.

The trigger logic for the ΔE-E telescopes is shown in figure 2.6, the logic for the surface barrier detectors used to monitor the beam current is shown in figure 2.7 and that for the HF and TDCs is shown in figure 2.8.

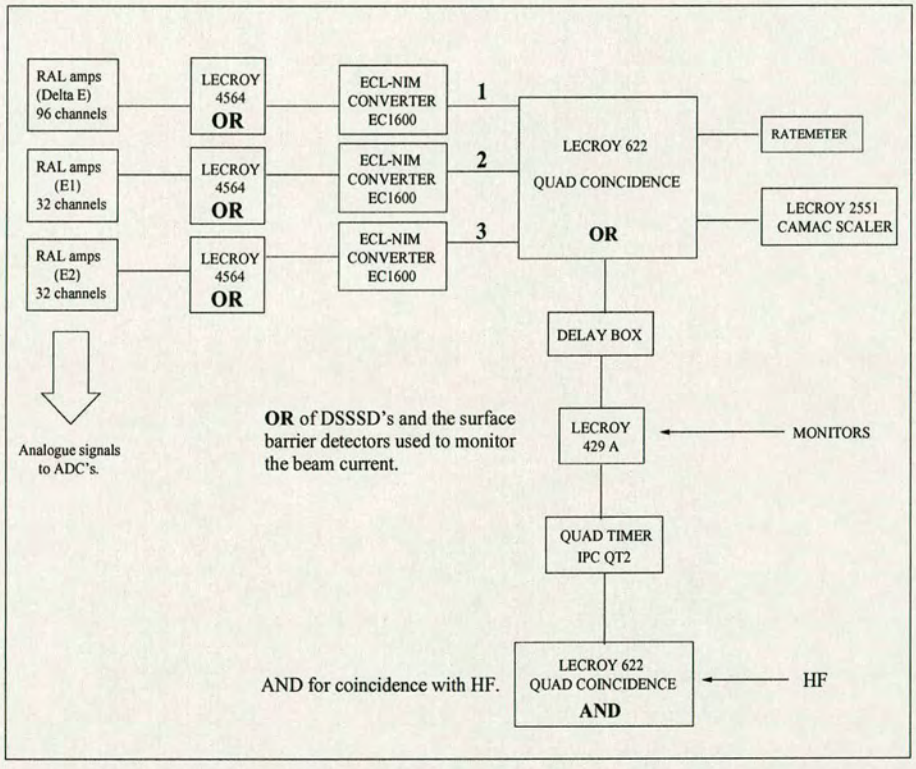

Figure 2.6: *Trigger logic for one of the proton telescopes.*

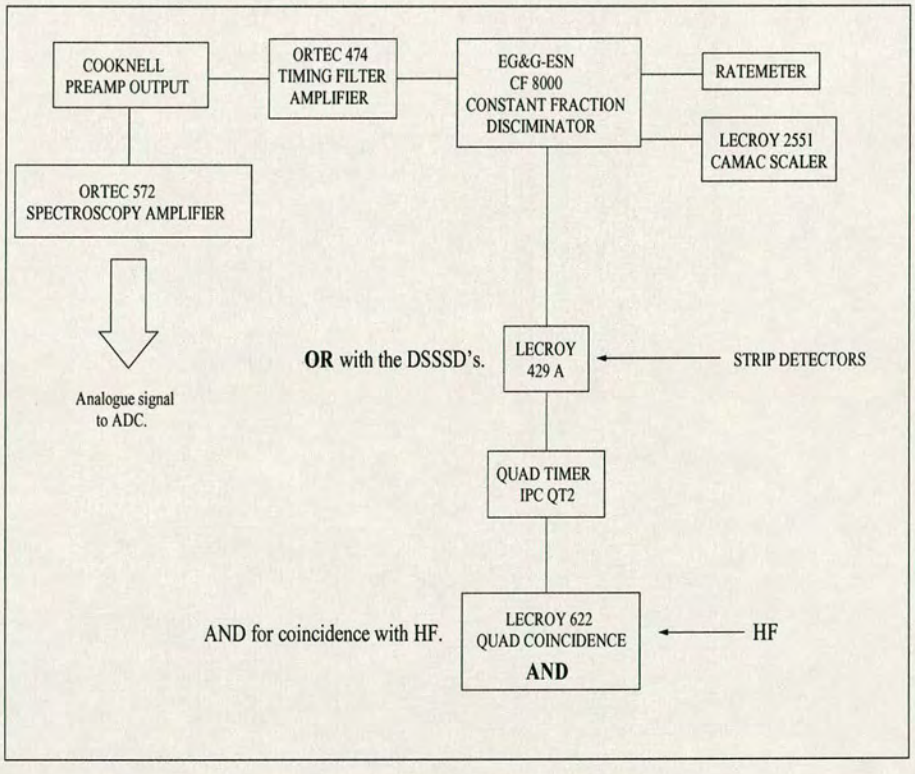

Figure 2.7: *Trigger logic for the monitor detectors.*

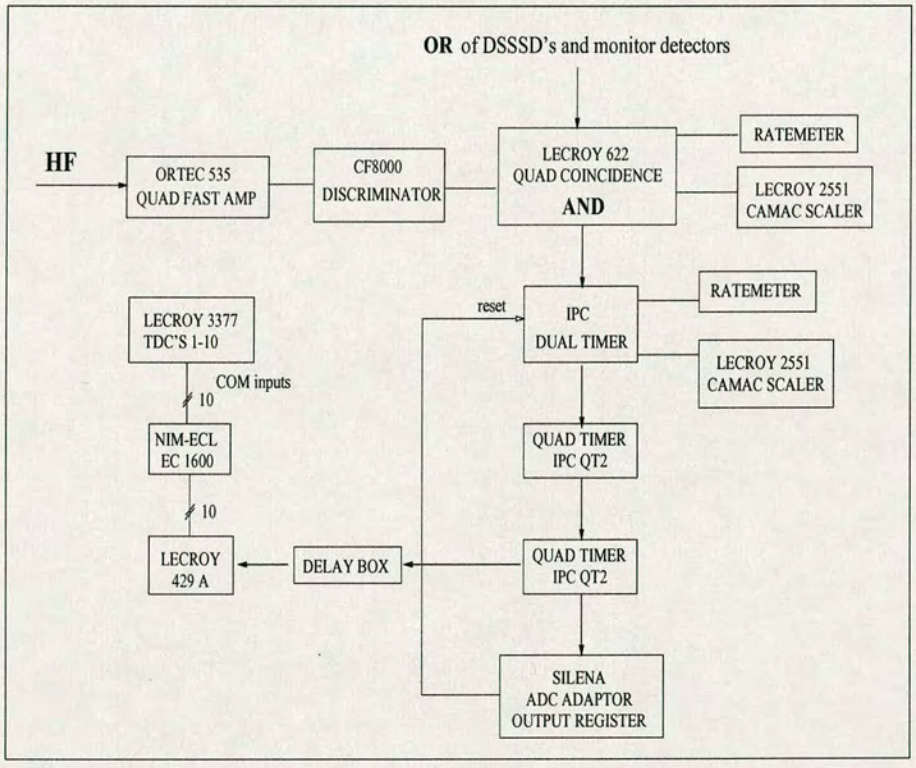

Figure 2.8: *Trigger logic for the HF and TDCs.*

2.6 Calibration

2.6.1 Energy Calibration

Each channel was instrumented one by one which means that they have different gains. Off-line, gainmatching can be applied to rescale each ADC to give absolute energy values.

A triple alpha particle source (^{239}Pu-^{241}Am-^{244}Cm) with well known alpha energies was used to carry out the calibration. The source was placed in front of each detector in turn. For the ΔE and *E1* detectors, the source was placed facing the side of the detector in which charged particles entered. However, due to space limitations on the platform, the source was placed facing the back of the *E2* detectors.

The gain for each channel is obtained once the energy loss in the dead layer (assumed to be 0.7μm silicon equivalent) of the DSSSD is corrected for.

2.6.2 Electronic Offset

In addition to having a different gain, each ADC channel also has a different d.c. offset. This electronic d.c. offset can be measured using a pulse generator. By feeding pulses directly into the preamplifiers at pulse heights of known ratio, a series of equally spaced pulser peaks result. Extrapolation of the zero gives the electronic offset.

After gainmatching, the energy per channel is 7.96 keV. A typical energy resolution of the alpha peaks is 40 keV FWHM and that of the pulser corresponds to an electronic noise of 20 keV FWHM.

2.7 Normalisation of the Beam Current

This was done using Rutherford scattered ^{18}Ne beam particles in the backward hemisphere (see figure 2.9).

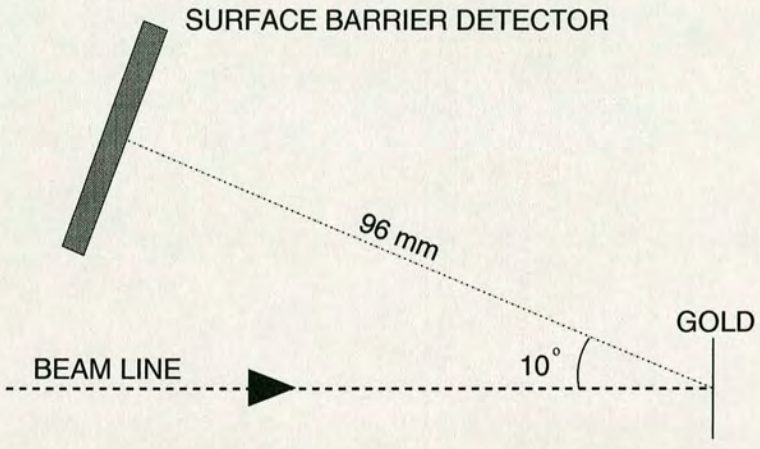

Figure 2.9: *Geometry of the surface barrier detectors.*

Nuclear interactions become possible for beam particles if the CM energy of the ^{18}Ne+^{197}Au system approaches that of the Coulomb barrier. The magnitude of the Coulomb barrier is given by [28]:

$$V_c = \frac{Z_1 Z_2 e^2}{4\pi \varepsilon_0 R} \tag{2.3}$$

where R is the sum of the radii of the two nuclei. For the ^{18}Ne+^{197}Au system, the Coulomb barrier is thus ~109MeV. As the beam energy was far below this energy, the scattering is therefore Rutherford. The differential cross section, $\frac{d\sigma}{d\Omega}$ for Rutherford scattering is given by [29]:

$$\frac{d\sigma}{d\Omega} = \frac{1}{4}\left(\frac{e^2}{4\pi \varepsilon_0}\,\frac{z\,Z}{2\,E}\right)^2 \frac{1}{\sin^4(\frac{\theta}{2})} \tag{2.4}$$

where z and Z are the atomic numbers of the projectile and target respectively, E is the energy of the projectile and θ is the scattering angle. This is considered to be constant over the angular range of the detector, allowing the integrated beam current to be calculated using [21]:

$$N_B = \frac{Y}{\frac{d\sigma}{d\Omega} N_T \Delta\Omega} \tag{2.5}$$

where Y is the elastic yield, N_{T} is the number density of the gold foil and $\Delta\Omega$ is the solid angle of the surface barrier detector.

EG & G ORTEC surface barrier detectors, with an area of 200mm^2 and a thickness of 150μm, were used on either side of the beam axis. This allows a check on whether the beam spot moved during the experiment. The solid angle for the detectors was 0.0194 sr.

2.8 The Direct Beam Profile Measurement

In a separate measurement, an EG & G ORTEC surface barrier detector, with an area of 50mm^2 and a thickness of 75μm, was mounted on the front of the platform (centred on the beam axis) to allow a direct measurement of the energy of the ^{18}Ne beam (with an intensity of $\sim 10^2$ pps) at three different positions within the He gas filled chamber (see figure 2.10). A measurement of the energy of the ^{18}Ne ions without any gas in the chamber was also undertaken, to give the energy of the ions upon exit from the Au+Ni window, giving a fourth point at d=0cm.

δ-electrons will be produced along the path of the incident ^{18}Ne ions (see appendix A.1 for details). Those δ-electrons emitted at small opening angles

could be detected causing a small increase in the measured pulse height. In order to deflect these δ-electrons, a metal plate (with a hole equal in diameter of the detector) was mounted in front of the detector. Measurements were made with 0V, +100V and +200V bias applied to the metal plate. This was found to have no effect on the observed pulse heights.

Furthermore, the detector was calibrated using a ^{239}Pu-^{241}Am-^{244}Cm triple alpha source and the electronic offset was measured with the pulser set at amplitudes of 110% and 10%. An electronics diagram is shown in figure 2.11.

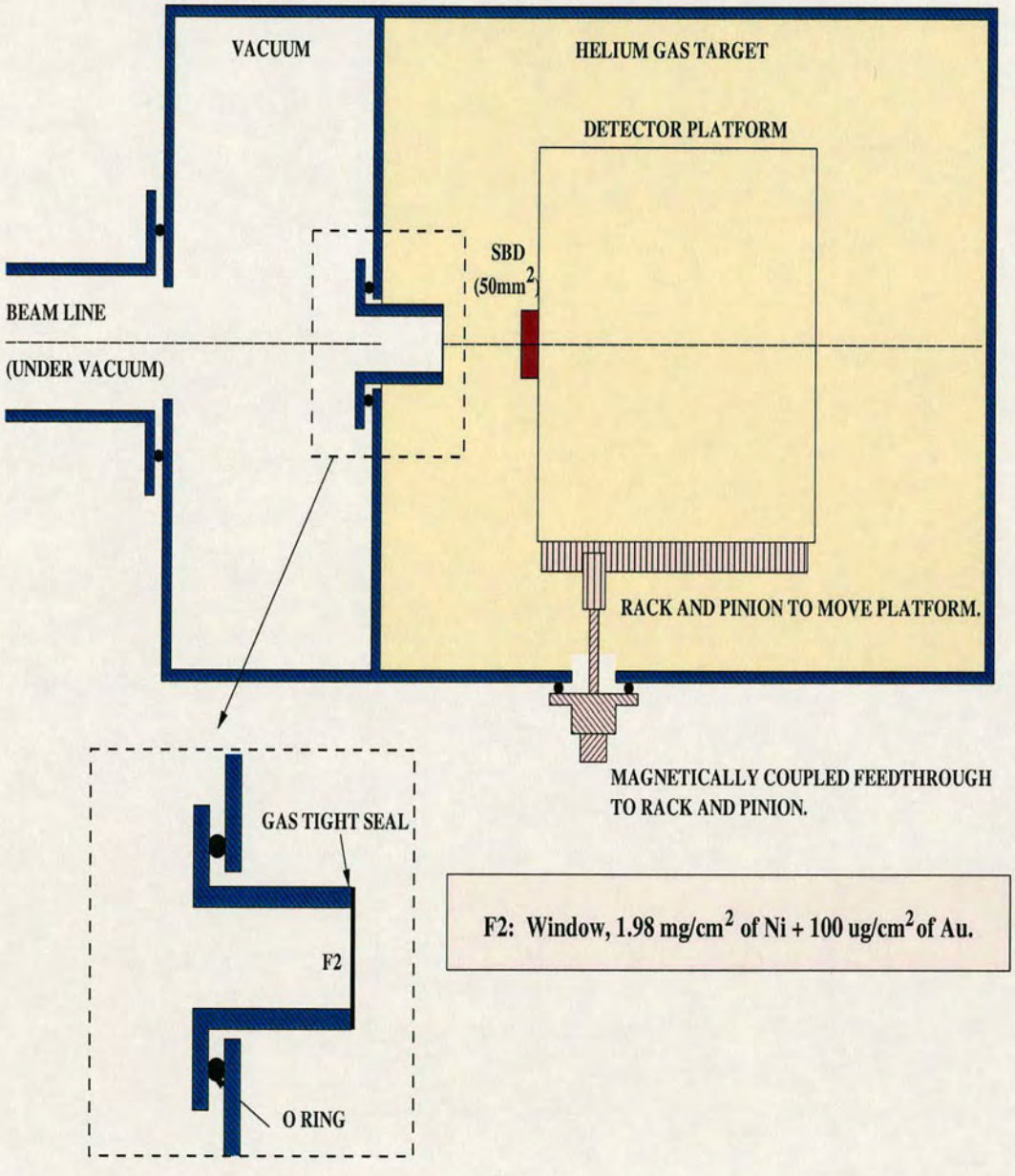

Figure 2.10: *A schematic of the experimental arrangement used for the beam profile measurement.*

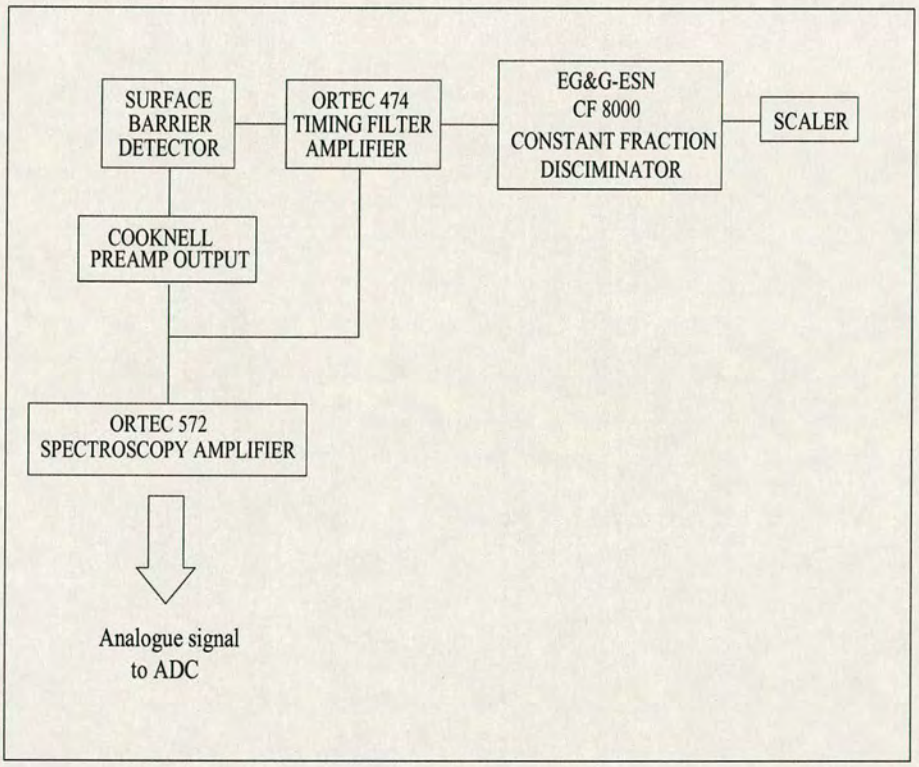

Figure 2.11: *An electronics diagram for the beam profile detector.*

Chapter 3

Analysis and Results

3.1 The ^{18}Ne Energy Profile

3.1.1 Problems with Calculating Energy Losses in Helium Gas

In the literature there are a few experimental results on energy loss and energy straggling of heavy ions in gaseous targets (see [33, 34, 35] and references therein). Incident ions lose most of their energy through interactions with the electrons of a target atom (see appendix A.1 for details on energy loss processes). It is difficult to calculate the energy loss of ions in He gas because He atoms exist in both singlet and triplet states (see figure 3.1). It is thus difficult to know which state an electron is in at any particular point along the path of interaction. In other words, the ionisation potential depends on the state in which the atom is in. Existing programs such as "dedx" use a parameterisation of the Bethe-Bloch formula, which assumes

an average ionisation potential. The above argument explains why such programs give inaccurate energy losses for ions passing through He gas. This makes the need for a direct measurement crucial.

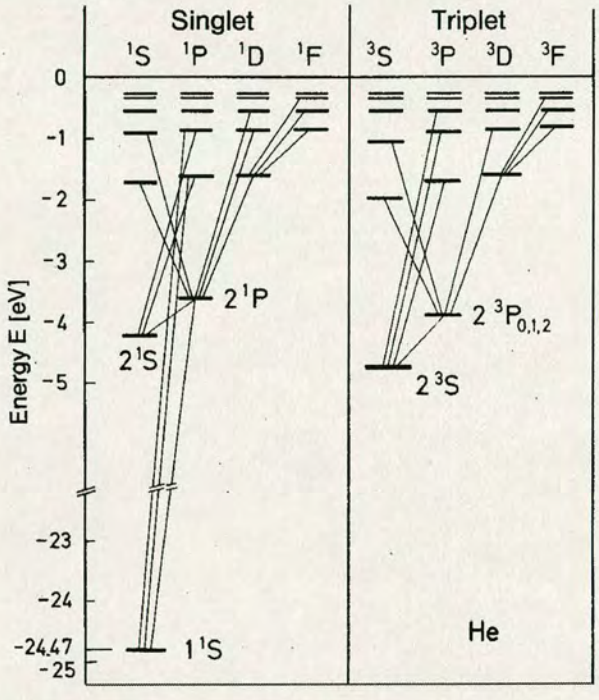

Figure 3.1: *A term diagram for the helium atom. Some of the allowed transitions are indicated. There are two term systems - singlet and triplet, between which transitions are forbidden [36].*

3.1.2 The Direct Measurement

Figure 3.2 shows the pulse height spectrum of the ^{18}Ne ions at 3 different positions in He gas and the measurement without any gas in the chamber, using the apparatus shown in figure 2.10. The energy of the beam before passing through the window was 30 MeV and the gas pressure was 500 mbar. The difference in yield for the measurement without any gas in the chamber

is due to a shorter measurement time.

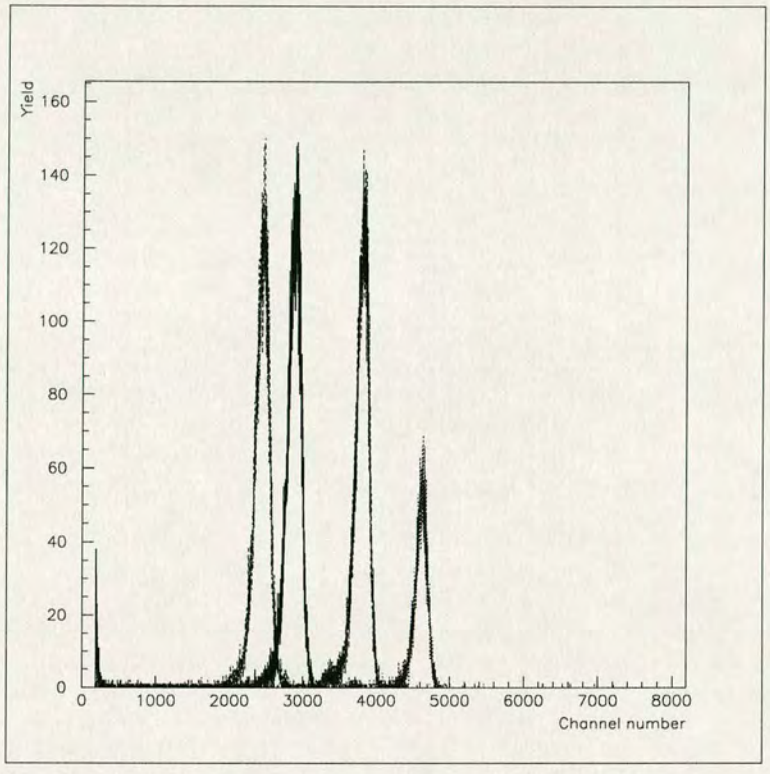

Figure 3.2: *Pulse height spectrum of the ^{18}Ne ions.*

Gaussian fits were applied to extract the centroid and width of each peak. The results from this fitting can be seen in table 3.1. The α calibration was used to determine the beam energy from the centroid of each peak.

D (mm)	Centroid (ch.)	Energy (keV)	σ	FWHM (keV)
0	4483.1±0.6	15859(14)	79.8±0.7	665.5±5.7
19(2)	3669.5±0.4	12900(8)	86.0±0.5	710.8±4.2
41(2)	2741.9±0.4	9526(10)	90.8±0.4	742.2±3.6
51(2)	2309.8±0.4	7955(12)	94.8±0.5	768.5±4.3

Table 3.1: *Results of the Gaussian fitting to the beam profile data.*

Applying a +100V and a +200V bias to the plate in front of the detector had no effect on the observed pulse height. This is likely to be due to the low intensity of the ^{18}Ne beam, producing very few δ-electrons.

The pulse height response of a Si surface barrier detector to heavy ions has been studied extensively [37, 38, 39]. There is a characteristic difference between the true ion energy and that as measured by a detector calibrated with alpha particles. This difference is known as the *pulse height defect* and is due to three processes: (i) the energy loss in the dead layer of the detector; (ii) energy loss due to nuclear stopping and (iii) the contribution from the recombination of electron-hole pairs in the plasma produced along the ionised track. The contributions from (ii) and (iii) are small and were thus neglected. Hence the energies were only corrected for energy loss in the dead layer of the detector. The dead layer was assumed to have a thickness of 50nm [26]. A SRIM2000 [40] calculation determined that 16 MeV ^{18}Ne ions lose $\sim$111 keV through a 50nm Si-equivalent dead layer.

Measurement of the ^{18}Ne beam seems to show a linear relationship between beam energy and distance traversed within the gas (over an energy range of 8-16 MeV). Indeed, a linear fit gives the best fit to the data. This gave an energy loss of (1.55 ± 0.01) MeV/cm and (15.96 ± 0.02) MeV for the energy of the ^{18}Ne beam upon entry into the gas.

Figure 3.3 shows how the energy of the ^{18}Ne ions varies as a function of distance through He gas (at 500 mbar). It can clearly be seen that the program "dedx" significantly underestimates the energy loss of ^{18}Ne ions through He gas. However, this result is in very good agreement with SRIM2000. Further details on the use of SRIM2000 is given in appendix A.

Furthermore, the width of the peaks in figure 3.2 gives an idea of the energy

straggling of ^{18}Ne ions in He gas (see table 3.1).

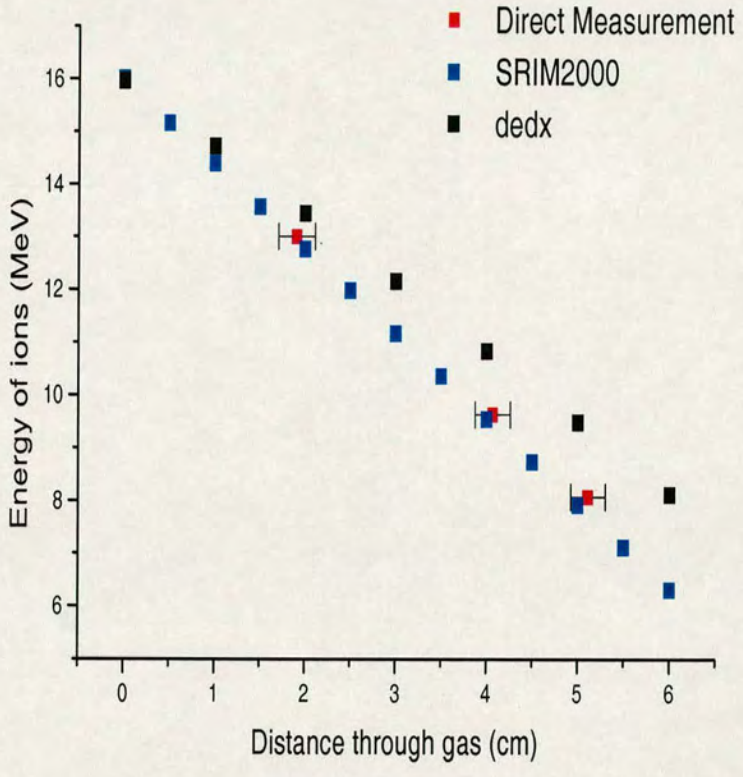

Figure 3.3: *The direct measurement of the* ^{18}Ne energy profile compared with results from the programs "dedx" and SRIM2000. Note that the measured point for d=0cm has been overlapped.

3.2 The ^{18}Ne(α,p)^{21}Na Reaction

The detectors were used to detect the reaction protons which populate the ground state and excited states in the residual nucleus, ^{21}Na. Kinematic information from these protons can be used to provide information on the level structure in the compound nucleus, ^{22}Mg. Details on how this was accomplished will be discussed in this section.

3.2.1 Analysis Procedure

The local program "sort-shell" [41] was used to read and unpack the data contained on the tapes. A user supplied routine allows data to be analysed on an event by event basis. This program enables defined spectra to be incremented.

The use of the ΔE-E telescope technique allows the identification of particles. The proton loses ΔE of its energy through the ΔE detector and the remainder is deposited in the E detectors (*E1* for low energy proton events, *E1* and *E2* for high energy proton events). Figure 3.4 shows 2-D energy spectra for the left and right proton telescopes (looking downstream) for an entrance beam energy of 15.96 MeV and a He gas pressure of 500 mbar. The energy recorded in the ΔE detector is plotted on the x-axes and the sum of the energies recorded in each detector is plotted on the y-axes. A calculation performed using SRIM2000 determined that a proton would need an energy >8.5MeV in order to be detected in the $E2$ detector (incident perpendicular to the detector surface). It can be seen in figure 3.4 that only a few high energy protons penetrate the left hand side *E1* detector. As no such events were detected in the other telescope, these events were rejected and treated

as random events.

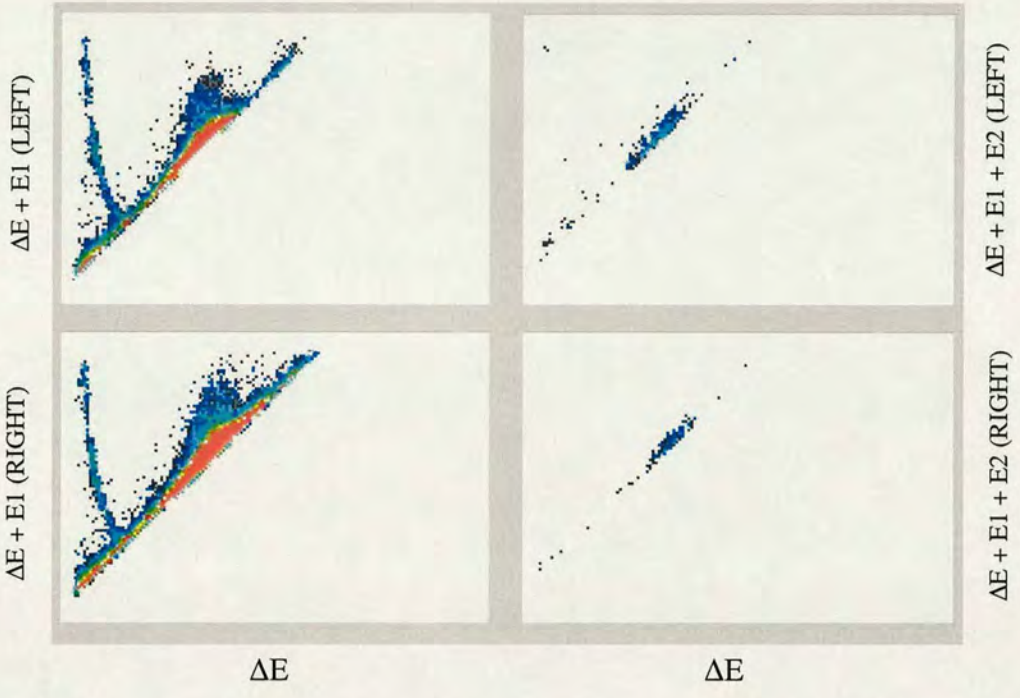

Figure 3.4: *2-D energy spectra for the left (upper) and right (lower) proton telescopes. ΔE vs. E1 are shown on the left hand side and ΔE vs. E1 + E2 are shown on the right hand side.*

A 2-D window can be used to select these proton events of interest. The initial energy of the proton, upon production, is the sum of energies in each detector it passes through and the energy losses through the various media (He gas and the detector dead layers). The local code "dedx" was used to calculate the energy loss of the protons through He gas and the detector dead layers. The inaccuracy in this energy loss is $\sim$10%.

The initial energy of the proton depends on its trajectory as this determines the thicknesses of the materials through which the proton passes. The trajectory of the proton can be reconstructed by knowing which of the detector strips fired. The region in-between the strips has a complicated electric field

and thus an event may cause adjacent strips to fire. In order to reject these interstrip events, a multiplicity condition was used where the number of strips that fire on the front must equal the number of strips that fire on the back of each detector. In addition, the condition of equal energy signals on the front and back of the detectors is also imposed.

The strips on the front and the back are orthogonal to one another and thus each event is located within "quasi pixels". Knowledge of the X and Y positions of the proton in the detectors allows the angle between the beam axis and its trajectory to be determined. Events were assumed to hit the centre of these pixels. This gives an error in the angle of 2°, corresponding to a 5% error in the thickness of materials.

Conversion from the frame of reference of the detectors to the frame of reference of the beam line allows an equation of a straight line to be used to determine every point on a proton's trajectory.

Calculation of the minimum perpendicular distance between the vector representing the trajectory of the proton and the vector representing that of the beam axis showed that, for all protons, this distance was $\leq$0.5cm. A cylindrical column of gas was assumed with a diameter therefore of 1cm (equal to that of the window), where the reactions take place (see figure 3.5.)

The two points where the straight line crosses the cylinder (Z_1 and Z_2) define upper and lower limits on the distance from the window (and hence lower and upper limits on the beam energy respectively).

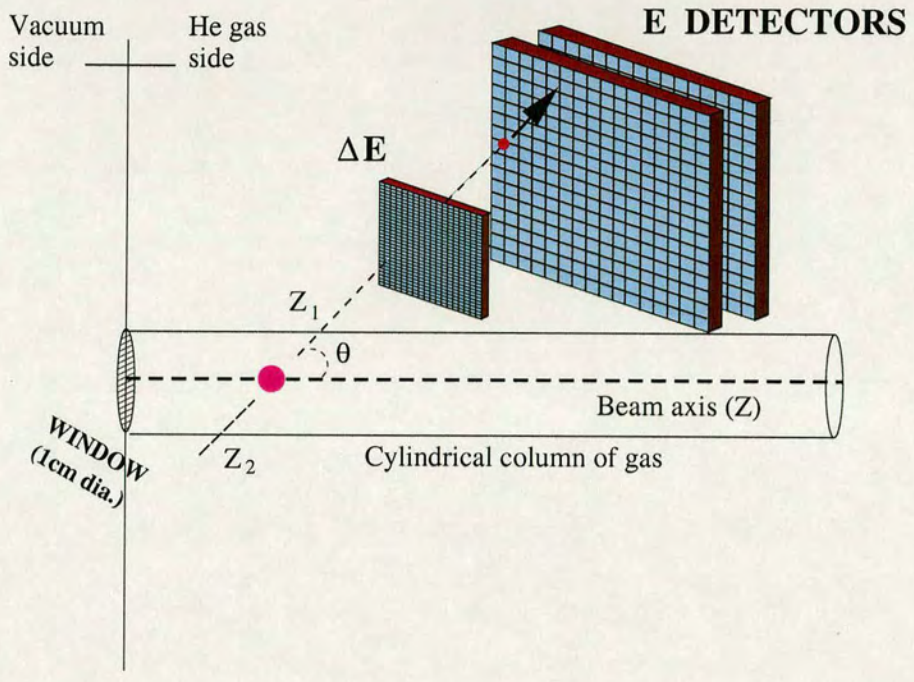

Figure 3.5: *A schematic showing how a proton is tracked. Note that only one proton telescope is shown.*

Figure 3.6 shows an energy spectrum for single proton events (not angle corrected). Each proton event has been corrected for energy loss in the detector dead layers and in traversing through He gas. The energy resolution of the detectors was determined from the α calibration. This was then scaled for protons. The proton energy resolution of each telescope, where the contributions from each detector are summed in quadrature, is ~40 keV FWHM. The total error in the energy loss correction is ~11%, corresponding to ~50 keV FWHM. The final uncertainty in the proton energy is then the quadrature sum of these two contributions and is thus ~64 keV FWHM.

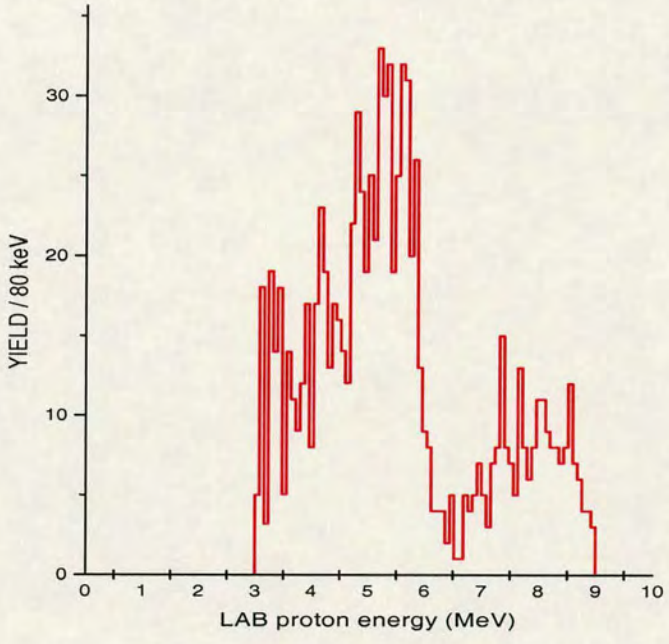

Figure 3.6: *Proton LAB energy spectrum (both telescopes are summed.)*

3.2.2 Detection Efficiency

The use of an extended gas target allows a range of energy levels in the compound nucleus, ^{22}Mg to be scanned. These levels correspond to a resonance energy which is dependent on the distance from the window, since a position in the gas can be related to the energy at which the reaction occured through a knowledge of the rate of energy loss of the beam in the gas. As protons can originate from any position within the assumed cylinder of gas, the target is not fixed in relation to the detectors. The detection efficiency is thus a function of position (or CM energy) and the final state accessed in the residual nucleus, ^{21}Na. The yield of protons from a particular resonance is needed in determining the resonance strength. A knowlege of the efficiency function of the detectors is therefore crucial. However, only a certain fraction of the total proton yield can be detected by the telescopes, as the experimental set-up only scans a limited angular range ($26° \leq \theta \leq 65°$). Hence the total yield depends on $\frac{d\sigma}{d\Omega}$ which is not known. The angular distribution of particles emitted from a compound nucleus, leading to a definite state in a residual nucleus, can be calculated by making assumptions about the spins and the resonance parameters as detailed in appendix C. This can then be taken into account in the determination of the efficiency function. Details on the calculation of the efficiency function can be found in appendix B. Efficiency spectra for protons accessing the ground state and the first 7 excited states in ^{21}Na are shown in figures 3.7 and 3.8. Protons accessing the 3^{rd} and 4^{th} excited states in ^{21}Na were assumed to have an isotropic angular distribution in the CM. This is due to these states being spin $1/2$, which gives a compound state spin possibility of 0 or 1 for outgoing

protons having an angular momentum of ℓ=0 or 1 respectively.

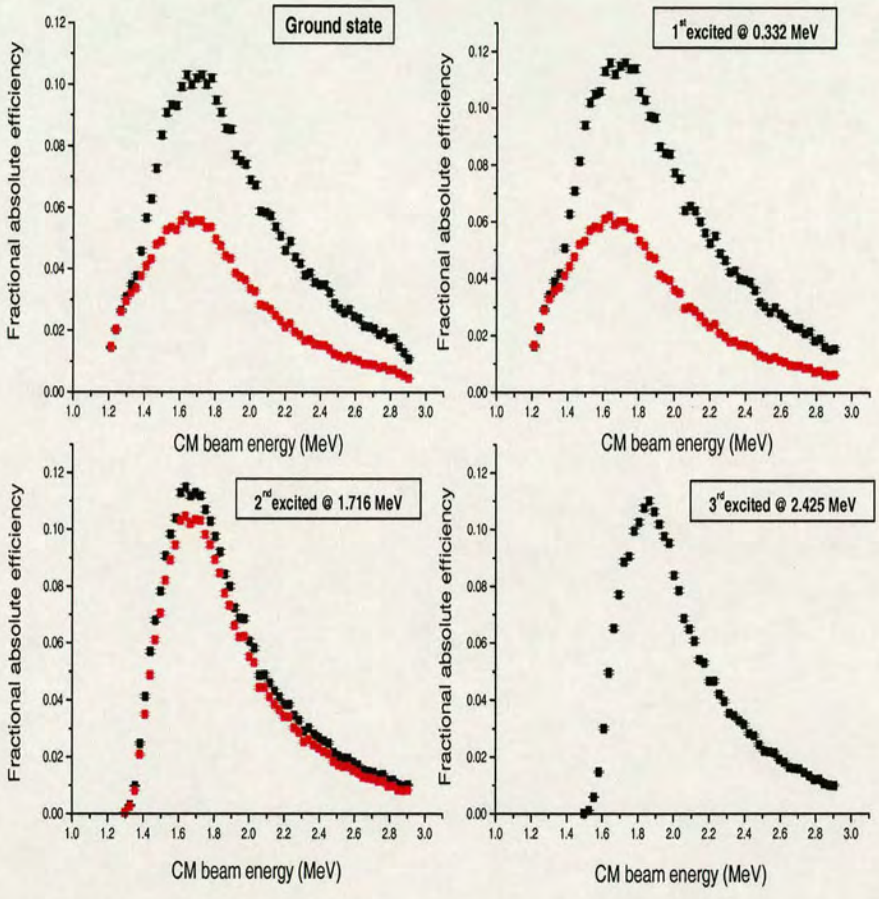

Figure 3.7: *Variation in efficiency as a function of CM energy. The black curve shows the efficiency taking into account the angular distribution of protons whereas the red curve shows the efficiency assuming an isotropic distribution of protons.*

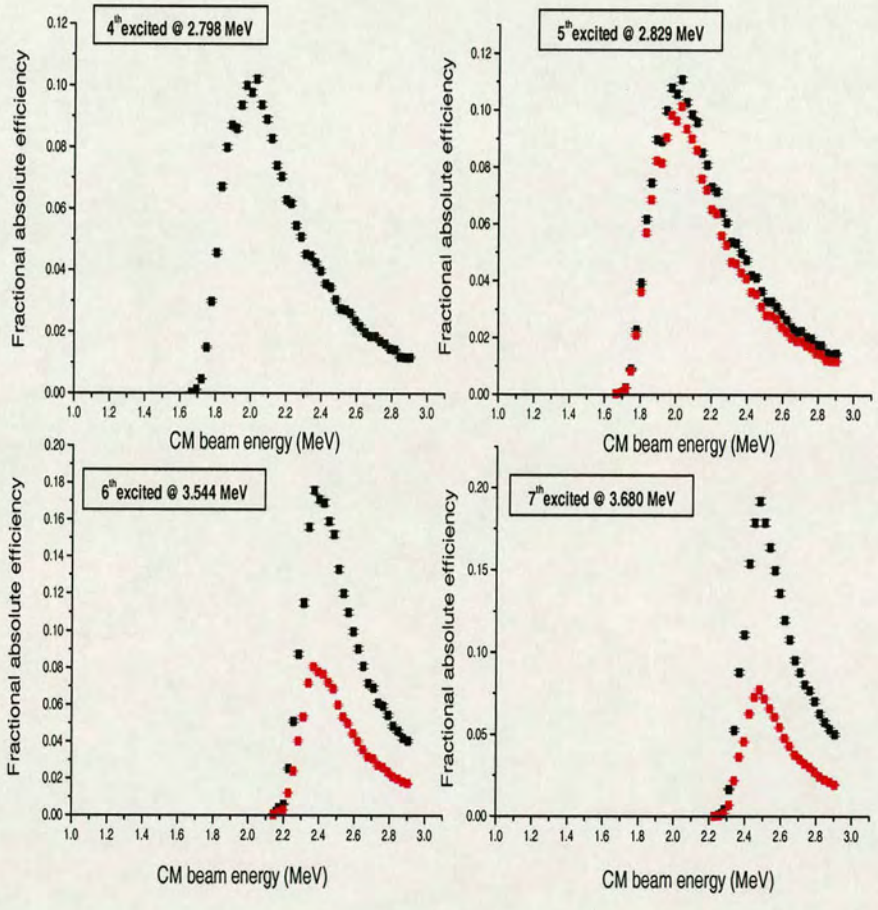

Figure 3.8: *Variation in efficiency as a function of CM energy. The black curve shows the efficiency taking into account the angular distribution of protons whereas the red curve shows the efficiency assuming an isotropic distribution of protons.*

3.2.3 Beam Energy Reconstruction

Once the laboratory energy and angle of emission of the protons are known, together with an assumption of the state accessed in the residual nucleus, the energy of the beam particle responsible for the reaction can be determined from two-body kinematics (see appendix D.2 for details). The CM beam energy was reconstructed, on an event by event basis, for protons accessing the ground state and the first 7 excited states in ^{21}Na with excitation energies of 0.332, 1.716, 2.425, 2.798, 2.829, 3.544 and 3.680 MeV and spins of $3/2^+$, $5/2^+$, $7/2^+$, $1/2^+$, $1/2^-$, $9/2^+$, $5/2^+$ and $3/2^-$ respectively [42].

One feature of this work is that the position information (provided by the tracking) can be used with the energy loss information described in section 3.1.2. This has the advantage of reducing any ambiguity in the assignment of the final state. Only those events with a reconstructed CM beam energy lying within the upper and lower limits from the tracking were accepted. This in turn gives information on the population of states in the compound nucleus, ^{22}Mg. The errors in these limits arise from the 2° error in the angle and corresponds to a CM energy of ± 0.22 MeV.

Before any reliable fits can be applied to this data, the spectra must first be corrected for the change in efficiency with CM beam energy. Figures 3.9 to 3.20 show efficiency corrected beam energy spectra for the various possible state assignments. In all cases, the raw data is shown in the upper graph, the efficiency corrected data is shown in the middle graph and Lorentzian fits to the efficiency corrected data are shown in the lower graph.

Lorentzian fits were applied to extract the resonance parameters, E_r and Γ. The results of which are summarised in tables 3.2 and 3.3.

^{21}Na state (MeV)	E_r (MeV)	Γ (MeV)
0.0	2.28±0.05	0.22±0.15
	2.52±0.01	0.10±0.05
	2.78±0.01	0.12±0.02
1.716	1.98±0.01	0.10±0.02
	2.17±0.03	0.15±0.09
	2.41±0.01	0.16±0.03
2.425	2.73±0.01	0.21±0.02
3.544	2.87±0.01	0.10±0.02

Table 3.2: *Results from Lorentzian fitting to cases where a unique state assignment can be made in* ^{21}Na.

^{21}Na state (MeV)	E_r (MeV)	Γ (MeV)
0.0	2.27±0.03	0.21±0.10
	2.55±0.01	0.19±0.04
0.332	2.74±0.01	0.30±0.04
1.716	2.35±0.01	0.12±0.03
	2.12±0.01	0.07±0.03
2.425	2.63±0.03	0.12±0.09
	2.85±0.01	0.08±0.02
2.798	2.06±0.01	0.09±0.03
	2.52±0.01	0.15±0.02
2.829	2.54±0.01	0.11±0.01
3.544	2.73±0.01	0.13±0.03
3.680	2.84±0.01	0.08±0.02

Table 3.3: *Results from Lorentzian fitting to cases where 2 state assignments can be made in* ^{21}Na.

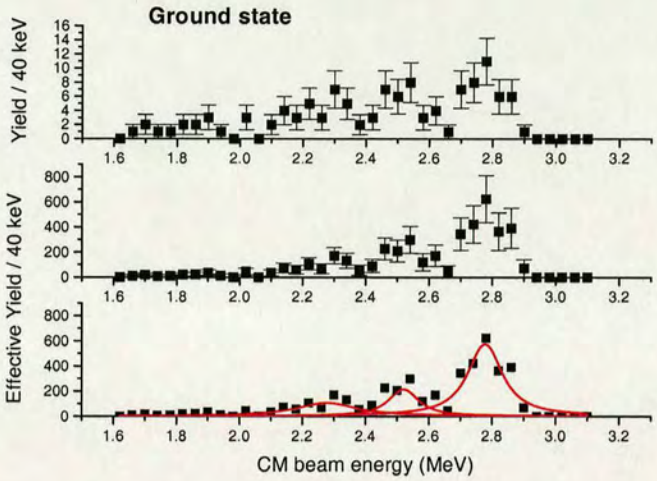

Figure 3.9: *Beam energy spectra for proton events where a ground state assignment can uniquely be made in* ^{21}Na.

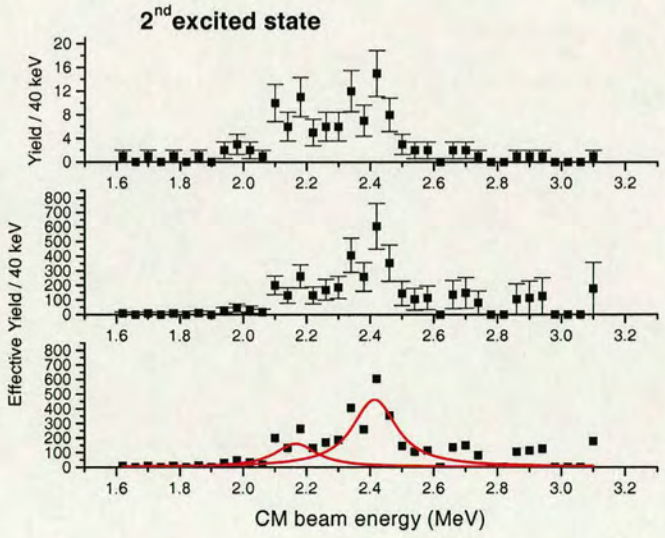

Figure 3.10: *Beam energy spectra for proton events where a* 2^{nd} *excited state assignment can uniquely be made in* ^{21}Na.

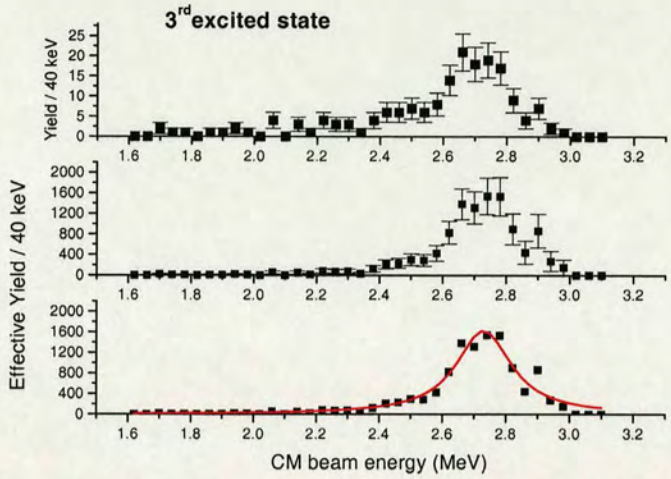

Figure 3.11: *Beam energy spectra for proton events where a 3rd excited state assignment can uniquely be made in* ^{21}Na.

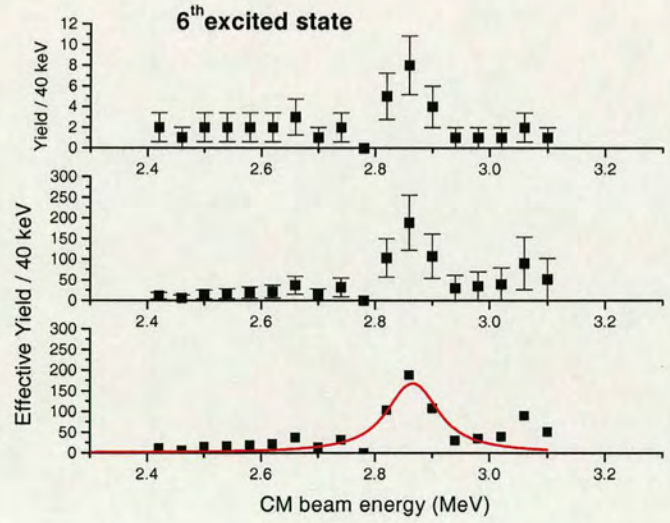

Figure 3.12: *Beam energy spectra for proton events where a 6th excited state assignment can uniquely be made in* ^{21}Na.

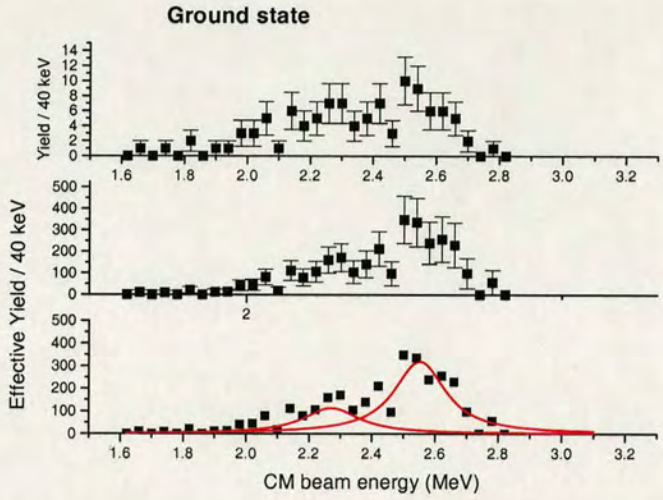

Figure 3.13: *Beam energy spectra for proton events where ground state and 1st excited state assignments can be made in* ^{21}Na .

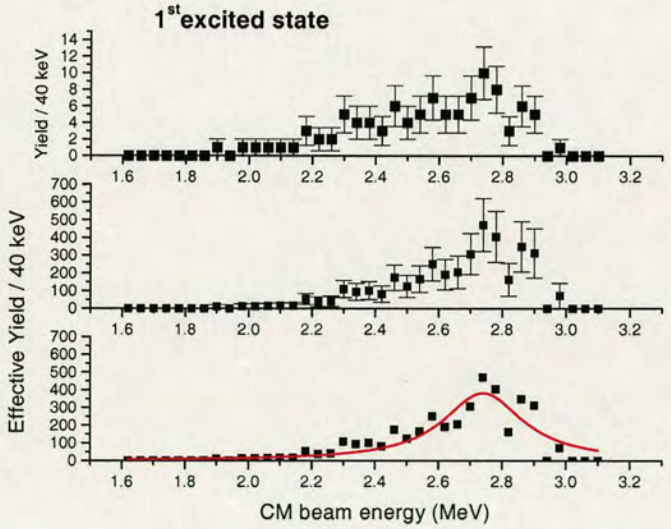

Figure 3.14: *Beam energy spectra for proton events where ground state and 1st excited state assignments can be made in* ^{21}Na .

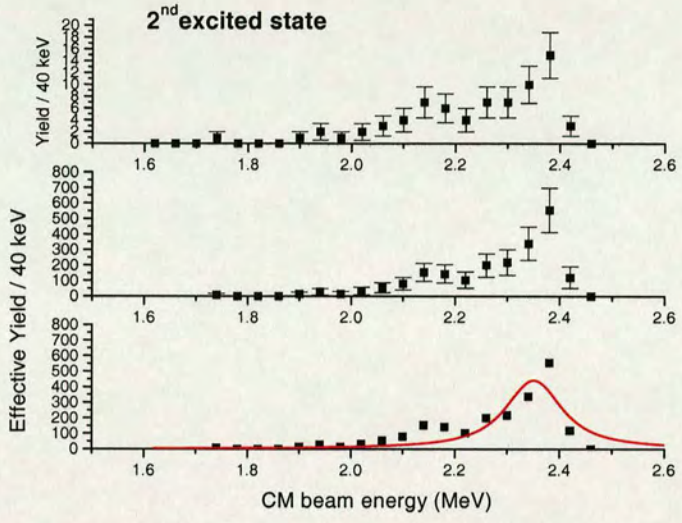

Figure 3.15: *Beam energy spectra for proton events where 2nd and 3rd excited state assignments can be made in* ^{21}Na .

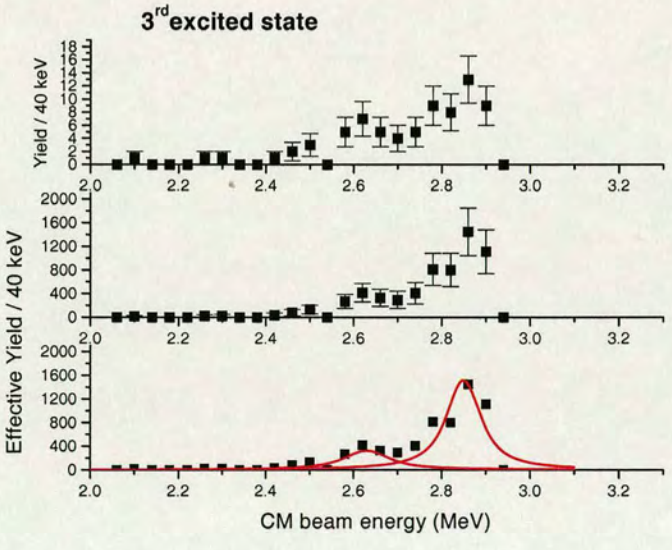

Figure 3.16: *Beam energy spectra for proton events where 2nd and 3rd excited state assignments can be made in* ^{21}Na .

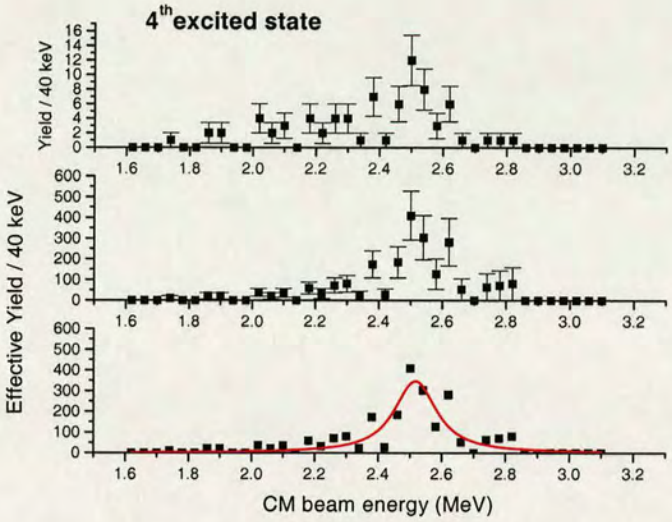

Figure 3.17: *Beam energy spectra for proton events where 4^{th} and 5^{th} excited state assignments can be made in* ^{21}Na .

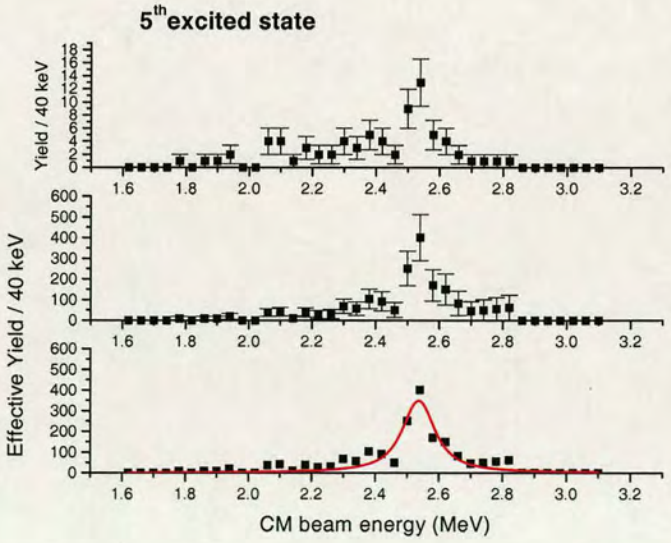

Figure 3.18: *Beam energy spectra for proton events where 4^{th} and 5^{th} excited state assignments can be made in* ^{21}Na .

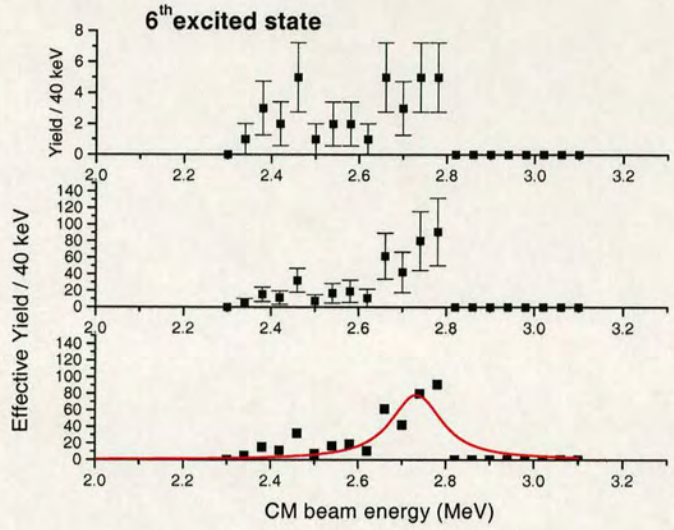

Figure 3.19: *Beam energy spectra for proton events where 6^{th} and 7^{th} excited state assignments can be made in* ^{21}Na .

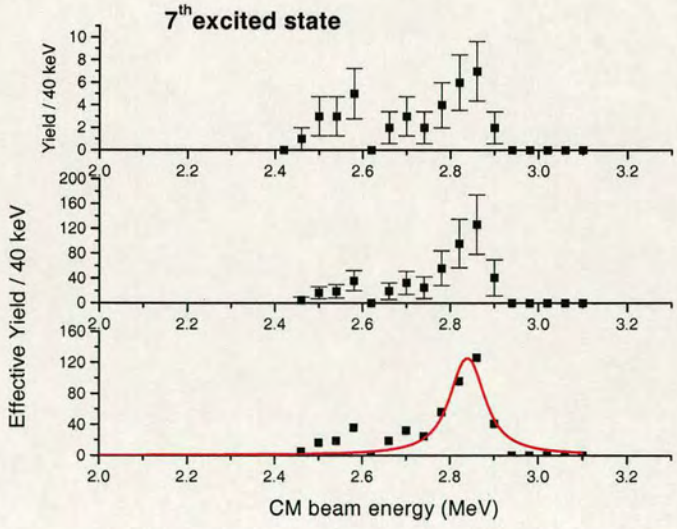

Figure 3.20: *Beam energy spectra for proton events where 6^{th} and 7^{th} excited state assignments can be made in* ^{21}Na .

3.2.4 Proton Background

It can be seen in the beam energy spectra (figures 3.9 to 3.20) that yields are observed from low energy regions of interest. The tunnelling probability for ^{18}Ne+α falls rapidly with decreasing CM energy. For instance, the tunnelling probability at a CM beam energy of 1.9 MeV is ~6% of the tunnelling probability at 2.4 MeV (assuming an ℓ=0 transition). In order to say whether these events are real it is thus necessary to look at the proton background.

The proton background was measured by running without any He gas in the chamber. However, data was taken for only one fifth of the time taken with He gas in the chamber. These events were put through the same analysis procedure and CM beam energies were reconstructed, as shown in table 3.4. Only 12 protons were observed from the background runs. The total number of protons detected experimentally was 983. This means that 1 in 17 protons are likely to be as a result of background (in the whole data set). Thus for those events populating low energy regions of interest, the worst case scenario is that 1 in 17 of them are from background. Hence from this argument most of the 983 events can be considered to be real.

Furthermore, due to there being very little background and the relatively short duration of the background run, the beam energy spectra were not corrected for background.

3^{rd}	4^{th}	5^{th}	6^{th}	7^{th}
			2.51	
			2.33	2.44
			2.38	2.48
			2.34	2.44
2.33				
	1.83	1.85	2.40	
		1.82	2.36	
			2.33	2.44
2.49				
2.28	2.55	2.58		
	2.15	2.17		
	1.80	1.82	2.38	

Table 3.4: *Reconstructed CM energies (in MeV) for the background protons for possible* ^{21}Na state assignments.

3.2.5 Sources of Error

Errors on the resonance energies (and hence ^{22}Mg excitation energies) result from: (i) the angular straggling of protons through the gas and detectors; (ii) the error in the energy loss corrected proton energy and finite pixel size and (iii) the error in the resonance energy resulting from the Lorentzian fitting.

A SRIM2000 calculation was performed to determine the contribution from (i). This determined that proton angular straggling was $\sim$1.1° corresponding to an error in the CM energy of $\pm$0.12 MeV. The error from (ii) was determined by putting limiting values on the energy loss corrected proton energy (E_{p}) and angle (θ) in the reconstruction of the CM beam energy. Upper and lower error limits on the reconstructed CM beam energy, for protons populating the ground state and the first 7 excited states in ^{21}Na, are shown in table 3.5.

E_x (^{21}Na) (MeV)	Error limits (keV)
0	± 80
0.332	± 80
1.716	± 70
2.425	$^{+80}_{-70}$
2.798	± 70
2.829	± 70
3.544	$^{+70}_{-60}$
3.680	$^{+70}_{-60}$

Table 3.5: *Errors in the reconstructed CM beam energy.*

The dominant source of error is that from angular straggling of the protons. It is not clear how the three separate contributions are related in determining the final error in the CM beam energy. It is likely to be a complicated procedure, involving a convolution of an unknown function. Thus the three sources of error were summed in quadrature, to give the total error, which can be considered to be a reasonable estimate.

3.2.6 Comparison with known data

Definite information can be deduced on the energy levels in ^{22}Mg where there is no ambiguity and a unique level assignment in ^{21}Na can be made. It can clearly be seen that particular levels in ^{21}Na can be populated through more than one level in ^{22}Mg. However, for those cases where there is some ambiguity and more than one level assignment is possible, no definite information on the level structure of ^{22}Mg can be deduced.

Calculation of the angular distribution of protons showed that the ground state, 1^{st}, 6^{th} and 7^{th} excited states have the same spin coupling possibilities, the 2^{nd} and 5^{th} excited states have the same spin coupling possibilities and

the 3^{rd} and 4^{th} excited states have the same spin coupling possibilities. This information can be used, together with resonance energy information from cases where a unique level assignment can be made, to place a restriction on the possible state assignments in ^{21}Na. For those cases where 2 state assignments are possible, it is thus assumed that the states accessed are the ground state, 3^{rd}, 5^{th} and 6^{th} excited states.

The low statistics and limited angular range of the detectors prevent the angular momentum of the outgoing protons from the proton angular distribution to be determined reliably. The spins of the states accessed in ^{22}Mg can otherwise be determined as detailed in appendix C. An ℓ=0 transition has been assumed for all the protons.

It should be pointed out that those states in ^{22}Mg which populate the 2^{nd} excited state in ^{21}Na (spin $7/2^+$) have possible spins of 4^+ for an ℓ=0 transition and 3^- or 5^- for an ℓ=1 transition. In the ^{18}Ne+α channel, the effective barrier for alphas with ℓ=4 is 10.72 MeV, the effective barrier for alphas with ℓ=2 is 7.21 MeV and the Coulomb barrier (ℓ=0) is 5.71 MeV. The transmission probability for alphas penetrating the effective barrier will be very low compared to that for penetrating the Coulomb barrier. For instance, the ratio between the transmission probabilities for alphas with ℓ=2 compared to ℓ=0 is $\sim 10^{-3}$ and that for alphas with ℓ=4 compared to ℓ=0 is $\sim 10^{-5}$. These probabilities were calculated from an optical model code (supplied by B. Fulton).

A more rigorous treatment involved determining the angular momentum of the alpha particle and that of the proton assuming the lowest possible state spin (and hence maximum probability) and calculating the product of the transmission probabilities for the entrance and exit channels. This gives an

indication of the likely spin of such states. One must note, however, that this method does not take into account the alpha and proton spectroscopic factors and relies on the barrier penetration factors alone. The results from this are shown in table 3.6.

J^π	ℓ_α	ℓ_p	T_{in}	T_{out}	$T_{in}.T_{out}$
0^+	0	4	$3.93E^{-5}$	$2.34E^{-4}$	$9.20E^{-9}$
1^-	1	3	$2.44E^{-5}$	$6.02E^{-4}$	$1.47E^{-8}$
2^+	2	2	$1.01E^{-5}$	$1.07E^{-3}$	$1.08E^{-8}$
3^-	3	1	$3.00E^{-6}$	$1.18E^{-3}$	$3.54E^{-9}$
4^+	4	0	-	$1.02E^{-3}$	-

Table 3.6: *Transmission coefficients for the entrance and exit channels.*

It can be seen in table 3.6 that it is thus more likely that states in ^{22}Mg which decay to the 2^{nd} excited state in ^{21}Na will have a spin of 2^+. However, for this to be the case, the emitted protons must have an angular momentum, ℓ=2 when coupled with the channel spin to give a 2^+ state. It was concluded from the CM proton energy spectrum (see appendix C for details), however, that protons are more likely to have an angular momentum, ℓ of 0 or 1. As a result of this, the contributions to the angular distribution for protons accessing the 2^{nd} excited state in ^{21}Na with ℓ=2 were not taken into account. Table 3.7 presents a comparison between the results obtained in the present study and previous results from studies of the ^{16}O(^{12}C,^{6}He)^{22}Mg reaction and the previous direct measurement of the ^{18}Ne(α,p)^{21}Na reaction. Likely spins assuming an ℓ=1 transition are shown in brackets. It can be seen that the excitation energies obtained from this work are in good agreement with previous studies. A corresponding level diagram is shown in figure 3.21.

Table 3.7: *Excitation energies in* ^{22}Mg with $E_x \geq 10.00$ MeV.

^{16}O(^{12}C,^{6}He)^{22}Mg[1]	^{18}Ne(α,p)^{21}Na[2]	^{18}Ne(α,p)^{21}Na[3]	J^π
10.078±0.024		10.12±0.14	2^+ (3^-)
10.190±0.029			
10.297±0.025		10.31±0.14	2^+ (3^-)
10.429±0.026		10.42±0.15	2^+ (1^-)
10.570±0.025	(10.580±0.050)	10.55±0.14	2^+ (3^-)
10.660±0.028		10.66±0.14	2^+ (1^-)
10.750±0.031		(10.77±0.14)	0^+ (1^-)
10.844±0.038	(10.820±0.060)	10.87±0.14	0^+ (1^-)
	10.910±0.050	10.92±0.14	2^+ (1^-)
10.980±0.031	10.990±0.050	(10.99±0.14)	0^+ (1^-)
	(11.050±0.050)	11.01±0.14	2^+ (1^-)
11.135±0.040	11.130±0.050		

[1]Chen *et al* [23]. [2]Bradfield-Smith *et al* [21, 22]. [3]The present work. Levels in parenthesis are tentatively assigned.

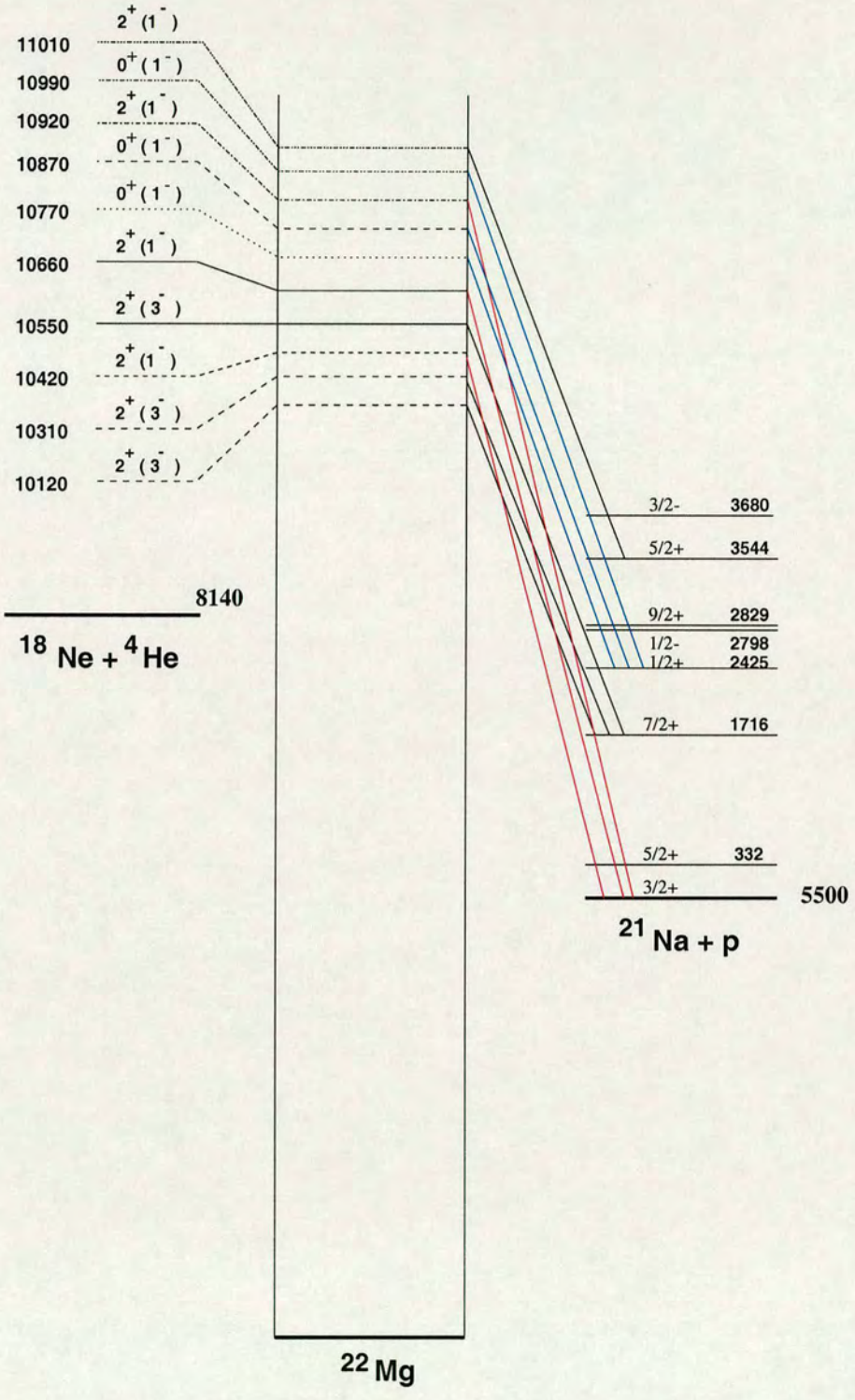

Figure 3.21: *Level diagram showing the states accessed in* ^{22}Mg.

Chapter 4

Theoretical Interpretation

4.1 Calculation of the Resonance Strength

Consider a thin element of gas at a distance, x from the entrance window. This distance corresponds to an energy, $E(x)$ and thus has a thickness, δE (see figure 4.1).

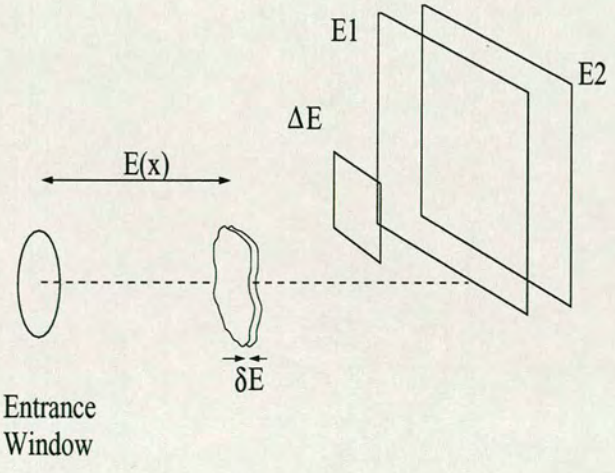

Figure 4.1: *A schematic to illustrate the $\omega\gamma$ calculation.*

The beam energy distribution at this point is Gaussian, as measured by the

direct beam profile measurement. This is probably as a result of straggling and is taken into account in the calculation of detection efficiency.

The yield of protons in the detector system, due to reactions within this gas element is:

$$Y = N_t N_B \int_{E_r-\Gamma}^{E_r+\Gamma} \sigma(E)\,\epsilon(E)\,dE \tag{4.1}$$

where N_B is the integrated beam current, $\epsilon(E)$ is the efficiency of the detectors (see section 3.2.2 and appendix B) and $\sigma(E)$ is the laboratory reaction cross section. N_t is the element target thickness and is determined from knowing both the energy loss in the target and the gas pressure.

For a resonance the resonance strength, $\omega\gamma$ is given by:

$$\omega\gamma = \omega\,\frac{\Gamma_p\Gamma_\alpha}{\Gamma} \tag{4.2}$$

Using the equations for $\sigma(E)$, as defined in equation 1.14, and $\omega\gamma$ above we get:

$$Y = \frac{\pi\, N_t\, N_B\, \Gamma\, \hbar^2}{2\mu}\,\omega\gamma \int_{E_r-\Gamma}^{E_r+\Gamma} \frac{\epsilon(E)}{E\left[(E-E_r)^2 + (\frac{\Gamma}{2})^2\right]}\,dE \tag{4.3}$$

where Y is the experimental yield of protons from the resonance. Thus $\omega\gamma$ can be calculated from:

$$\omega\gamma = \frac{2\mu Y}{\pi\, N_t\, N_B\, \Gamma\, \hbar^2}\left[\int_{E_r-\Gamma}^{E_r+\Gamma} \frac{\epsilon(E)}{E\left[(E-E_r)^2 + (\frac{\Gamma}{2})^2\right]}\,dE\right]^{-1} \tag{4.4}$$

Thus $\omega\gamma$ depends on knowledge of the resonance parameters, E_r and Γ and an understanding of the efficiency in the CM system. The integral can be evaluated numerically using Simpson's rule of integration [43], the results of which are shown in table 4.1. It should be pointed out that in reality these

widths are likely to be too wide to be real but, to a first order, this will not affect the integral. Errors in $\omega\gamma$ arise due to uncertainties in the yield and in the resonance parameters, E_r and Γ. These errors are calculated using limiting values on these parameters. It can be seen that the strongest resonances are those which populate the 2.425 MeV state in ^{21}Na.

Γ (MeV)	E_r (MeV)	E_x (^{22}Mg) (MeV)	$\omega\gamma$ (keV)
0.10±0.02	1.98±0.14	10.12±0.14	$1.6\ ^{+0.3}_{-0.2}$
0.15±0.09	2.17±0.14	10.31±0.14	$10.2\ ^{+7.5}_{-1.2}$
0.21±0.10	2.28±0.15	10.42±0.15	$7.3\ ^{+9.7}_{-1.5}$
0.16±0.03	2.41±0.14	10.55±0.14	$22.4\ ^{+4.5}_{-3.2}$
0.10±0.05	2.52±0.14	10.66±0.14	$18.2\ ^{+8.9}_{-1.9}$
0.12±0.09	2.63±0.14	10.77±0.14	$73.8\ ^{+19.6}_{-11.4}$
0.21±0.02	2.73±0.14	10.87±0.14	$80.4\ ^{+30.1}_{-21.5}$
0.12±0.02	2.78±0.14	10.92±0.14	$34.0\ ^{+4.9}_{-3.6}$
0.08±0.02	2.85±0.14	10.99±0.14	$92.4\ ^{+19.0}_{-11.0}$
0.10±0.02	2.87±0.14	11.01±0.14	$8.1\ ^{+2.9}_{-2.0}$

Table 4.1: *A summary of the resonance parameters for the transitions considered.*

4.2 Calculation of the Stellar Reaction Rate

The stellar reaction rate, $< \sigma v >$ can be calculated using equation 1.17. If $\Gamma \ll kT$ the resonance can be assumed to be narrow. In this instance $E\,e^{-\frac{E}{kT}}$ varies slowly over the width of the resonance. However, for the ^{18}Ne(α,p)^{21}Na reaction, typical widths are $>kT$ and therefore resonances can not be considered as being narrow.

Using the Breit-Wigner form to describe the resonance is an approximation and is only valid over the energy range covered by the data. Hence the limits of the integration should cover the range over which the fitting is valid. The

stellar reaction rate per particle pair thus becomes:

$$< \sigma v >= \left(\frac{2}{\mu\pi}\right)^{\frac{1}{2}} \left(\frac{1}{kT}\right)^{\frac{3}{2}} \left(\frac{\hbar^2\pi}{\mu}\right) (\omega\gamma)\, \Gamma \int_{E_r-\Gamma}^{E_r+\Gamma} \frac{e^{-\frac{E}{kT}}}{(E-E_r)^2 + (\frac{\Gamma}{2})^2}\, dE \quad (4.5)$$

where the symbols have the meaning defined previously. The integral can be evaluated numerically using Simpson's rule of integration. Errors arise due to uncertainties in the resonance parameters and the resonance strength and are calculated using limiting values on these parameters. Figure 4.2 shows the variation in $< \sigma v >$ as a function of temperature, calculated for each resonance. It can be seen that the stellar reaction rate is dominated by the 10.77 and 10.87 MeV resonances above a temperature of 1.5 GK and by the 10.12 and 10.31 MeV resonances below 1.5 GK.

The total stellar reaction rate is given by:

$$< \sigma v >_T = \left(\frac{2}{\mu\pi}\right)^{\frac{1}{2}} \left(\frac{1}{kT}\right)^{\frac{3}{2}} \left(\frac{\hbar^2\pi}{\mu}\right) \sum_i \int_{E_r-\Gamma}^{E_r+\Gamma} \frac{\Gamma_i\, (\omega\gamma)_i\, e^{-\frac{E}{kT}}}{(E-E_{r_i})^2 + (\frac{\Gamma_i}{2})^2}\, dE \quad (4.6)$$

where i is a sum over all transitions. Figure 4.3 shows the variation in the total stellar reaction rate as a function of temperature. The experimental rate is shown compared with theoretical predictions [44] based on the level structure of ^{22}Mg and on Hauser-Feshbach statistical calculations with the code SMOKER. Also shown for comparison is the reaction rate from the previous direct measurement [21, 22]. Upper and lower limits are calculated from limiting values of the resonance parameters and resonance strengths. It can be seen that the discovery of lower lying states in ^{22}Mg has acted to enhance the stellar reaction rate as compared to the previous measurement. This enhanced rate is in reasonable agreement with theoretical predictions

at and above a temperature of 1.5 GK. However, the stellar reaction rate rapidly falls below predicted values at lower temperatures. This is because the theoretical calculations used predicted resonance strengths at lower CM energies between 0.15 and 2.00 MeV, whereas the experimental rate uses only the observed resonances between 1.98 and 2.87 MeV. Lower energy states will dominate the reaction rate at lower temperatures.

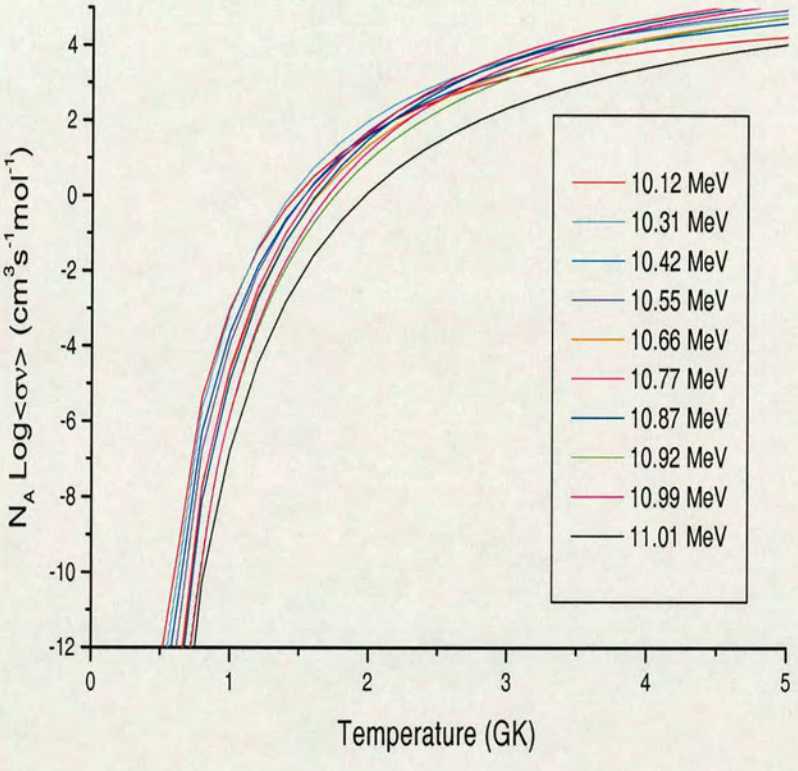

Figure 4.2: *The stellar reaction rate as a function of temperature for each resonance. The errors are not shown in this figure.*

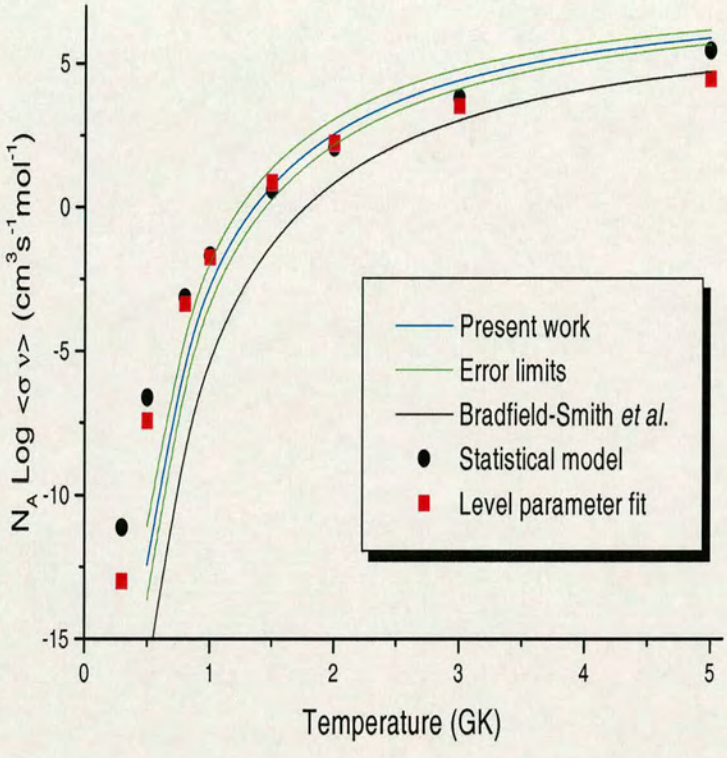

Figure 4.3: *The total stellar reaction rate as a function of temperature compared with theoretical predictions and the previous direct measurement.*

4.3 Astrophysical Implications

The experimentally determined stellar reaction rate can be used in a full network calculation for the rp and α processes. The impact of which upon the nucleosynthesis that takes place during an X-ray burst has been investigated previously by W. Bradfield-Smith [21]. This calculation was based on a 1-zone X-ray burst model (developed at Notre Dame), where an X-ray burst is modelled in 1-D with a constant accretion rate from the companion star. In addition, this model assumed that the envelope expansion is adiabatic and that the ejected material falls back to the surface of the neutron star.

Figure 4.4 shows the energy generation, temperature and density of an X-ray burst from the previous calculation [21]. It can be seen that the burst can be characterised by four phases. The reader is referred to the aforementioned reference for full details of the results from this calculation. Only the significance of the ^{18}Ne(α,p)^{21}Na reaction will be discussed here. The peak phase (denoted by 2 in figure 4.4) is dominated by the triple alpha and breakout reactions. ^{18}Ne is processed through the second hot-CNO cycle and breakout via the ^{18}Ne(α,p)^{21}Na reaction gives rise to an increase in energy production. This is illustrated in figure 4.5 by the peak 2b.

The observation of lower lying resonances in ^{22}Mg from this work has acted to increase the total stellar reaction rate. For instance, at a temperature of 2.0 GK (typical in an X-ray burst) the stellar reaction rate is enhanced by a factor of $\sim$50 compared to that obtained in the previous direct measurement. This means that breakout via this reaction proceeds much more rapidly than was previously thought. The destruction of ^{18}Ne (and the subsequent pro-

cessing of ^{21}Na) thus occurs more quickly and the peak in energy production will occur faster and within a smaller time interval. More detailed physics will emerge when this enhanced stellar reaction rate is included in more sophisticated models that take into account stellar rotation, magnetic fields and gas hydrodynamics.

The enhanced stellar reaction rate obtained in this work could also be included in a network calculation of the nucleosynthesis that is thought to take place in novae. One will then be able to say whether (α,p) breakout also occurs during novae. Due to time constraints, these are now matters for the future.

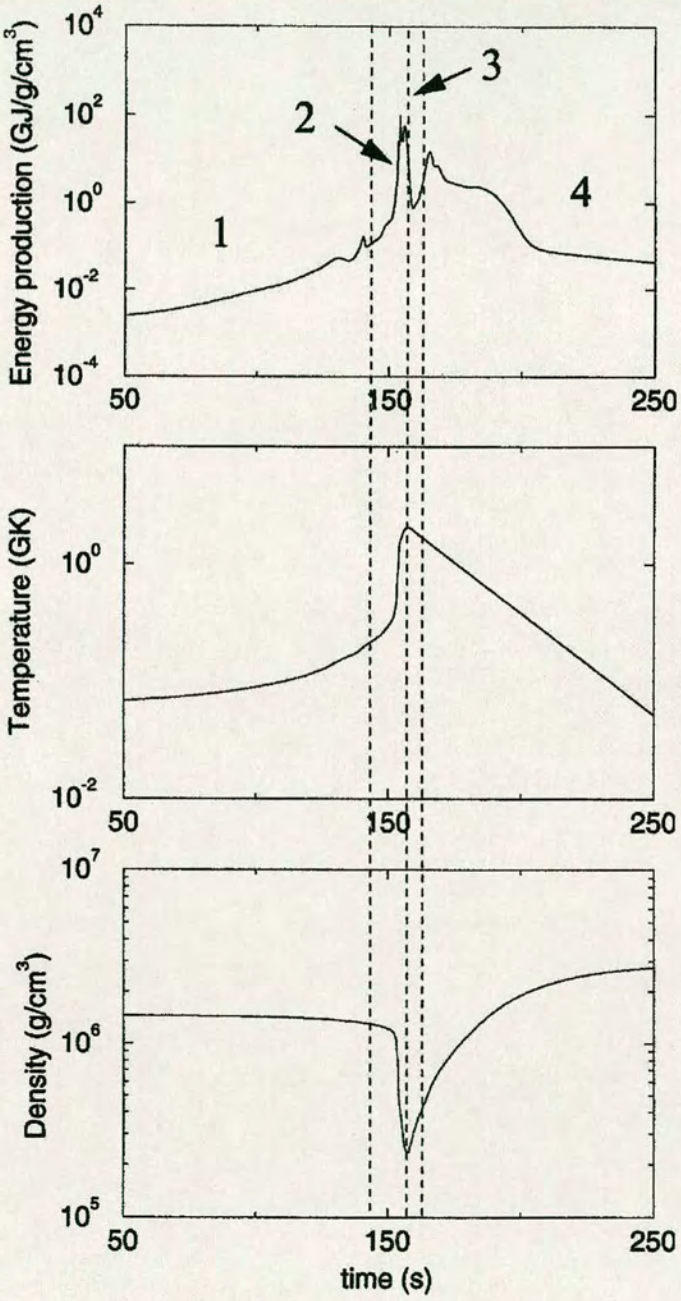

Figure 4.4: *Energy generation, temperature and density of an X-ray burst [21].*

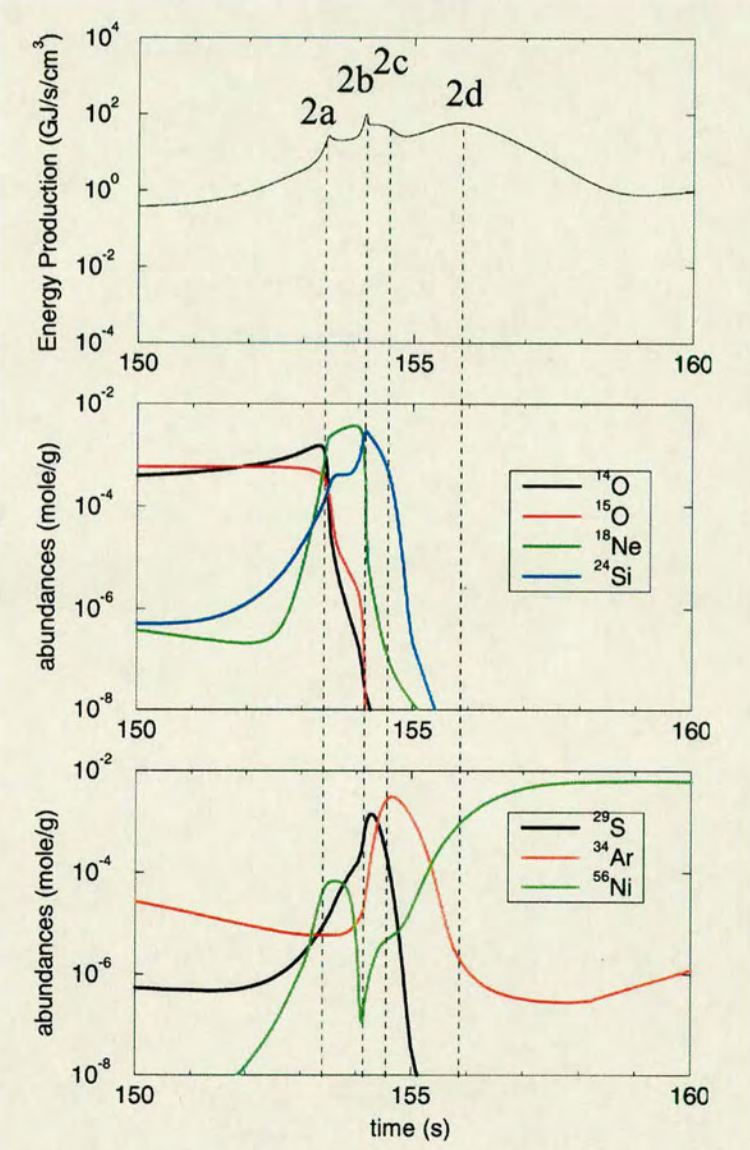

Figure 4.5: *Phase 2 of the energy generation of an X-ray burst. Also shown are the abundances for the nuclei of interest [21].*

Chapter 5

Conclusions

The experimental technique previously developed for the investigation of (α,p) reactions has been optimised. A change in the detector geometry from that adopted in a previous experiment had the effect of increasing the detection efficiency and significantly reduced the proton background.

The nucleus, ^{22}Mg has been studied successfully at lower energy between an energy region of $\sim$10$-$11 MeV. Ten states have been identified within this region and have been given spin assignments. These states have been compared with information that is currently known from an indirect method and are in good agreement. The existence of those states found in the previous direct measurement have also been verified.

Resonance strengths, $\omega\gamma$'s were calculated from a knowledge of the resonance parameters and the detection efficiency function, using the observed proton yield for each resonance. Taking a direct measurement of the energy profile of the ^{18}Ne beam drastically reduced the major source of uncertainty on these resonance strengths. The calculated $\omega\gamma$'s have been used to evaluate the stellar reaction rate in the temperature region between 0-5 GK. This

stellar reaction rate shows reasonable agreement with theoretical predictions [44] at and above a temperature of 1.5 GK. At lower temperatures, however, the stellar reaction rate rapidly falls below theoretical predictions. This is due to the fact that the theoretical calculations used predicted resonance strengths at lower CM energies between 0.15 and 2.00 MeV. The agreement above 1.5 GK shows that the observed resonances dominate the reaction rate at these temperatures.

The limit of this experimental technique is such that resonances and resonance strengths can be measured down to 1.7 MeV. Indeed, small yields were observed at such energies, however, no reliable fits could be made because of the low statistics. Further work will need to be done in order to check the theoretical calculations below 1.5 GK. To do so using this technique, a more intense ^{18}Ne beam and longer run time will be required to increase the yields from lower lying resonances.

A previous 1-zone network calculation [21] showed that the ^{18}Ne(α,p)^{21}Na reaction rate is sufficient to trigger an X-ray burst. The observation of lower lying resonances in ^{22}Mg in this work has acted to increase the total stellar reaction rate. Future work will be to include this enhanced rate into existing X-ray burst models. More detailed physics will emerge from more sophisticated models that take into account stellar rotation, magnetic fields and gas hydrodynamics. In addition, including this enhanced rate into a nova model will shed light on whether (α,p) breakout also occurs during novae.

Furthermore, the optimisation of this technique has shown its validity in the investigation of (α,p) reactions. Along with the improvements suggested in the next chapter, this technique can be used successfully to investigate other (α,p) reactions of astrophysical interest.

Chapter 6

Future Work

6.1 The ^{18}Ne(α,p)^{21}Na Reaction

The initial aim of this experiment was to improve upon the previous measurement of the ^{18}Ne(α,p)^{21}Na reaction. Changing the detector geometry gave a higher detection efficiency and eliminated the proton background from the window. In addition, the use of two detector telescopes at either side of the beam line doubled the statistics. Furthermore, taking a direct measurement of the energy profile of ^{18}Ne, as it passes through He gas, has greatly reduced the uncertainty in the resonance strengths. From this point of view, this experiment has been successful. However, there are additional improvements that can be made.

Reducing the beam spot size would reduce the range of the upper and lower limits given by the tracking. This would then restrict the possible CM beam energies further. One must note that this is a problem with the accelerator and not the experimental setup itself.

6.1.1 Energy Profile of the ^{18}Ne beam

The most important improvement would be to the direct beam profile measurement. This affects the range of the upper and lower limits from the tracking and also the efficiency calculation. Obvious improvements would be to take more measurements and cover a wider energy range to give a more complete description of the energy profile.

Measurement of the dead layer thickness of the surface barrier detector would give a more accurate determination of the dead layer contribution to the pulse height defect. The simplest technique would be to vary the angle of incidence of, for example, a collimated source of α particles (e.g. ^{241}Am). In this way the detector could be rotated over a range of angles. The difference between the measured pulse heights for angles of incidence of $0°$ and θ, coupled with energy loss information, can be used to determine the thickness of the dead layer.

Calibration of the detector with an α source is another source of error. An alternative method would be to use a time-of-flight technique which would allow a direct energy calibration. This technique requires the use of two detectors a known distance apart. One detector (which would need to be very thin to minimise energy loss) provides the start time signal and the other provides the stop time signal. The velocity (and hence energy) of the beam can be calculated from the time taken to traverse this fixed distance. A measurement would need to be taken with and without the Ni window, to give the energy upon entrance into the gas and the initial energy of the beam respectively. For a timing resolution of 1ns, the error in the beam entrance energy will be $\sim$1%. This technique could only be used to measure the en-

ergy profile of the beam if a good vacuum can be obtained. In addition, the pulse height spectra would yield direct information on the energy straggling of ^{18}Ne through He gas, avoiding the need to assume Bohr straggling in the efficiency calculation.

6.1.2 Proton Background

Elastic proton background will still be present from H_2O molecules in the gas. Water is a very simple molecule and it absorbs infrared (IR) and visible radiation. This principle is used by meteorologists to measure the atmospheric water vapour content above the Earth's surface. One technique to measure water vapour content in gases, commonly employed in chemistry, is that of IR spectroscopy. The region of the infrared spectrum of interest corresponds to $\sim$4000-500 cm^{-1} ($\sim$2.5-15μm). Absorption of radiation in this region by interatomic bonds in organic molecules, result in the excitation of vibrational, rotational and bending modes, while the molecule itself remains in its electronic ground state. Chemical bonds will absorb radiation at different frequencies and intensities. An infrared spectrum is used to display this information. The frequencies at which IR radiation is absorbed can be related to bonds within the particular molecule. The reader is referred to [45] for further details on IR spectroscopy.

Portable IR spectroscopy kits are commercially available at low cost with PC compatibility. One such kit could be connected to the He gas filled chamber, via a suitable vacuum tight feedthrough. Once calibrated an on-line measurement of water vapour content in the He gas can be obtained, with a sensitivity of $\sim$1 in 10^6 ppm.

Despite using ultra-pure He gas, any H contamination in the gas itself could also contribute to the elastic background. It is, however, extremely difficult to remove H from gases [46].

6.2 Other (α,p) Reactions of Interest

There are other (α,p) reactions that could be measured using this technique. For instance the $^{14}O(\alpha,p)^{17}F$ reaction is important in determining the rate of formation of ^{18}Ne (via a proton capture reaction on ^{17}F). Acceleration of an ^{14}O beam poses an experimental challenge, however, due to the chemical reactivity of oxygen. This reaction is planned to be measured at the TRIUMF facility at a later stage.

Another (α,p) reaction leading to the hot Ne-Na cycle is the $^{18}F(\alpha,p)^{21}Ne$ reaction. The rate of formation of ^{18}F is determined by the rate of formation of ^{18}Ne. This experiment is currently being planned at Louvain-la-Neuve [47]. Furthermore, the $^{23}Na(\alpha,p)^{26}Mg$ reaction leads to the hot Mg-Al cycle. This reaction has been studied indirectly [48], however, no direct measurement has yet been made.

There are also other key waiting points, along the path of the *rp process*, that may be important in determining the rate of flow of material to higher mass. These include the $^{34}Ar(\alpha,p)^{37}K$ and $^{44}Ti(\alpha,p)^{47}V$ reactions. The latter of which has been previously measured at ATLAS/ANL.

It is clear that the major limiting factors in using this technique to measure (α,p) reactions is the availability of the required beams and crucially, the expected intensities of such beams.

Appendix A

A.1 The Energy Loss of Ions in Matter

Incident charged particles lose energy through interactions with target atoms. This can be described by two mechanisms: the first, *electronic stopping*, is dominant at velocities greater than the Bohr velocity ($\sim$ 2200km/s [49]). At such velocities, the bound valence electrons do not have enough time to change their position relative to the incident particle and the incident particle loses energy through inelastic collisions with atomic electrons. When an ion strikes an electron, the energy transferred to the electron is given by:

$$\sim \frac{4m_{\mathrm{e}}}{m} \cos^2(\theta)\, E \tag{A.1}$$

where E is the incident energy of the ion and θ is the recoil angle.
Thus, for an incident ion to lose all of its energy, it must undergo many thousands of collisions with atomic electrons. The energy gained in such a collision can excite the electron to a higher bound level, or if high enough, can ionise the atom.

An incident ion travelling through a medium slows down gradually and effectively travels in a straight line (the scattering of the ion is small but the electrons may be scattered to large angles). This "slowing down" can be characterised by an average slowing down rate or *stopping power* given by the Bethe-Bloch formula [50]:

$$(-)\frac{dE}{dx} = \frac{1}{(4\pi\varepsilon_0)^2}\frac{4\pi e^4 z^2}{m_e v^2} N Z \left[\ln\frac{2m_e v^2}{I} - \ln(1-\frac{v^2}{c^2}) - \frac{v^2}{c^2}\right] \qquad \text{(A.2)}$$

where v and ze are the velocity and charge of the incident ion, N and Z are the number density and atomic number of the target, m_e is the electron rest mass, e is the electronic charge and I is the average ionisation/excitation potential of the target.

This formula, which is derived from elastic scattering by atomic electrons using quantum mechanics in the Born approximation, assumes that the electron is at rest and is therefore not valid at low velocities. At velocities comparable to the velocity of atomic electrons, the nucleus appears to be surrounded by an electron cloud. When the electron cloud from another atom approaches, it becomes distorted resulting in a decrease in the screening of the nuclear charges. When the electron clouds overlap, electrons can jump between the atoms. This "charge exchange" causes momentum transfer to the target electrons from the incident particle, thus reducing $\frac{dE}{dx}$. The effect on the target medium is to leave a track of ionisation where the electrons are knocked off the atoms. Some of these electrons acquire significant energy ($\sim$ 1keV) and produce their own tracks of ionisation. These are known as δ-electrons.

The second mechanism for which an incident charged particle can lose its

energy is through *nuclear stopping* where the projectile interacts with nuclei. However, this contribution is typically of the order of 1% that of electronic stopping.

The average distance travelled in the medium before the incident ion stops is characterised by the *range* which can be determined as follows [25]:

$$r(E) = \int_0^E \frac{1}{\frac{dE}{dx}(E)} dE \tag{A.3}$$

One is usually interested in the mean projected range. This is the average depth into the material that a particle, incident at 90°, penetrates.

In reality, however, no two ions starting with the same energy will slow down in exactly the same way. It is a stochastic process and after passing through some thickness of material, a beam of identical particles will have an energy loss distribution. The width of this distribution is the *energy loss straggling*. Similarly it will have a distribution of final ranges (longitudinal and transverse), the width of this distribution is termed *range straggling*. The range straggling for ions is typically 1% of the range [25].

A.2 The Use of SRIM2000 for Energy Loss Calculations

SRIM2000 is a set of programs which uses a full quantum mechanical treatment of projectile-target collisions to calculate the stopping and range of ions in matter (from 100eV/u to 2GeV/u). A Monte Carlo technique is employed making the calculation very efficient. These algorithms average the collision results over allowed gaps in-between each collision. The projectile and tar-

get ions/atoms have screened Coulomb collisions and electron excitations and plasmons are created in the target through long range interactions of the projectile. The effective charge concept (including a velocity-dependent charge state and long-range electron screening) is used to describe the charge state of the projectile within the target. Further information detailing the physics of the calculation can be found in reference [51].

The most comprehensive program, TRIM (the Transport of Ions in Matter) calculates special stopping powers for ions traversing through He (and other) gas targets. The stopping powers in solid and gas targets of the same element differ by <10% for projectiles above 200keV/u. TRIM assumes that gas targets are at standard temperature and pressure (0°C, 1 atm), however, this can be varied. As the stopping power of ions in gases is greatly dependent on the gas pressure, differences up to a factor of two may be found for pressures other than STP [52]. The actual simulations of ^{18}Ne ions in a He gas target at 500 mbar were performed with the option "Ion Distribution and Quick Calculation of Damage." This option calculates damage based on the Kinchin-Pease method and calculates the final distribution of ions in the target and the final trajectory and energy of those ions that are transmitted through the target.

The degree of angular straggling of ^{18}Ne ions (as a function of distance through the gas) was found to correspond to transverse distances less than the assumed radius of the beam spot. Hence the effects of this angular straggling could be ignored.

Figures A.1 and A.2 show typical output from SRIM2000 for 30.0 MeV ^{18}Ne ions going into 51.7nm Au + 2.35μm Ni + 60mm He gas at 500 mbar, recreating the actual experimental conditions.

Figure A.1: *Longitudinal view showing the trajectory of* ^{18}Ne ions as a function of depth into the target.

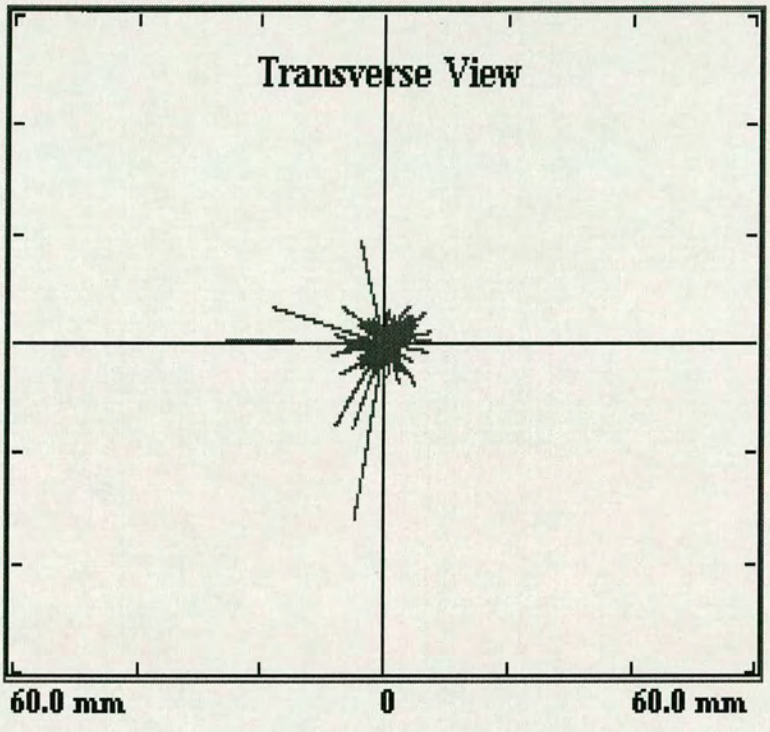

Figure A.2: *Transverse view showing the degree of angular straggling of* ^{18}Ne ions in He gas.

Appendix B

B.1 Calculation of the Efficiency Function

Protons can be produced at any position within the volume of gas. Thus, the target is not fixed in relation to the telescopes. Therefore, for the proton telescopes, the efficiency is a function of CM beam energy and the state accessed in the residual nucleus, ^{21}Na.

A Monte Carlo simulation was developed to calculate the efficiency of the proton telescopes. The gas target was split into 60 elements, each of thickness 0.1cm (corresponding to a distance along the Z-axis of 6cm from the entrance window). For each gas element, 10^5 protons were randomly created with a sinusoidal distribution in theta and a flat distribution in phi - giving an isotropic distribution in the CM frame. A random number generator was used to produce a number between 0 and 1. The angles are then calculated from:

$$\theta' = \cos^{-1}(1 - RANDOM) \tag{B.1}$$

$$\phi' = (\pi \times RANDOM) \tag{B.2}$$

For a given beam energy and Q-value, the energy (E_{p}) and velocity vector of each proton (v_{p}) can be transformed into the laboratory frame. In component form, these velocities are:-

$$v_{\mathrm{p}}(x) = v_{\mathrm{p}} \sin\theta \cos\phi \tag{B.3}$$

$$v_{\mathrm{p}}(y) = v_{\mathrm{p}} \sin\theta \sin\phi \tag{B.4}$$

$$v_{\mathrm{p}}(z) = v_{\mathrm{p}} \cos\theta \tag{B.5}$$

where $v_{\mathrm{p}} = \sqrt{(\frac{2E_{\mathrm{p}}}{m_{\mathrm{p}}})}$. This allows the position of the proton to be tracked from its origin.

The detectors are made up of pixels to give a realistic representation. An event is registered if the velocity vector, once transformed into the frame of reference of the detectors, passes through pixels for both the ΔE and E detectors.

Due to the fact that some of the pixels were inactive in the experiment, those protons that passed through inactive pixels were rejected. In addition, the "active" area of the detectors was taken into account from a knowledge of the distribution of proton events in the X and Y planes, taken from the actual experimental data.

The beam spot was given a Gaussian distribution in the X and Y planes, with a diameter of 1cm. The effect of energy loss of the beam was taken into account using the result from the direct measurement (see section 3.1.2).

The effect of energy straggling of the ^{18}Ne ions, through the Au+Ni window and the helium gas, was calculated using the Bohr derivation (program supplied by T. Davinson). This showed that the energy straggling was pro-

portional to the square root of the gas target thickness (see figure B.1) and that the straggling of the ^{18}Ne beam upon exit from the window was 348 keV. The straggling obtained from the direct measurement was 665 keV (see table 3.1). Thus the Bohr derivation underestimates the degree of energy straggling by ~50%.

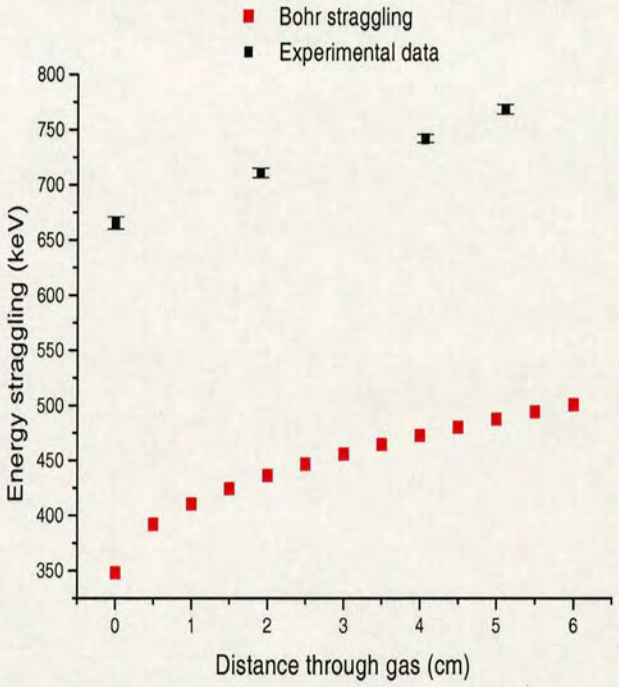

Figure B.1: *Energy straggling as a function of distance through* He gas (Bohr derivation).

The efficiency is given by the number of protons striking the detectors divided by the total number of protons initially created. The statistical errors on the efficiency are ~1-3%.

Due to inverse kinematics (a heavy projectile on a light target), the angular distribution of the outgoing protons will be forward peaked rather than isotropic. The angular distribution of proton events (in the CM frame) was

calculated, as detailed in appendix C. Calculations were performed for protons emitted from ^{22}Mg leading to the ground state and the first 7 excited states in ^{21}Na. For protons leading to the ground state and the 1^{st}, 6^{th} and 7^{th} excited states, the contribution from the 4^{th} order Legendre polynomial is <20% and was thus ignored, leaving only the contributions from the 0^{th} and 2^{nd} order polynomials. These curves can hence be described by the function:

$$f(\theta') = A_1 - A_2 \sin^2 \theta' \tag{B.6}$$

For protons leading to the 2^{nd} and 5^{th} excited states, the contribution from the 2^{nd} order polynomial is zero because the particular combinations of angular momenta for these excited states gives rise to zero Z coefficients. Hence the only contributions are from the 0^{th} and 4^{th} order polynomials. These curves can hence be described by the function:

$$f(\theta') = B_1 \cos^4 \theta' - B_2 \cos^2 \theta' + B_3 \tag{B.7}$$

Protons accessing the 3^{rd} and 4^{th} excited states in ^{21}Na were found to have an isotropic angular distribution in the CM. Figure B.2 shows angular distributions for protons leading to the ground state and the 1^{st}, 2^{nd}, 5^{th}, 6^{th} and 7^{th} excited states in ^{21}Na.

Fitting this data allowed the angular distribution to be taken into account in the efficiency calculation. The angular distribution is then described by a function, $f(\theta')$ and a correction factor (CF) can be applied to the isotropic case. For each position in the gas there is a range of angles covered by the

detectors and the correction factor is thus:

$$\frac{\int_{\theta'_1}^{\theta'_2} f(\theta')\, d\theta'}{\int_0^{\frac{\pi}{2}} f(\theta')\, d\theta'} \tag{B.8}$$

The variation in these correction factors with distance through the gas can be seen for the ground state and 2^{nd} excited state in table B.1.

Distance in gas (cm)	CF (Ground state)	CF (2^{nd} excited state)
0	2.45	1.23
2	2.28	1.16
4	1.90	1.09
6	0.99	1.29

Table B.1: *Angular distribution correction factors.*

It should be pointed out that these calculations are an approximation as one of the summations is the angular momentum of the outgoing protons. It should also be pointed out that reasonable estimates for the resonance parameters E_r and Γ, based on the raw data, were used (see table B.2).

State in ^{21}Na (MeV)	E_r (MeV)	Γ (MeV)
0.000	2.52	0.15
0.332	2.61	0.08
1.716	2.43	0.10
2.829	2.55	0.10
3.544	2.84	0.12
3.680	2.86	0.12

Table B.2: *Estimates on E_r and Γ.*

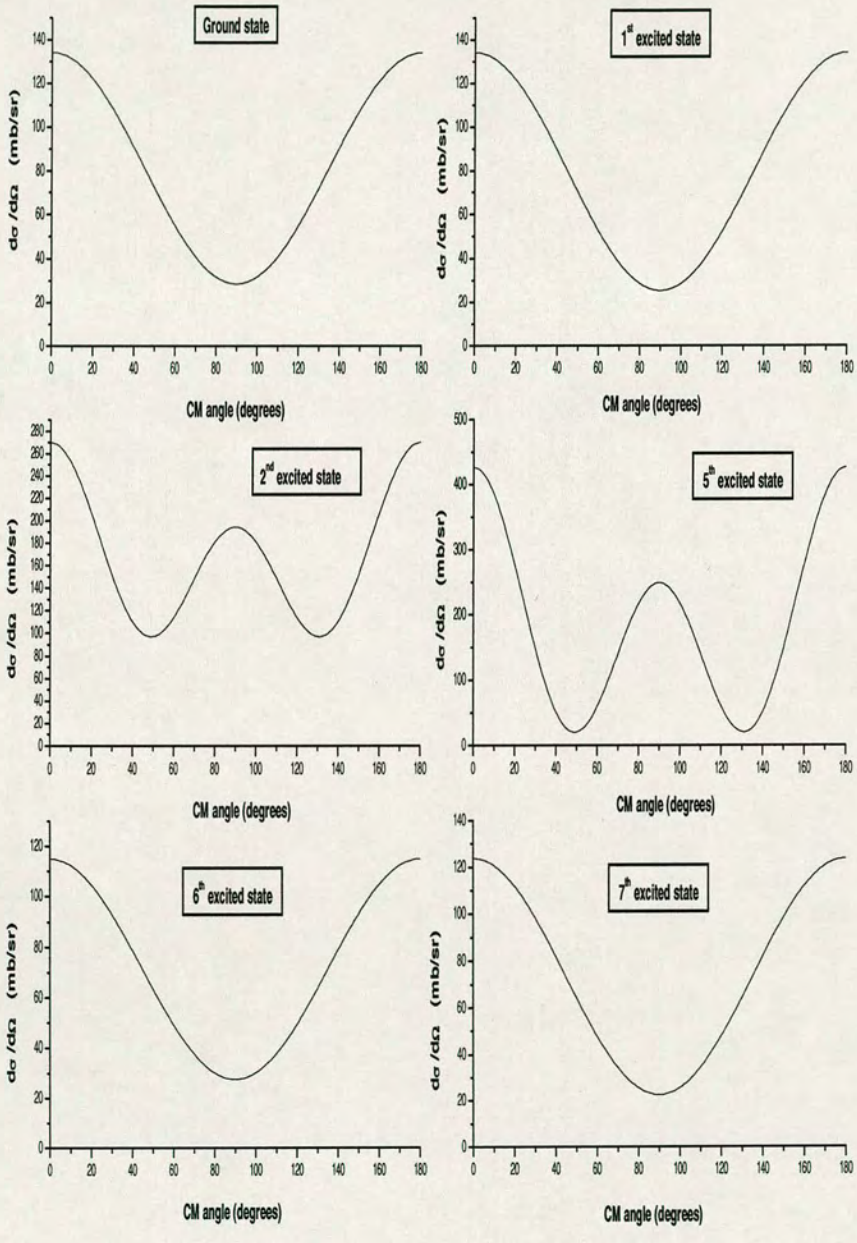

Figure B.2: *Calculated angular distributions of proton events leading to the ground state and 1st, 2nd, 5th, 6th and 7th excited states in* ^{21}Na.

Appendix C

C.1 Spin Assignments

For ^{18}Ne at 1.67 MeV/A, the ions undergo strong Coulomb repulsion and show Rutherford scattering. If they make contact with the He target nuclei they can react. There is a critical angular momentum, ℓ_c above which it is impossible for protons to be emitted since there is essentially no nuclear interaction. This can be calculated from a semi-classical treatment as follows [53]: By conservation of angular momentum:

$$p\,b = \ell\,\hbar = p'\,X \tag{C.1}$$

where p is the momentum of the incident ions, b is the impact parameter, ℓ is the outgoing orbital angular momentum, X is the closest distance between the ions and p' is their relative momentum at this distance. By conservation

of energy, we have the condition:

$$\frac{p^2}{2\,\mu} - \frac{E_{\mathrm{B}}\,R}{X} = \frac{p'^2}{2\,\mu} \tag{C.2}$$

The condition for contact of the nuclei is thus:

$$\frac{2\,\mu\,R^2(E - E_{\mathrm{B}})}{\hbar^2} \geq \ell_c^2 \tag{C.3}$$

where E_{B} is the electrostatic potential energy when the nuclei are just in contact, μ is the reduced mass, E is the energy in the CM system of ^{21}Na+p and $R = 1.2(A_1^{\frac{1}{3}} + A_2^{\frac{1}{3}})$ where A_1 and A_2 are the mass numbers of ^{21}Na and p respectively. This gives a critical angular momentum of ℓ_c=2 and hence for protons with $\mathrm{E_{CM}}$>$\mathrm{E_B}$, the possible values for the outgoing orbital angular momentum are 0, 1 and 2.

The effective potential outside the nucleus (for r > R) is given by [54]:

$$U_\ell\,(r) = \frac{Z_1\,Z_2\,e^2}{4\pi\,\varepsilon_0\,R} + \frac{\hbar^2\,\ell(\ell+1)}{2\,\mu\,R^2} \tag{C.4}$$

where the first term is the Coulomb potential and the second term is the centrifugal potential. There is a probability that a proton will penetrate this barrier. For an ℓ=0 transition, the effective barrier is 3.51MeV, which is the Coulomb barrier. For an ℓ=1 transition, the effective barrier is 5.66MeV and for an ℓ=2 transition, the effective barrier is 9.96MeV.

All proton events have a CM energy that is much lower than the effective barrier for an ℓ=2 transition (see figure C.1). Thus the transition probability for an ℓ=2 transition is lower than for an ℓ=0 or ℓ=1 transition. For those protons with a CM energy less than that of the Coulomb barrier, the

transition probability for an ℓ=0 transition is greater than that for an ℓ=1 transition. The most likely ℓ value for all protons is ℓ=0.

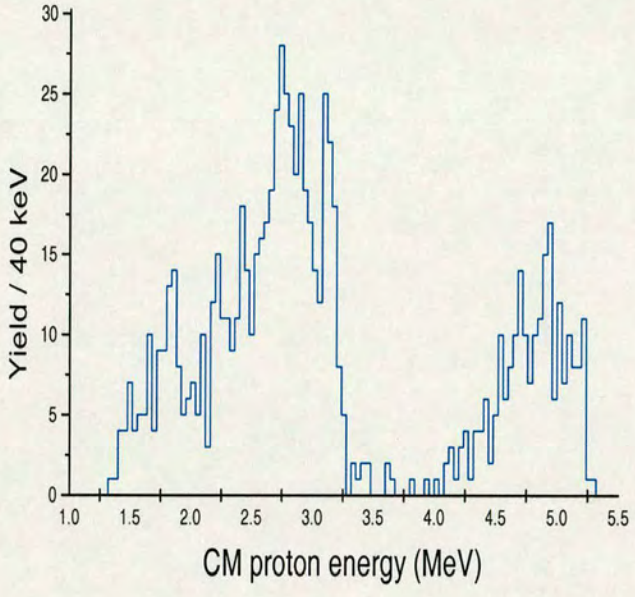

Figure C.1: *Proton CM energy spectrum.*

Both the projectile and target contain 0^+ nuclei (spin zero). This results in only natural parity states being accessed in the compound nucleus ^{22}Mg. For an ℓ=0 transition, the compound state has to be 0^+,2^+, 4^+ and so on. For an ℓ=1 transition, the compound state has to be 1^-,3^-, 5^- and so on. It is assumed that parity is always conserved in strong force reactions.

C.2 Calculation of the Angular Distribution

For a single isolated resonance in the compound nucleus of total angular momentum, J the differential cross section leading to a definite state, I in the residual nucleus is given by [55, 56, 57]:

$$\frac{d\sigma_{\alpha_1\alpha_2}}{d\Omega} = \frac{\lambda_{\alpha_1}^2}{(2i_1+1)(2I_0+1)} \frac{1}{4[(E-E_r)^2+\frac{\Gamma^2}{4}]} \sum_L \Big[P_L \cos(\theta) \sum_{s_1,s_2} \Big[(-1)^{s_1-s_2}$$

$$\Big(2^n \sum_{\ell_1} \sum_{\ell_1'} \sum_{\ell_2} \sum_{\ell_2'} i^{\ell_1-\ell_1'+\ell_2-\ell_2'} \, Z(\ell_1\, J\, \ell_1'\, J\,;\, s_1\, L)\, Z(\ell_2\, J\, \ell_2'\, J\,;\, s_2\, L)\, g_{\alpha_1 s_1 l_1}$$

$$g_{\alpha_1 s_1 l_1'}\, g_{\alpha_2 s_2 l_2}\, g_{\alpha_2 s_2 l_2'}\, \cos\left[\xi_{\alpha_1\ell_1}\, \xi_{\alpha_1\ell_1'}\, \xi_{\alpha_2\ell_2}\, \xi_{\alpha_2\ell_2'}\right] \Big) \Big] \Big] \qquad \text{(C.5)}$$

where ℓ_1 is the relative orbital angular momentum of a and X, i_1 is the intrinsic spin of a, ℓ_2 is the relative orbital angular momentum of b and Y, i_2 is the intrinsic spin of b, I_0 is the total angular momentum of the target and I is the total angular momentum of the residual nucleus. $P_L \cos\theta$ is a Legendre polynomial of order L. The primed quantities indicate interfering quantities. n is the number of pairs (ℓ,ℓ') in which the two quantum numbers are different. S_1 and s_2 are the channel spins for the incident and emitted particles respectively. From conservation of angular momentum:

$$s_1 + \ell_1 = J = s_2 + \ell_2 \qquad \text{(C.6)}$$

where $s_1 = i_1 + I_0$ and $s_2 = i_2 + I$.

Before the collision, the system can be described by α_1 which specifies the incoming particle and the state of the target nucleus, the channel spin, s_1 and the orbital angular momentum, ℓ_1. Similarly, the quantities α_2, s_2 and

ℓ_2 describe the system after the collision.

For both incident and emitted particles, the various possible orbital angular momenta must differ by integral multiples of 2. This follows from conservation of parity. The wavelength of the incoming particle, λ_{α_1} is given by:

$$\frac{\lambda}{2\pi} = \frac{M_a + M_X}{M_X} \frac{\hbar}{\sqrt{2M_a E_L}} \tag{C.7}$$

where E_{L} is the laboratory energy of the incident particle, M_{a} is the mass of the incident particle and M_{X} is the mass of the target nucleus. The quantity $g_{\alpha s \ell}$ is related to the partial width as $g_{\alpha s \ell} = \pm \sqrt{\Gamma_{\alpha s \ell}}$, where the sign ambiguity indicates that there is a nuclear phase shift which can only be 0 or 180°. Additionally, there are phase shifts for potential scattering, $\xi_{\alpha \ell}$ given by:

$$\xi_{\alpha \ell} = \sum_{m=1}^{\ell} \left(\arctan \frac{\eta_\alpha}{m} - \arctan \frac{F_{\alpha \ell}}{G_{\alpha \ell}} \right) \tag{C.8}$$

where η_α is the Sommerfeld parameter, $F_{\alpha \ell}$ and $G_{\alpha \ell}$ are the regular and irregular solutions of the radial wave equation outside the nuclear surface (as defined in [58]). The Z coefficients describe coupling of angular momenta and are defined in the next section. The summation over polynomial order, L has the following conditions: L = even, $L \leq 2J$ or $L \leq 2\, l_c'$.

C.3 Coupling of Angular Momenta

The composition of angular momenta is accomplished through Clebsch-Gordan coefficients which provide a solution to coupled angular momenta problems [59]. However, the problem is made much more complicated when transforming between coupling schemes. The properties of these transforma-

tions have been discussed in [60]. The coefficient $W(a\,b\,c\,d;\,e\,f)$ is defined as the transformation between the coupling schemes $(a+b=e;\,e+d=c)$ and $(b+d=f;\,a+f=c)$. Algebraic tables of these Racah coefficients can be found in [61].

The coefficient $Z(a\,b\,c\,d;\,e\,f)$ is more appropriate for angular distributions and is defined as follows:

$$Z = i^{f-a+c}\,[(2a+1)(2b+1)(2c+1)(2d+1)]^{\frac{1}{2}}\,W(a\,b\,c\,d;\,e\,f)\,(a\,c\,0\,0|a\,c\,f\,0) \tag{C.9}$$

where:

$$(a\,c\,0\,0|a\,c\,f\,0) = (-1)^{g+f}\,(2f+1)^{\frac{1}{2}}\,\Delta(a\,c\,f)\,\frac{g!}{(g-a)!\,(g-c)!\,(g-f)!} \tag{C.10}$$

for $a+c+f=$ even and where $2g = a+c+f$ and

$$\Delta(a\,c\,f) = \left[\frac{(a+c-f)!\,(a-c+f)!\,(-a+c+f)!}{(a+c+f+1)!}\right]^{\frac{1}{2}} \tag{C.11}$$

In addition to obeying all the selection rules for the Racah coefficients, $Z=0$ unless $a+c+f=$ even. Thus the phase factor i^{f-a+c} is always real and equal to ± 1.

There are special cases when either e or f is zero. When $e=0$, corresponding to vanishing channel spin:

$$Z(a\,b\,c\,d;\,0\,f) = \delta_{ab}\,\delta_{cd}\,(-1)^{2f}\,i^{f-a+c}\,[(2a+1)\,(2c+1)]^{\frac{1}{2}}\,(a\,c\,0\,0|a\,c\,f\,0) \tag{C.12}$$

and when $f = 0$, which is related to the total cross section:

$$Z(a\,b\,c\,d\,;\,e\,0) = \delta_{ac}\,\delta_{bd}\,(-1)^{b-e}\,(2b+1)^{\frac{1}{2}} \tag{C.13}$$

where δ_{mn} is the Kronecker delta. In the application to angular distributions in nuclear reactions, $f = L$ is integral so $(-1)^{2f}$ is always equal to $+1$.

The equations presented here, together with algebraic tables for the W coefficients, allow the Z coefficients to be calculated explicitly. They have also been extensively tabulated in [62, 63].

Appendix D

D.1 Reaction kinematics

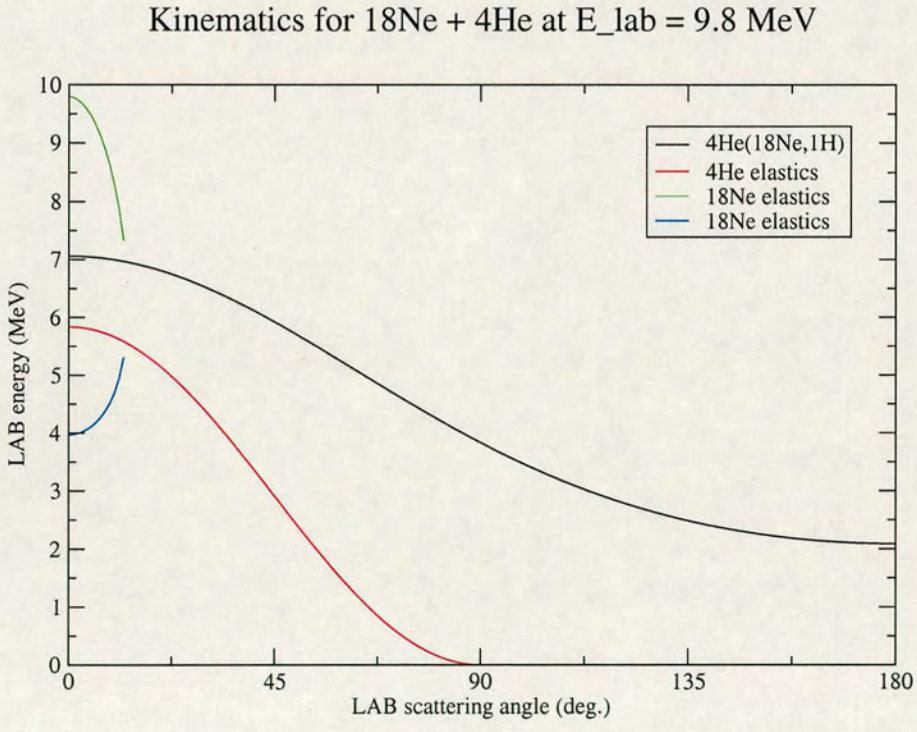

Figure D.1: *Reaction kinematics for* ^{18}Ne+α

Figure D.1 shows a diagram of the reaction kinematics for ^{18}Ne+α at a typical beam energy of 9.8 MeV. It can be seen that elastic scattering of ^{18}Ne on ^{4}He has a maximum scattering angle of $\sim$13°. Thus no elastically scattered ^{18}Ne ions could be detected using a rotated geometry. A ΔE detector with a thickness of 67μm would stop a 9 MeV alpha particle. A look at the kinematics shows that no elastic recoil alphas could punch through a ΔE detector of this thickness. The reaction kinematics clearly show that a ΔE-E telescope placed in a rotated geometry would detect less background than one placed at 0°. The variation in energy of the reaction protons, E_{p} as a function of scattering angle, θ (for a transition to the ground state) can also be seen in figure D.1. Note that there is a one-to-one correspondence between E_{p} and θ.

D.2 2-body kinematics

A reaction can be represented as a two-step process as follows:

$$a + X \rightarrow b + Y + Q \tag{D.1}$$

where a is the projectile, X is the target, Y is the recoil nucleus, b is the scattered particle and Q is the Q-value of the reaction. A schematic showing the reaction geometry is shown in figure D.2.

By conservation of linear momentum we have the following:

$$P_a = P_b \cos\theta + P_Y \cos\phi \tag{D.2}$$

$$P_b \sin\theta = P_Y \sin\phi \tag{D.3}$$

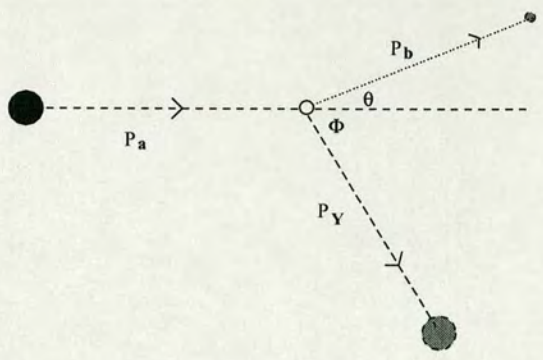

Figure D.2: *Reaction geometry for a+X→b+Y*

Momentum, P is related to kinetic energy, E through $P = \sqrt{2mE}$ where m is the mass of the particle. From conservation of energy we have:

$$Q = E_Y + E_b - E_X - E_a \tag{D.4}$$

Algebraic manipulation of these equations gives the following expression for the kinetic energy of the projectile responsible for the reaction (in the LAB frame):

$$E_a = \frac{1}{8}\left[2\cos\theta\sqrt{2m_bE_b} - 2\Big(2m_bE_b\cos^2\theta - \Big(1-\frac{m_Y}{m_a}\Big)(2m_bE_b\Big(1+\frac{m_Y}{m_b}\Big)\right.$$

$$\left.-2m_YQ)\Big)^{\frac{1}{2}}\right]^2 / m_a\Big(1-\frac{m_Y}{m_a}\Big)^2 \tag{D.5}$$

Note that if the reaction goes to excited states in Y, then $Q = Q_0 - E_{ex}$ where Q_0 is the Q-value corresponding to the ground state of Y and E_{ex} is the excitation energy above the ground state. It can thus be seen that a projectile's kinetic energy can be reconstructed from a knowledge of the kinetic energy and angle of the scattered particle and the Q-value.

The transformation to the CM frame is as follows:

$$E_{CM} = E_{LAB}\left(\frac{m_X}{m_a + m_X}\right) \tag{D.6}$$

The excitation energy of the compound nucleus, E_{CN} is the sum of the kinetic energy of the projectile (in the CM frame of the a + X system) and the binding energy i.e

$$E_{CN} = E_a\left(\frac{m_X}{m_a + m_X}\right) + E_B \tag{D.7}$$

where E_{B} is the binding energy. For the ^{18}Ne+α system, E_{B} = 8.14 MeV and the excitation energy in ^{22}Mg is thus (E_{r} + 8.14) MeV where E_{r} is the resonance energy in MeV.

Bibliography

[1] D.C.B. Whittet, Dust in the Galactic Environment, IOP Publishing (1992)

[2] S.Weinberg, The First Three Minutes, Flamingo, (1993)

[3] C.R. Kitchen, Stars, Nebulae and the Interstellar Medium, Adam Hilger (1987)

[4] T.P. Snow, The Dynamic Universe: an Introduction to Astronomy (4^{th} edition) West Publishing Company (1991)

[5] A.N. Ostrowski, Lecture notes on Nuclear Astrophysics for the 10th Annual Nuclear Physics Summer School (1999)

[6] E.M. Burbidge *et al*, Rev. Mod. Phys. **29** (1957) 547

[7] F. Hoyle, Ap. J. Suppl. 1 (1954) 121

[8] M. Wiescher, Signatures of Nucleosynthesis in Explosive Stellar Processes. Nuclear and Particle Astrophysics, eds. J.G. Hirsch & D. Page, Cambridge University Press (1998) 79

[9] A. Champagne & M. Wiescher, Ann. Rev. Nucl. Sci. **42**, 39 (1992)

[10] R.K. Wallace & S.E. Woosley, Astro. J. Suppl. Ser. **45** (1981) 389

[11] A.M. Laird. Ph.D. thesis. The University of Edinburgh. (2000)

[12] M. Weischer *et al*, Reactions with radioactive beams and explosive nucleosynthesis, Phil. Trans. R. Soc. London. **A356** (1998) 2105

[13] M. Wiescher *et al*, Breakout reactions from the CNO cycles, J. Phys. G. Nucl. Part. Phys. **25** (1999) 133

[14] S. Starrfield, Phys. Rep. **311** (1999) 371

[15] H. Schatz *et al*, Phys. Rev. Lett. **86** (2001) 3471

[16] W.K. Rose, Advanced Stellar Astrophysics, CUP (1999)

[17] F. Käppeler *et al*, Ann.Rev. Nucl. Part. Sci. **48** (1998)

[18] C.E. Rolfs & W.S. Rodney, Cauldrons in the Cosmos, University of Chicago Press (1988)

[19] H. Schatz *et al*, Phys. Rep. **294** (1998) 167

[20] L. Van Wormer *et al*, Ap. J. **432** (1994) 326

[21] W. Bradfield-Smith. Ph.D thesis. The University of Edinburgh (1999)

[22] W. Bradfield-Smith *et al*, Phys. Rev. C **59** (1999) 3402

[23] A.A. Chen *et al*, Phys. Rev. C **63** (2001)

[24] Fortran code "dedx", based on the Northcliffe and Schilling Nuclear Data Tables 7A (1970) 233. The University of Birmingham

[25] G.F. Knoll, Radiation Detection and Measurement (2^{nd} edition), Wiley (1989)

[26] T. Davinson, *private communication* (1999)

[27] T. Davinson *et al*, Nucl. Instr. and Meth. A 288 (1990) 245

[28] S.S.M. Wong, Introductory Nuclear Physics, Prentice-Hall (1990)

[29] G. R. Satchler, Introduction to Nuclear Reactions (2^{nd} edition), Macmillan (1990)

[30] Micron Semiconductor Ltd, Lancing UK

[31] M.C. Scott, Particle Detection Techniques: An Introduction, The University of Birmingham (1986)

[32] EG & G Ortec, Oak Ridge, TN, USA

[33] B. Efken *et al*, NIM **129** (1975) 219

[34] C. Tschalär, NIM **61** (1968) 141

[35] Geissel *et al*, Nucl. Instr. and Meth. **215** (1983) 329

[36] H. Haken & H.C. Wolf, The Physics of Atoms and Quanta (4^{th} edition), Springer-Verlag (1994)

[37] E.C. Finch & A.L. Rodgers, NIM **113** (1973) 29

[38] E.C. Finch, NIMS **A257** (1987) 381

[39] M. Ogihara *et al*, NIMS **A251** (1986) 313

[40] J.F. Ziegler & J. Biersack, The Stopping & Range of Ions in Matter (SRIM) Monte Carlo program, IBM Corporation (1999)

[41] Sort-shell, D. Brightly, CCLRC, Daresbury Laboratory, UK

[42] R. B. Firestone, Table of Isotopes (8^{th} edition), John Wiley & Sons (1996)

[43] E. Kreyszig, Advanced Engineering Mathematics, Wiley & Sons (1988)

[44] J. Görres *et al*, Phys. Rev. C **51** 392 (1995)

[45] J.M. Hollas, Modern Spectroscopy (3^{rd} edition), John Wiley & Sons (1996)

[46] D. Ashcroft, *private communication* (2000)

[47] M. Wiescher, *private communication* (2001)

[48] D.P. Whitmore & C.N. Davids, Phys. Rev. C **9** (1974)

[49] J.D. Jackson, Classical Electrodynamics (3^{rd} edition), Wiley (1999)

[50] W.R. Leo, Techniques for nuclear and particle physics experiments, Springer-Verlag (1994)

[51] J. F. Ziegler *et al*, The Stopping and Range of Ions in Solids, Pergamon Press (1985)

[52] WWW: http://www.research.ibm.com/ionbeams/SRIM/SRIMA.HTM

[53] E. Segrè, Nuclei and Particles, W.A. Benjamin, Inc. (1964)

[54] J.M. Blatt & V.F. Weisskopf, Theoretical Nuclear Physics, Springer-Verlag (1979)

[55] P.M. Endt & M. Demeur (Eds.), Nuclear Reactions Vol. 1. North Holland Publishing Co. (1959)

[56] R. Huby, Proc. Phys. Soc. A **67** (1954) 1103

[57] J.M. Blatt & L.C. Biedenharn, Rev. Mod. Phys. **24** (1952) 258

[58] M. Abramowitz & I.A. Stegun (Eds.), Handbook of Mathematical Functions, Dover Publications, Inc. (1972)

[59] D.M. Brink & G.R. Satchler, Angular Momentum (2^{nd} edition), Oxford University Press (1968)

[60] G. Racah, Phys. Rev. **62** (1942) 438

[61] J.M. Blatt *et al*, Rev. Mod. Phys. **24** (1952) 248

[62] L.C. Biedenharn & A. Simon, Revised Z tables of the Racah coefficients, Oak Ridge National Laboratory Report 1501 (1953)

[63] L.C. Biedenharn & A. Simon, Revised Z tables of the Racah coefficients, Oak Ridge National Laboratory Report 1501 Suppl. 1 (1953)